

WASHINGTON FIELD GUIDE



COLUMBIA UNIVERSITY
DEPARTMENT OF EARTH AND ENVIRONMENTAL SCIENCES
ARTHUR D. STORKE MEMORIAL EXPEDITION

August 3 - August 14, 2014

©Department of Earth and Environmental Sciences, Columbia University, 2014
Prepared and edited by Celia Eddy, Zach Eilon, Helen Janiszewski, Hannah Rabinowitz, Natalia Zakharova
Front Page: Washington Field Trip Participants at Mt. Rainier National Park

Contents

1 Preface	1
2 Trip Itinerary	2
3 Introduction to Washington	5
4 Geologic Overview	13
4.1 Seismic Observations	13
4.1.1 Seismic Techniques	13
4.1.2 Geophysical Observations in the Cascadia Subduction Zone	17
4.1.3 Episodic Tremor and Slip	26
4.1.4 Crustal structure and seismicity of North Cascades	28
4.1.5 Volcano Seismology	30
4.2 Volcanic Features	33
4.2.1 Mt. Rainier	33
4.2.2 Mt. St. Helens	36
4.2.3 Columbia River Basalts	40
4.3 Surface Processes	45
4.3.1 Tsunamis and Surface Expressions of Earthquakes	45
4.3.2 Glacial History and Features of Washington	48
4.3.3 Olympic National Park Rainforest	51
4.3.4 Waterbodies and Coastal Ecology of the Olympic Peninsula	53
5 Detailed Itinerary and Description of Sites Visited	57
5.1 Day 1, August 3, 2014: Ophiolite complex on Fidalgo Island	57
5.2 Day 2, August 4, 2014: Metamorphism and Accretion	60
5.3 Day 3, August 5, 2014: Mt. Baker from afar	66
5.4 Day 4, August 6, 2014: North Cascades National Park	70
5.5 Day 5, August 7, 2014: Columbia River Basalt and Petrified Forest	77

5.6 Day 6, August 8, 3014: Hiking Burroughs Mountain at Mt. Rainier National Park	80
5.7 Day 7, August 9, 3014: Hiking on south side of Mt. Rainier	86
5.8 Day 8, August 10, 3014: Mt. St. Helens - Windy Ridge	91
5.9 Day 9, August 11, 3014: Mt. St. Helens - Ape Caves	99
5.10 Day 10, August 12, 3014: Mima Mounds and Ruby Beach	102
5.11 Day 11, August 13, 3014: Olympic National Park and the Hoh Rainforest	105
6 Campsite Information	109
7 Trip Budget	110
8 Trip Participants	111
9 Acknowledgements	112

1 Preface

Lamont graduate students have a proud history of organizing geological field trips that complement our academic education and nourish interpersonal and observational skills. In that tradition, we conducted a student field trip in August 2014 to explore the geology of the Pacific Northwest.

This region showcases a varied set of natural features with locations of interest for every field of Earth science. From high-latitude rainforests and glacier-carved mountain ranges to ophiolite complexes, active stratovolcanoes and the greatest past (and future?) earthquakes seen in the continental US, this destination offered an unparalleled opportunity for DEES students to observe and understand the wide range of phenomena we study.

Enclosed is a field report that we hope will be of benefit to future travellers to the Pacific Northwest, or any one with an interest in the region. We include a multidisciplinary set of preparatory material relevant to the trip, touching on petrology, glaciology, seismology, and climate science. We then provide daily itineraries from our trip; this resource may be used as a step-by-step field guide or as a source for detailed information about the area. We showcase notable features found in our field guides, as well as observations we made along the way.

This trip would not have been possible without the planning and instruction of Philipp Ruprecht, our faculty representative, who guided us through volcanology, petrology, and the mores of Washington State.

2 Trip Itinerary

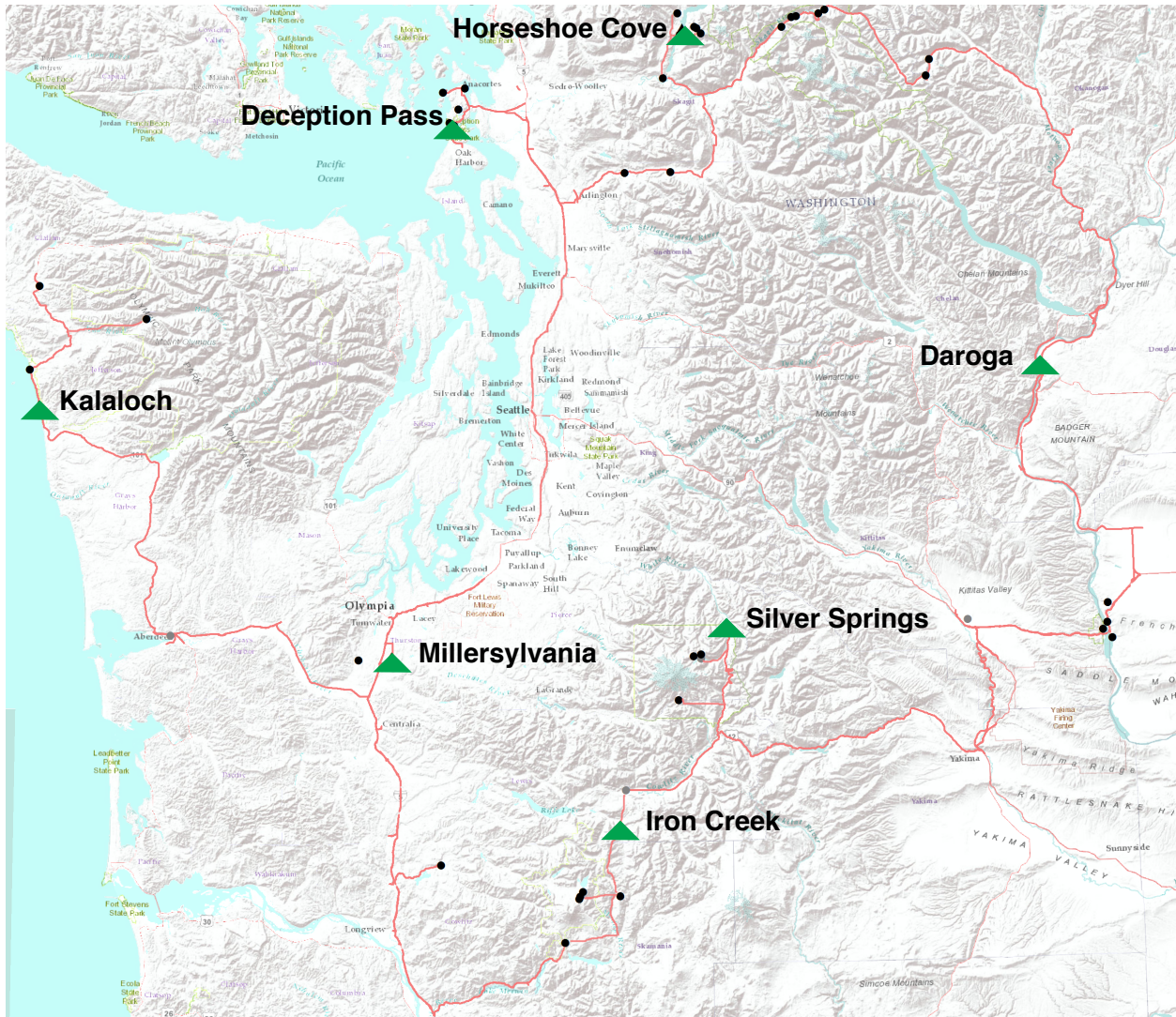


Fig. 2.1: Map of stops on our itinerary. Campsites are labeled and indicated by green triangles. Approximate locations of stops are shown as black dots. Red line: driving route.

Day 1: August 3, 2014

- Flew to Seattle-Tacoma Intl. Airport from Newark Intl. Airport.
- Drove north to Anacortes to view ophiolite sequence.
- Camped at Deception Pass State Park.

Day 2: August 4, 2014

- Outcrops near Deception Pass showing accretionary history.

- Left the Puget Sound region and drove to Mt. Baker-Snoqualmie National Forest, passing the location of the 2014 Oso Landslide.
- Camped at Horseshoe Cove.

Day 3: August 5, 2014

- Local overlooks and hiking in alpine meadows with views of Mt. Baker.
- Visited a dam that regulates river flow and prevents flooding in the region.
- Camped at Horseshoe Cove.

Day 4: August 6, 2014

- Left the vicinity of Mt. Baker and drove east along the North Cascades Highway (SR-20), stopping to note roadside geology. Turned south at junction with Rt. 97.
- Camped at Daroga State Park.
- Note: Original plans were to camp at Alta Lake State Park; however the Carlton Complex fires damaged the park forcing it to close prior to our visit. At the time of writing this guide, reconstruction is ongoing at the park. Daroga State Park was booked last minute, about a week in advance of our trip.

Day 5: August 7, 2014

- Left Daroga State Park and continued driving south with stops to view the Columbia River Basalts.
- Ginko Petrified Forest.
- Longer, scenic route through Yakima with roadside geology and views of Mt. Ranier.
- Camped at Silver Springs.

Day 6: August 8, 2014

- Explored the northern side of Mt. Rainier with Tom Sisson.
- Drove to Sunrise Visitor Center and hiked the Burrows Mountain Trail.
- Camped at Silver Springs.

Day 7: August 9, 2014

- Explored the southern side of Mt. Rainier.
- Drove to Paradise Visitor Center and hiked to Panorama Point with detours to view glacial features.

- Continued to Gifford-Pinchot National Forest.
- Camped at Iron Creek.

Day 8: August 10, 2014

- Explored the northeastern side of Mt. St. Helens.
- Drove to Windy Ridge with roadside stops along the way.
- Hiked the Windy Ridge Trail and continued down into the Pumice Plain.
- Camped at Iron Creek.

Day 9: August 11, 2014

- Drove to Ape Caves on the southern side of Mt. St. Helens.
- Hiked Upper Ape Cave.
- Drove west and then north on I-5 with a stop at Harry Gardener Park.
- Camped at Millersylvania State Park.

Day 10: August 12, 2014

- Stop at Mima Mounds.
- Drove west to the coastline turning north at Aberdeen and continued to Kalaloch Campground.
- Visited Ruby Beach.
- Camped at Kalaloch.

Day 11: August 13, 2014

- Drove to Forks and visited Timber Museum.
- Visited the Hoh Rainforest.
- Visited Kalaloch Beach.
- Camped at Kalaloch.

Day 12: August 14, 2014

- Drove to Sea-Tac Intl. Airport.
- Return flight to Newark.

3 Introduction to Washington

RAJ MOULIK

The Pacific Northwest of the contiguous United States offers unique insights into the geologic history of western North America. Several crustal complexities in the surrounding regions, such as the extensional features in the Basin and Range, the Rocky Mountains and crystalline belts in British Columbia, terminate in Washington. The region has been exposed to a multitude of tectonic events, including continental collisions, metamorphism, igneous intrusions, volcanism and massive flooding events. Washington is part of the American Cordillera, one of the oldest orogenic belts on the planet, and has a long tectonic history with an evolution that spans the entire Phanerozoic (541 Ma - present day).

One reason for this long history is the tectonically stable configuration of an ocean-continent lithospheric boundary, which has persisted since at least Cambrian time. Much of the Mesozoic evolution of the western North American lithosphere can be attributed to the diverse interactions between the Farallon and North American plates [Dickinson, 1991, 1997, 2006, Engebretson et al., 1984, Humphreys, 1995, 2009]. The geology of Washington continues to evolve today due to subduction along the Cascadia convergent margin and associated arc volcanism. In its current configuration (Fig. 3.1), the Juan de Fuca plate subducts beneath North America at a rate that increases northward from 30 to 45 mm/yr with an azimuth of 55 to 63° and the plate is only ~10 My old at the trench [DeMets and Dixon, 1999, Wilson, 1993, 2002, McCaffrey et al., 2007]. The subduction is oblique along the Oregon coast while it is more normal to the margin off Washington and Vancouver Island.

The complex geology of Washington can be studied best by dividing it into major geomorphic



Fig. 3.1: Tectonic setting of the Pacific Northwest. Volcanoes are indicated by red triangles. From north to south they are: Meager, Cayley, Garibaldi, Baker, Glacier Peak, Rainier, Adams, St. Helens, Hood, Jefferson, Three Sisters, Newberry, Crater Lake, Medicine Lake and Shasta. Arrows indicate convergence rates along the plate boundary. Source: USGS.

regions [Fig. 3.2; DNR, 2014]:

Olympic Mountains: These are part of the Pacific Coast Ranges that reach moderate heights of up to ~2400 meters. The Olympic peninsula encounters moisture-laden Pacific storms, which interact with the topography to produce an average of 140 inches of precipitation per year, making it the wettest place in the 48 contiguous states. The Olympics are made up of Eocene sandstone, turbidites and basaltic oceanic crust. The Coast Range basement consists of the Eocene Crescent Formation with thick submarine basalt flows, including pillow lavas. The Crescent Formation was deposited upon continentally derived marine sediments and is interbedded with Eocene limestones. As the convergence accelerated in the Miocene, rocks along the west flank of the Olympics were broken and jumbled up to form a melange called the Hoh rock assemblage. The Olympics were also shaped in the Pleistocene by advancing and retreating glaciers that lead to the typical U-shaped valleys of the Hoh and Queets rivers.

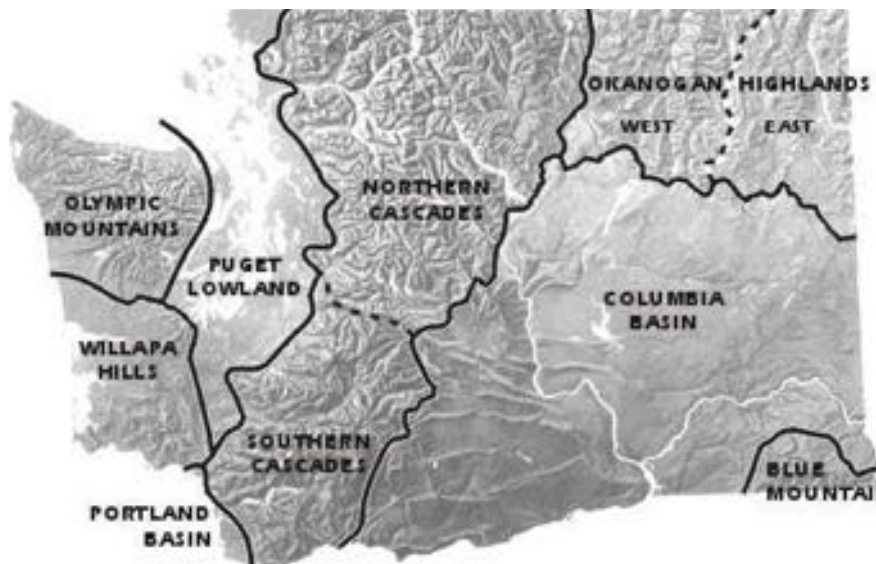


Fig. 3.2: Major physiographic regions of Washington. Adopted from Washington State Department of Natural Resources (DNR).

Puget Lowland: This is a broad, low-lying region situated between the Cascade Range to the east and the Olympic Mountains to the west. The Triassic and Cretaceous sections are represented by clastic sedimentary rocks containing limestone lenses only rarely. The sequence of Jurassic rocks on Fidalgo Island is interpreted to be an ophiolite [Brown et al., 1979] i.e. a section through oceanic crust including some portion of the underlying mantle that has been thrust onto the arc or continental crust by obduction. Starting in the early Pleistocene, the Puget Lowland was subject to four periods of extensive glaciation. The Puget Sound (the body of water contiguous with the Pacific) owes its current geomorphic features to the last continental glaciation that covered the region 18-10,000 years ago.

Cascade Range: The Cascades Arc has been active for the past 37 Ma and is made up of almost 20 major volcanoes that can be classified broadly between the North and South Cascades. The North Cascades are made up of jagged, glaciated mountains comprising Mesozoic crystalline and metamorphic rocks. The magmatic arc consists of two Quaternary stratovolcanoes: Mount Baker and Glacier Peak. The current rugged topography is a result of Holocene glaciation. This region

contains the greatest concentration of alpine glaciers in the 48 contiguous states. The southern portion of the Cascade mountain range in Washington consists predominantly of Cenozoic volcanic rocks and associated deposits. The South Cascades are lapped by basalts of the Columbia Basin to the east, the Columbia River to the south and the Puget Lowland to the west.

Columbia Basin: The Columbia Basin is the drainage basin of the Columbia River and covers an area of 668,000 km². The province is characterized by incised rivers, plateaus, and anticlinal ridges. The region is underlain by Miocene Columbia River Basalt Group rocks and interbedded Neogene terrestrial sediments. The Columbia Basin province is best defined by the areal extent of the Miocene Columbia River Basalt Group rocks, which cover 36 percent of the entire state.

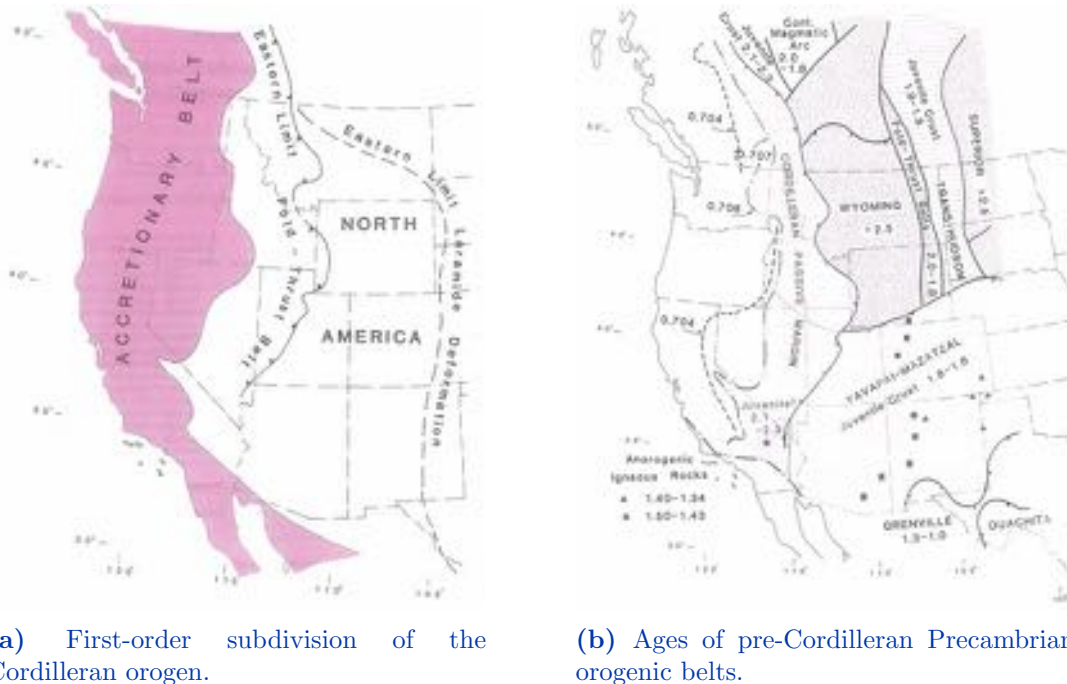


Fig. 3.3: Overall subdivisions and ages of western North America. Source: Burchfiel et al. [1992].

Due to its long history, the Pacific Northwest has become a natural laboratory for the study of how tectonic processes constantly amass and mould terrestrial crust from older or preexisting crustal material [e.g. Coney et al., 1980, Howell, 1989]. An accretionary belt makes up 20 to 50 percent of the width of the American Cordillera at different latitudes (Fig. 3.3a). Although a few of the western terranes can be tied to North America [e.g. Gray, 1986], most of them are allochthonous terranes of primarily oceanic origin [Burchfiel et al., 1992]. Regional variations in isotopic compositions of Sr, O, Nd and Pb in igneous rocks can be used to delineate the boundary between Pre-Cambrian sialic crust and the late Paleozoic-Mesozoic accreted terranes. The isotopic ratio $^{87}\text{Sr}/^{86}\text{Sr}$ is a sensitive indicator of the source material of magmas and of the type of underlying crust. Due to increased crustal contributions from the Pre-Cambrian craton, more radiogenic $^{87}\text{Sr}/^{86}\text{Sr}$ ratios are observed in the plutonic rocks to the east of the cordillera [Farmer and DePaolo, 1983, Arndt and Goldstein, 1987, DePaolo et al., 1991]. Magmas intruding the arc terranes were potentially derived from the upper mantle or subducted oceanic lithosphere of Phanerozoic age and thereby exhibit a less radiogenic signature. The $^{87}\text{Sr}/^{86}\text{Sr} = 0.706$ line appears to delineate the margin between Proterozoic North America and the younger provinces [e.g. Fleck and Criss, 1985,

Ernst, 1988]. This demarcation runs roughly along the Oregon-Idaho border and cuts northwest into Washington State (Fig. 3.3b).



Fig. 3.4: Evolution of the western margin. Top: Early Devonian (400 Ma). Bottom: Early Permian (290 Ma). Source: NAM [2014]

Large tracts of preserved Mesozoic and Cenozoic oceanic lithosphere in western North America have enabled the long-term reconstruction of the Pacific Basin [e.g. Atwater, 1970, Stock and Molnar, 1988]. The basement of the eastern Cordilleran orogen consists of tectonic elements that were already assembled in the Archean and Proterozoic (~ 1.6 Ga, [Hoffman, 1988]). Several terranes were subsequently accreted to form the eastern region of the Cordilleran orogen. With the breakup of the Rodinia super-continent in the neo-Proterozoic (~ 650 Ma), the North American Craton (Laurentia) drifted away to form a passive margin until this was interrupted in Devonian times by the accretion of several island arc terranes (400-250 Ma, Fig. 3.4). With the formation of super-continent Pangea in the Permian, the western margin of North America was dominated by a subduction zone along with continued eastward accretion of island arcs and the generation of continental magmatic arcs (250-50 Ma, Fig. 3.4).

The last of the Farallon oceanic terranes, ‘Siletzia’, was accreted between 56 and 49 Ma (Fig. 3.5). This event coincided with the cessation of the contractional and amagmatic Laramide orogeny and caused a westward jump in subduction to the present-day configuration of the Cascadia subduction zone. Post-accretion marginal rifting and magnetism ensued in Siletzia (44-30 Ma) along with the initiation of the Cascade arc. Siletzia is now a massive formation of marine basalts and interbedded sediments in the forearc of the Cascadia subduction zone [Wells et al., 2014]. Collectively, this province includes basalts of the Metchosin Fm. (Vancouver, B.C.),

Crescent Fm. (Washington), and Siletz River Volcanics (Oregon) [Fig. 3.6a Irving, 1979]. It is classified as an oceanic large igneous province (LIP) and is 8-12 times as voluminous as the Columbia River flood basalts [Reidel et al., 2013], which terminate in south-eastern Washington.

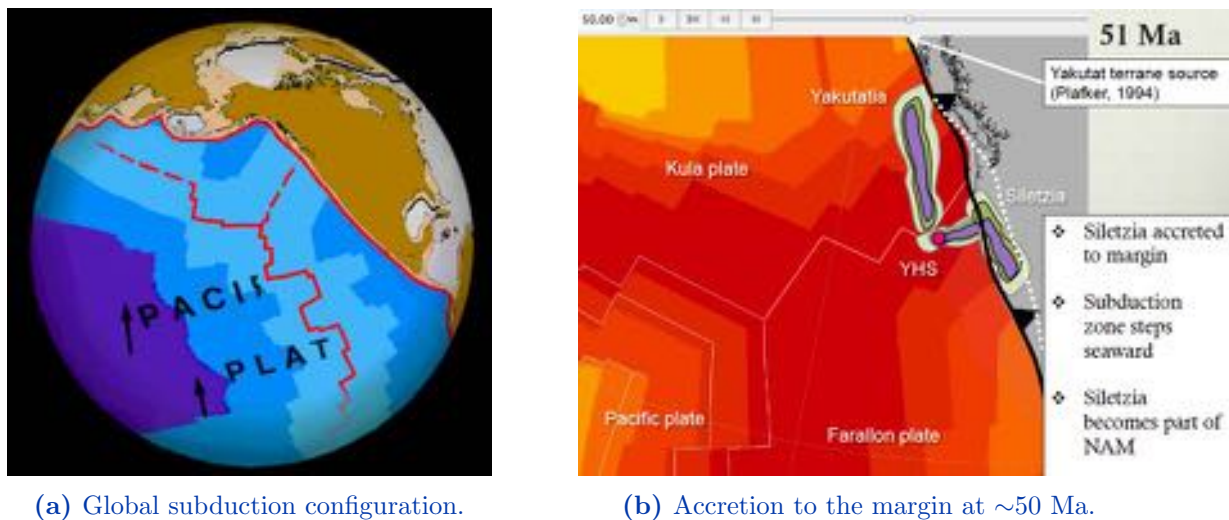
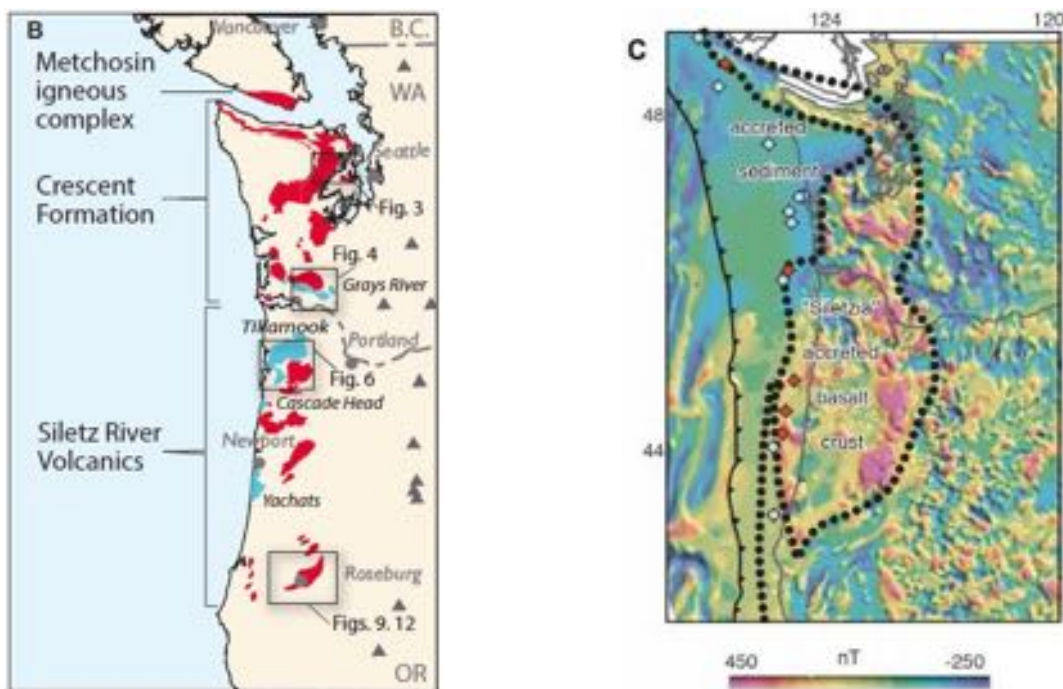


Fig. 3.5: Accretion of Siletzia. Both figures shown at 51 Ma. Source: Atwater, Wells [2014]



(a) Formations composing Siletzia (red) and postaccretion basaltic magmatism (blue).

(b) Extent of Siletzia in the subsurface from regional aeromagnetic data and deep exploration wells.

Fig. 3.6: Formations and extent of Siletzia. Source: Wells et al. [2014]

Geophysical techniques such as seismic imaging and regional potential field data (Fig. 3.6b) suggest that the Siletzia province approached 1.7–2.6 million km³ in original volume [e.g. Trehu et al., 1994] while isotopic dating suggests that much of the magmatism was produced over a 6 million year interval beginning at 56 Ma. The large volume of basalt may indicate a hotspot origin with a mantle source that has isotopic signatures similar to the source of the Columbia River Flood Basalts [e.g. Wells et al., 2014].

Although present-day Cascadia contains most of the characteristics typical of convergent margins [e.g. von Huene and Scholl, 1991], several of its unique features make it an end member among subduction zones. Oblique subduction of the Juan de Fuca plate has created a complex, seismically active convergent margin and transpressive volcanic arc in the Pacific Northwest. The small plates of the Cascadia convergent margin are caught in the dextral shear couple between the much larger Pacific and North American plates [Wells and The Cascadia Working Group, 1989]. There is evidence of progressive and widespread clockwise rotation of the forearc in a broad deformation zone along the plate boundary [e.g. Magill et al., 1982]. Paleomagnetic data indicate Cenozoic clockwise rotation of the Pacific Northwest with respect to stable North America at the rate of $\sim 1^\circ/\text{Ma}$ (Fig. 3.7, Wells and Heller [1988]). Global Positioning System (GPS) velocities suggest that the forearc, arc and a large part of the backarc is rotating as a single, quasi-rigid body [e.g. Khazaradze et al., 1999, Savage et al., 2000, Wells and Simpson, 2001].

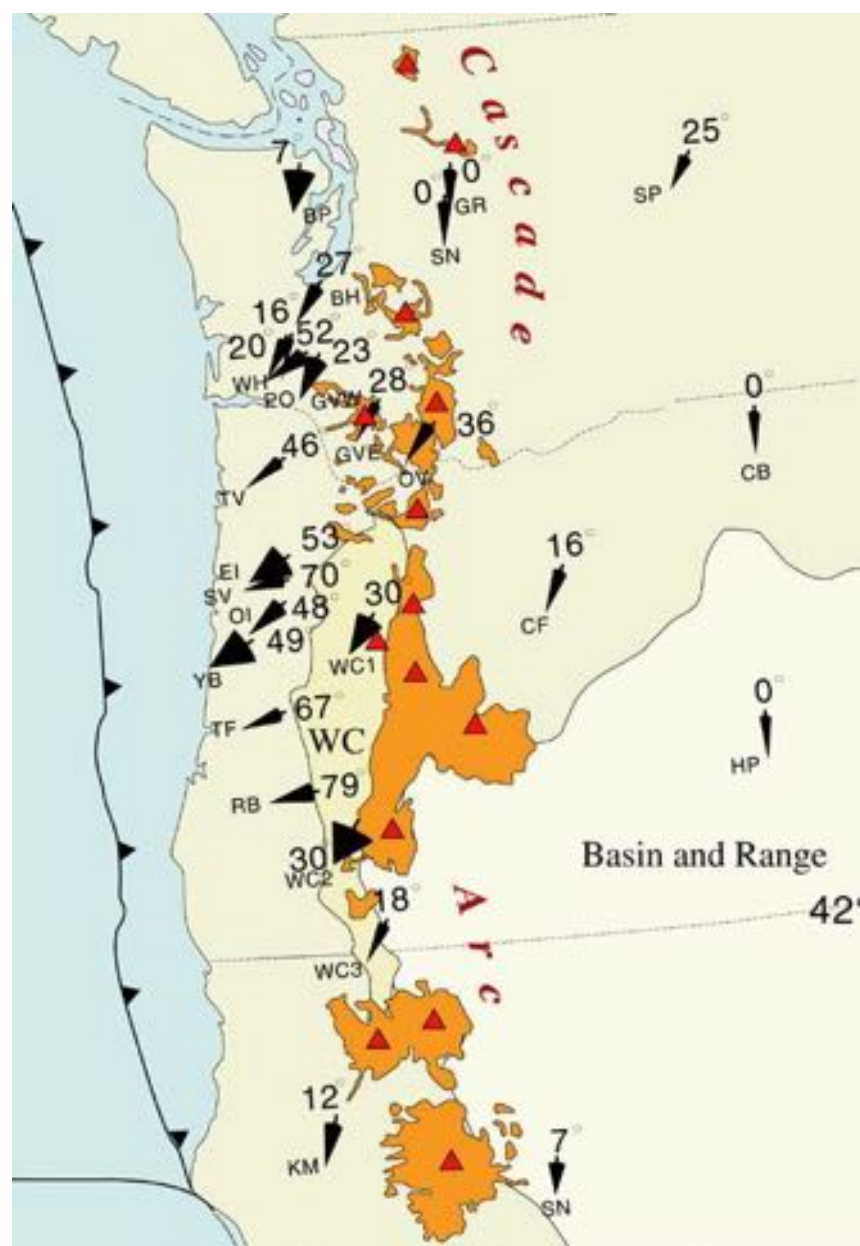


Fig. 3.7: Tectonic rotations of rock units (in $^\circ$) from 21 paleomagnetic studies (1977-1988), summarized by Wells and Heller [1988] and Wells and Simpson [2001].

The GPS velocity field in the forearc has largely been explained as the sum of two processes: 1) elastic deformation above the locked Cascadia subduction zone; and 2) the long term clockwise rotation of an Oregon forearc microplate in response to oblique subduction, basin and range extension and Pacific-North America dextral shear [Wells et al., 1998]. The forearc rotation is linked to contemporary northward migration of the Sierra Nevada block. This results in the breakup of western Washington into smaller, seismically active blocks (Fig. 3.8) that are compressed against the Canadian Coast mountains [e.g. Wells and Simpson, 2001].

The north-south shortening is concentrated in Washington, where it is accommodated by east-west oriented thrust faults like the Seattle fault. The style of slip partitioning is markedly different than that of several other oblique subduction zones like Sumatra, where the migrating forearc is clearly defined by strike-slip faulting near the volcanic arc [e.g. Fitch, 1972, McCaffrey et al., 2007]. The Seattle thrust, which is thought to accommodate this tectonic configuration, has produced several surface-rupturing earthquakes [e.g. Atwater and Moore, 1992] and recent trenching and LIDAR imaging of fault scarps confirms Quaternary activity on this fault [e.g. Nelson et al., 2002, Sherrod et al., 2004]. The Holocene earthquake record for subduction-related megathrust earthquakes in Cascadia indicates a repeat time of \sim 600 years [Goldfinger et al., 2003]. Due to relative quiescence in the recent geologic record and the presence of onshore fault systems, robust hazard assessment in the Pacific Northwest is both challenging and of paramount importance.



Fig. 3.8: Velocity field for the Oregon Coast (OC) and Sierra Nevada (SN) forearc microplates, shown with Euler poles defined with respect to stable North America (from Wells and Simpson [2001], modified from Wells et al. [1998]).

4 Geologic Overview

4.1. Seismic Observations

4.1.1. Seismic Techniques

HELEN JANISZEWSKI

Cascadia's modern subduction environment has made it the subject of considerable seismological enquiry over the past several decades. Seismic studies can be broadly subdivided into *active* and *passive* source experiments. The former studies involve anthropogenic sources, while latter utilise earthquakes and other natural seismic events as sources. Since the tectonic system of Cascadia is characterized by the subduction of the oceanic Juan de Fuca Plate underneath the continental North American plate, a comprehensive investigation of this area requires both onshore and offshore studies, which each provide distinct challenges and advantages.

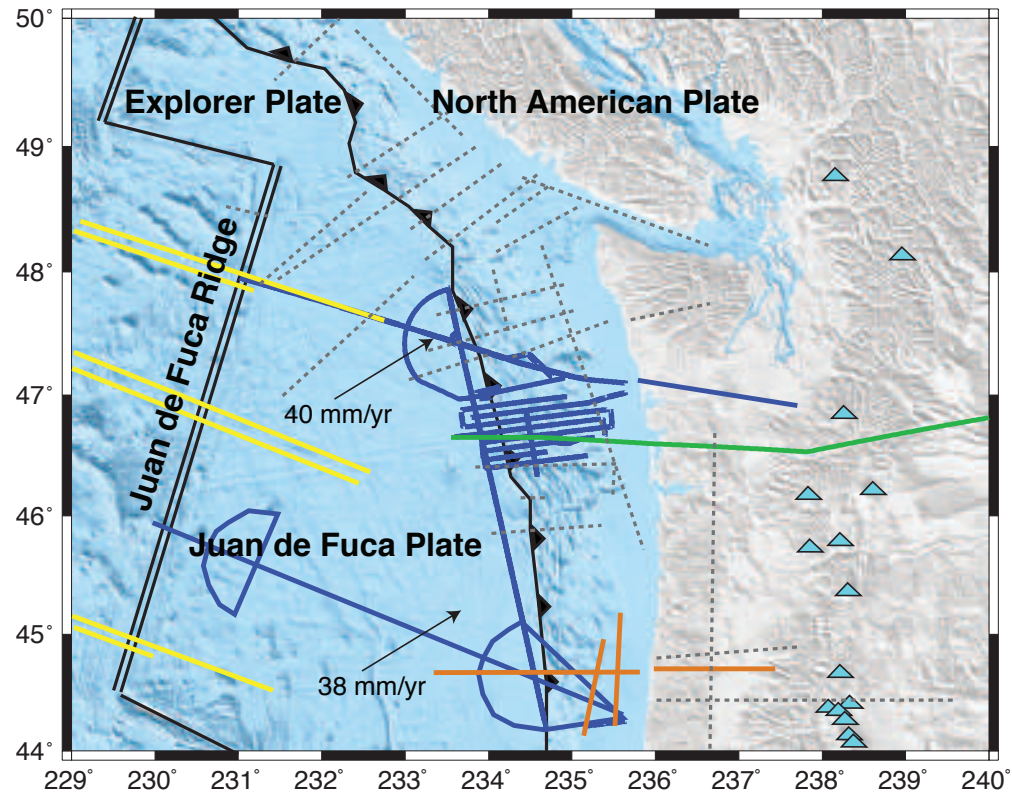


Fig. 4.1: Recent onshore and offshore active source seismic experiments in Cascadia. Green lines: results from Parsons et al. [1998]; orange: results from Gerdon et al. [2000]; yellow: results from Nedimovic et al. [2009]; blue: Ridge-to-Trench and COAST Cruises. Blue triangles indicate volcanoes.

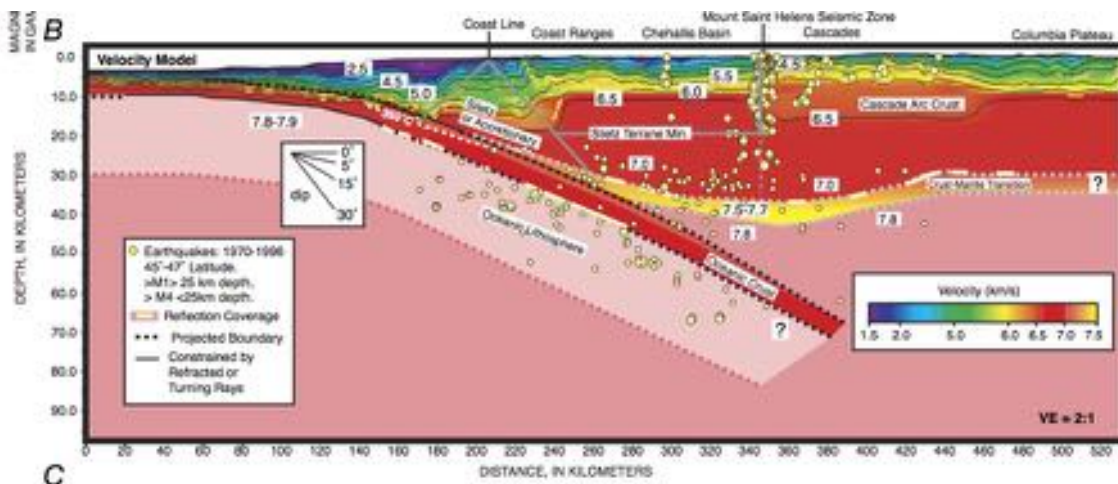


Fig. 4.2: Velocity profile determined by Parsons et al. [1998].

Active source seismic studies in Cascadia have been conducted both onshore and offshore. Onshore studies typically use either explosions or other machines that cause ground shaking to generate seismic signals that are then recorded by seismometers deployed on land nearby. Offshore studies typically involve a ship equipped with an air gun to generate seismic signals. These can be recorded by either hydrophones towed on a streamer by the ship (i.e. multi-channel seismic - MCS), or by nearby seismometers (i.e. wide-angle reflection and refraction) deployed either on the sea floor (Ocean Bottom Seismometers - OBS) or onshore if close to the coastline. MCS studies are sensitive to upper crustal structure and are typically provide information on sediments and faulting within the crust. Wide-angle reflection/refraction studies give information about the velocity structure of the crust and the upper mantle on a larger scale. In subduction environments, the technique can also give information about the subducting crust.

As seen in Figure 4.1, Cascadia has been extensively studied using active-source seismic methods. Parsons et al. [1998] (Figure 4.2) and Gerdemann et al. [2000] used wide-angle onshore and offshore data to image the subducting Juan de Fuca crust from the trench to the Cascades arc. In addition to providing velocity profiles of the North American plate and the subducting crust, they have observed a region of high reflectivity along the subducting plate interface that may indicate hydration within the subducting crust and have implications for the locked zone of the plate interface. Since the link between megathrust fault slip and hydration is not fully understood, it would be useful to estimate the water contained within the slab. One proxy for this may be the extent of faulting within the slab. In particular, faults that reach the mantle may facilitate serpentinization that we may observe using MCS data [Nedimovic et al., 2009] (Figure 4.3).

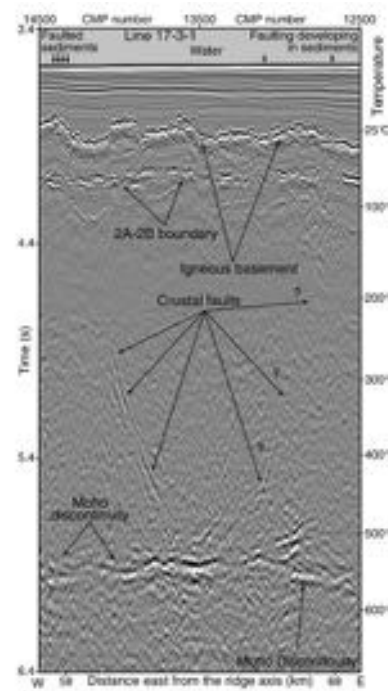


Fig. 4.3: Crustal faults observed in Nedimovic et al. [2009].

Passive source seismology in Cascadia entails studies that focus on local seismicity as well as those that use teleseismic data. Unlike many other subduction zones, Cascadia has relatively little local tectonic seismicity. Consequently, local earthquakes do not provide good constraints on the location of the subducting plate. Despite this quiescence, paleoseismology indicates that large ($\sim M9.0$) megathrust earthquakes have occurred along the thrust interface in the past, most recently in 1700, generating a historically recorded tsunami in Japan [Atwater, 1987, Goldfinger et al., 2003]. Seismologists need to rely on several geophysical techniques to determine the earthquake risk in the region.

Locally, seismologists track the spatiotemporal evolution of episodic tremor and slip (ETS), an emergent seismic phenomenon not controlled by normal tectonic processes [Rogers and Dragert, 2003]. The mechanism behind ETS is not fully understood, but is thought to be related to locking and slip along the megathrust (see Section 4.1.3).

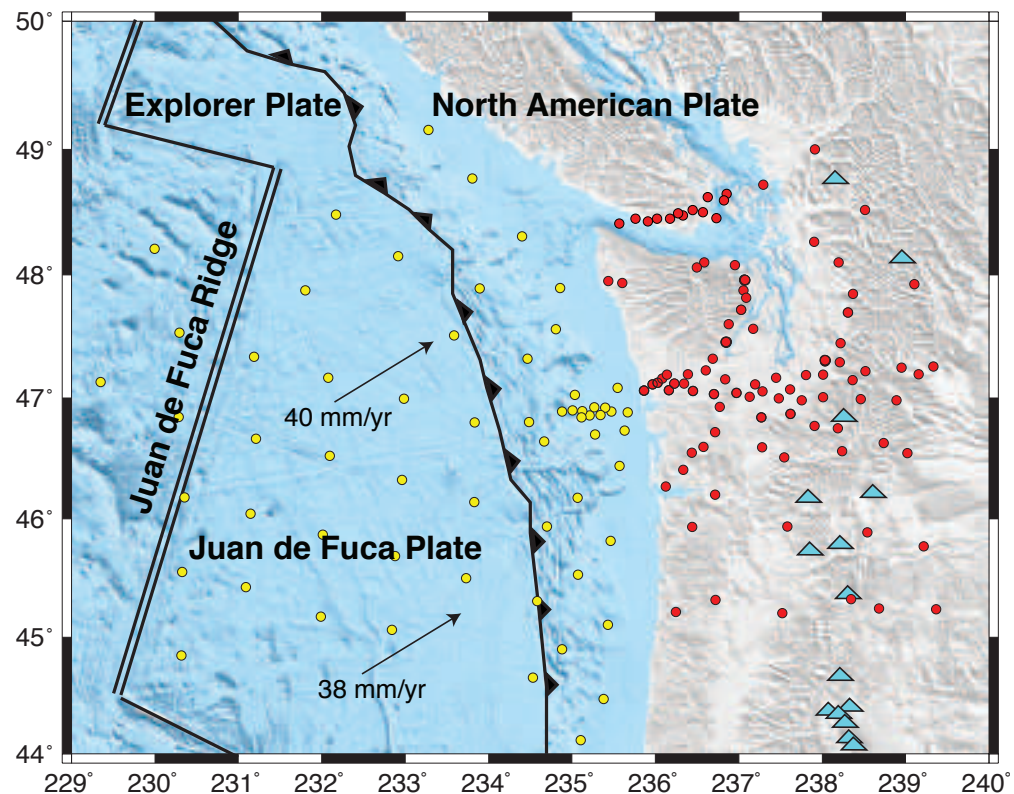
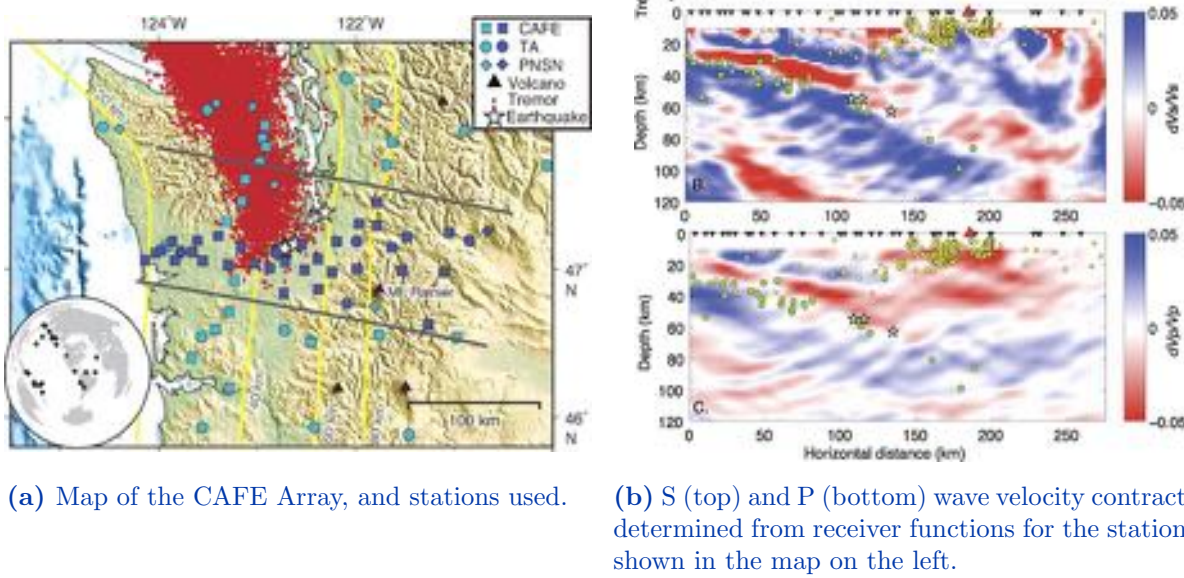


Fig. 4.4: Recently deployed stations for passive teleseismic studies including those used for the results of Abers et al. [2009], Audet et al. [2009], and Bostock et al. [2002] (red circles), as well as the OBS stations from the Cascadia Initiative (yellow circles).

Other techniques used in passive-source seismology make use of teleseismic events, or events that occur globally that are recorded in Cascadia. A sampling of instruments that have been deployed recently for passive source seismic experiments is shown in Figure 4.4, and includes both onshore and offshore instruments. Wider-scale tomography has been used along the entire western United States to image the remnant Farallon plate and the mantle plume related to the Yellowstone hotspot [Obrebski et al., 2010].

On a more localized scale, receiver functions have been used to image the structure of the downgoing Juan de Fuca crust beneath Cascadia [Abers et al., 2009, Audet et al., 2009]. These are most sensitive to abrupt velocity boundaries and are able to resolve layering within the subducting crust. These studies have observed velocity contrasts at both the top and base of the subducting crust, interpreted respectively as a layer of hydrous minerals or metasediments, and the oceanic Moho (Figures 4.5a and 4.5b). This understanding of the compositional structure of the subducting crust is important for determining the location of the locked zone and, therefore, the regional risk from any potential megathrust earthquake.

Unfortunately, the margin of the Juan de Fuca and North American plates extends several hundreds of kilometers offshore in Cascadia. Receiver functions calculated from OBS stations are required to resolve the velocity structure of the subducting crust offshore. The stations deployed as part of the Cascadia Initiative (a large 4 year community experiment) are being utilized in this regard, and will hopefully determine the extent of this structure within the slab and be capable of resolving local heterogeneities.



(a) Map of the CAFE Array, and stations used.

(b) S (top) and P (bottom) wave velocity contracts determined from receiver functions for the stations shown in the map on the left.

Fig. 4.5: Receiver function study from Central Washington [Abers et al., 2009].

4.1.2. Geophysical Observations in the Cascadia Subduction Zone

ZACH EILON

The dominant tectonic influence on the Pacific Northwest today is the subduction system of Cascadia, the region extending from northern CA up to WA. The Juan de Fuca plate is subducting eastwards beneath the North American continent, resulting in classic arc magmatism and (according to palaeoseismic data) occasional megathrust earthquakes. The associated seismic hazard is perhaps the most potent natural disaster that could affect the continental US; this risk, along with easy access to facilitate experiments, has made the Cascadia subduction zone one of the best studied worldwide. Among its atypical features are: a paucity of $M < 7$ thrust interface earthquakes, regular episodic tremor and slip, and a relatively shallow arc system.

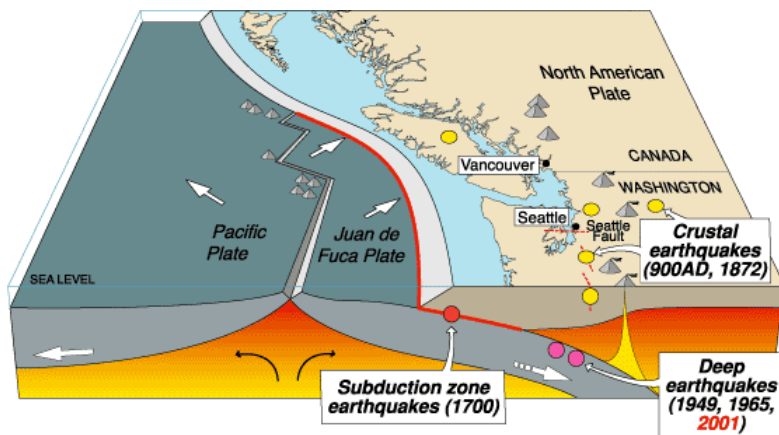
The Cascadia subduction zone is atypically “quiet”, i.e. there is very little seismic activity observed. As a result, it was thought to be a region of low seismic hazard [Acharya, 1992]. In fact, fault quiescence can result from two end members of fault behaviour: total unlocking (aseismic slip) or total locking. The former implies essentially frictionless sliding and zero stress accumulation, while the latter implies zero slip and maximal stress accumulation, which must be relieved in occasional large slip (megathrust) events. Whereas the former case had been long-assumed, Paleoseismic observations of $M > 8$ thrust events made it clear that, in fact, the latter must prevail.

As shown in Figure 4.6 there are three source regions for earthquakes associated with Cascadia subduction:

Subduction interface: earthquakes associated with friction at the interface between the overriding North American plate and the subducting Juan de Fuca plate. Outboard of the trench, we may also observe bending-related faulting at the outer rise.

Deep slab events: deeper than ~ 30 km we observe earthquakes within the subducting slab [Preston, 2003], thought to be a result of dewatering reactions or (at depths > 70 km) a number of other proposed mechanisms including dehydration embrittlement, volume-reducing phase transitions, and runaway thermal instability.

Upper plate crustal faults: Earthquakes in the crust of the overriding plate, largely as a result of some trench-parallel component of convergent motion introducing a component of shear (in addition to the near-perpendicular shortening) that is accommodated in transform zones close to



Source	Affected area	Max. Size	Recurrence
● Subduction Zone	W.WA, OR, CA	M 9	500-600 yr
● Deep Juan de Fuca plate	W.WA, OR,	M 7+	30-50 yr
● Crustal faults	WA, OR, CA	M 7+	Hundreds of yr?

Fig. 4.6: Cartoon of Cascadia earthquake sources. Source: Wikipedia.

the plate boundary. There may also be some seismic activity associated with volcanism.

These earthquakes are captured by a number of seismic recording networks (Figure 4.7):

Cascadia Initiative deployment: an array of onshore/offshore seismometers and geodetic stations that has been marching up and down the Pacific NW coast.

The Pacific Northwest Seismic Network (PNSN): a heterogeneous mix of seismometers deployed throughout Cascadia, run by the University of Washington.

The California Integrated Seismic Network (CISN): an array of seismometers deployed throughout California, run by the University of California: Berkeley.

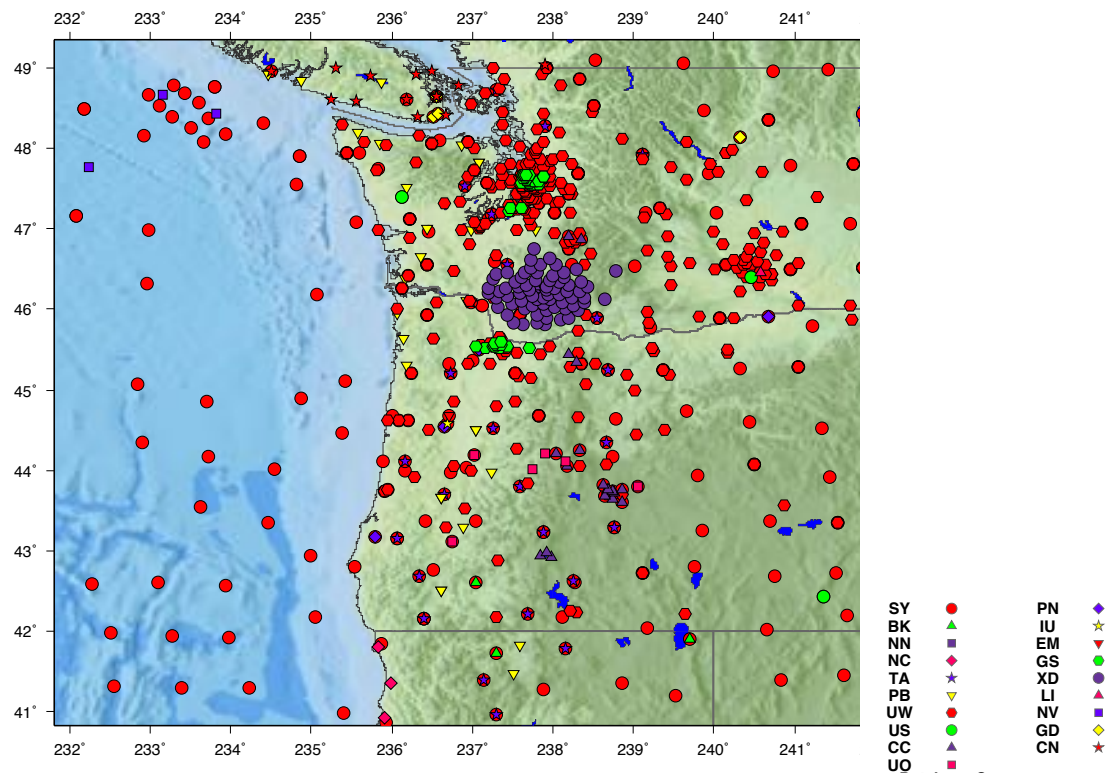
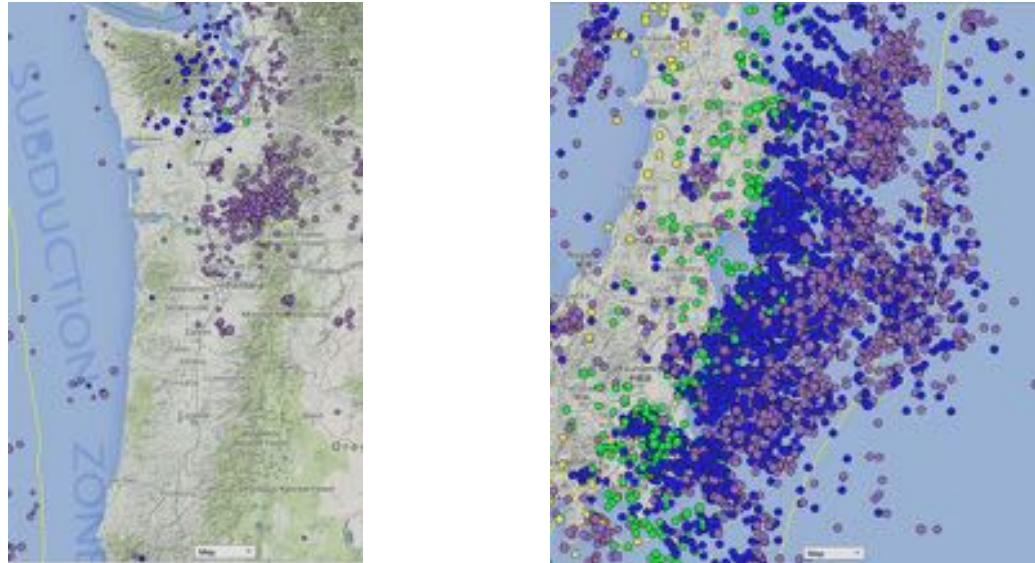


Fig. 4.7: Summary of all active seismic stations in Cascadia reporting data to IRIS. Network code in legend. Map from IRIS website.

This close monitoring allows excellent observations of local seismicity, with magnitude of completeness of the seismic catalogue as low as M=0 beneath much of the PNSN. Despite this good coverage, very few earthquakes are observed, compared to other subduction zones (e.g. Japan - see Figure 4.8). The Cascadia subduction zone is largely quiescent; this results from some convergence being accommodated aseismically as well as some strain accumulation that may be released in large megathrust earthquakes.



(a) Seismicity in Cascadia since 1971: ~1500 earthquakes total.

(b) Seismicity at Japan trench since 1971: 5000 shown, of ~50000 earthquakes total.

Fig. 4.8: Comparison of seismicity at Cascadia and NE Japan, at the same scale. Only $M \geq 3$ are shown.

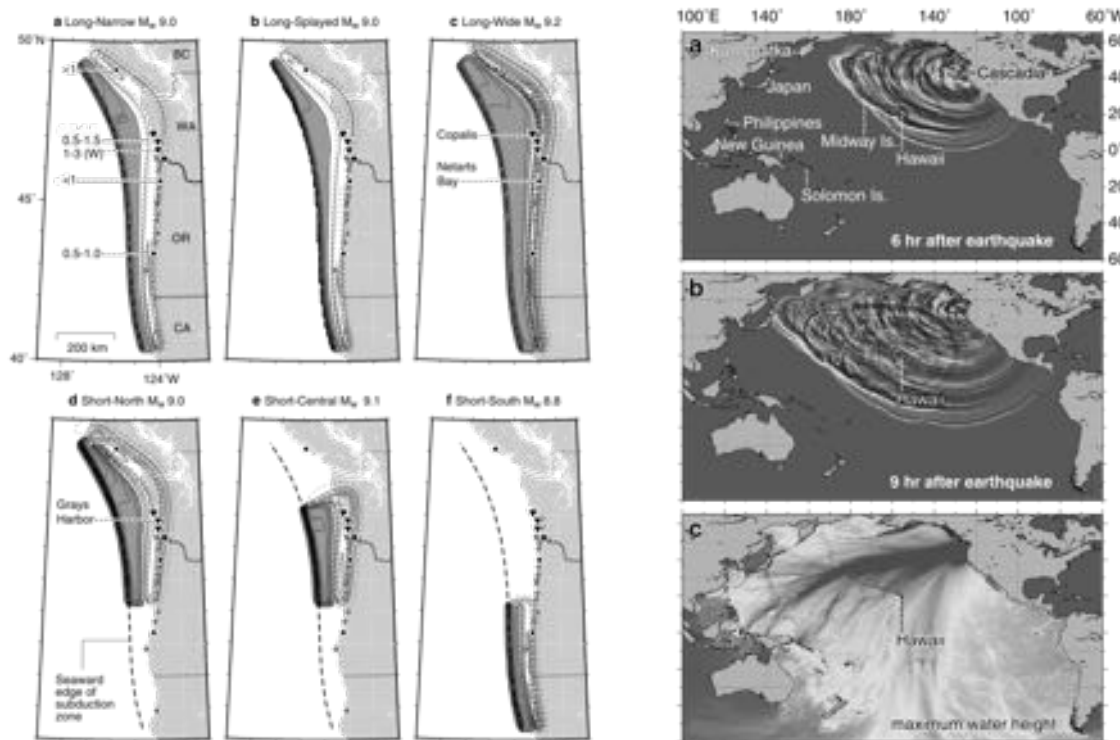


Fig. 4.9: Forward models of 1700 rupture [Satake et al., 2003]. The "Long-narrow" or "Long-splayed" simulations (a & b on the left) match paleotsunami records in Japan the best. Both of these indicate that the 1700 earthquake had magnitude $M_W \sim 9.0$

In the last 20 years we have discovered abundant evidence for very large, $M > 8$ earthquakes on the

Cascadia thrust zone. These destructive earthquakes have a periodicity of between 300-500 years, and the most recent was in 1700. The next “big one” has the potential to be the single largest natural disaster ever to strike the continental US.

The last major earthquake on the Cascadia subduction zone occurred in 1700, according to data from Japanese tsunami descriptions [Satake et al., 2003] (Figure 4.9) and radiocarbon dating from deposits along the Pacific NW coast [Nelson et al., 1995]. A history of large earthquakes on this plate boundary has been pieced together from several types of paleoseismological data, including tsunami deposits in coastal Oregon lakes [Kelsey et al., 2005], turbidites [Goldfinger et al., 2012], and tidal-zone tsunami deposits [Nelson et al., 2006]. The widespread nature of these seismic indicators points to rupture zones up to 900 km long and the magnitude of tsunami waves as far away as Japan confirms the large magnitude of these ruptures: on the order of $M_W \sim 9.0$.

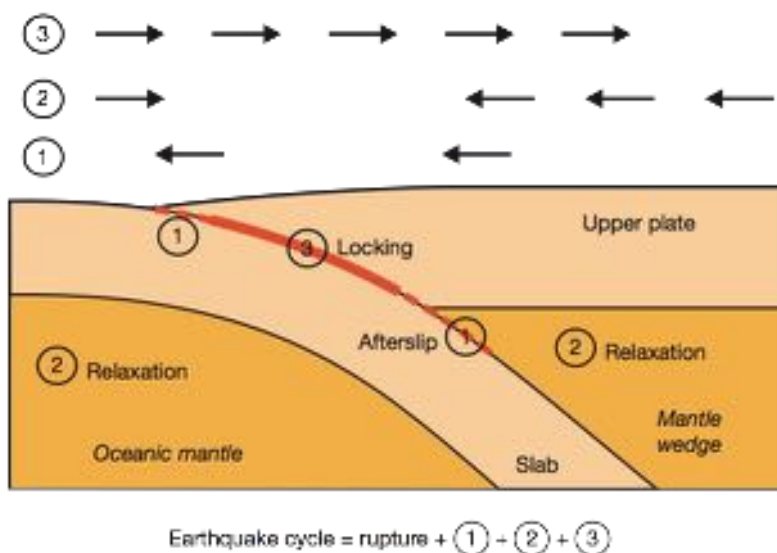


Fig. 4.10: Primary processes following a subduction earthquake [Wang et al., 2012]. Stage 1: Afterslip stage, overriding plate moves seaward. Stage 2: Post-seismic, ductile relaxation processes, near-trench region moves landward, further inland, upper plate slips seaward. Stage 3: Inter-seismic, overriding plate moves landward at subducting plate rate. Locked.

stage (3), as expected from the known time since the last large earthquake. That said, the average GPS motions are smaller in magnitude than the relative plate motion vector, indicating that only a portion of the convergence is being stored as stress on a locked interface. Given that the margin is largely aseismic the rest of the motion must be accommodated by slippage that has no seismic signature, or via episodic tremor and slip.

One of the principal controls on the behaviour of the subduction zone, from seismicity to slab morphology to volcanism, is the composition and (thermal/mechanical) structure of the downgoing plate. Sediments may have implications for mechanical or hydrous lubrication of the plate interface, and may form accretionary wedges that affect tsunamigenesis and material transport. Pre-existing weaknesses at faults formed close to mid-ocean ridges or at the outer rise can be later reactivated within the slab, and may control localisation of deep seismicity; the availability of these structures

One of the ways to constrain the state of stress on a subduction interface is by using geodetic observations to estimate fault locking. Using GPS stations close to the plate boundary, one may assess what stage of the seismic cycle the interface is at: the afterslip stage, the post-seismic stage, or the inter-seismic stage (Figure ??). Between the post-seismic stage and the inter-seismic stage the region of neutral motion moves progressively landward (Figure ??): this line is therefore a proxy for time since rupture and mantle rheology.

Figure 4.11 shows a comparison between the geodetic motions at Cascadia in comparison to other subduction zones: Cascadia appears to be in the inter-seismic

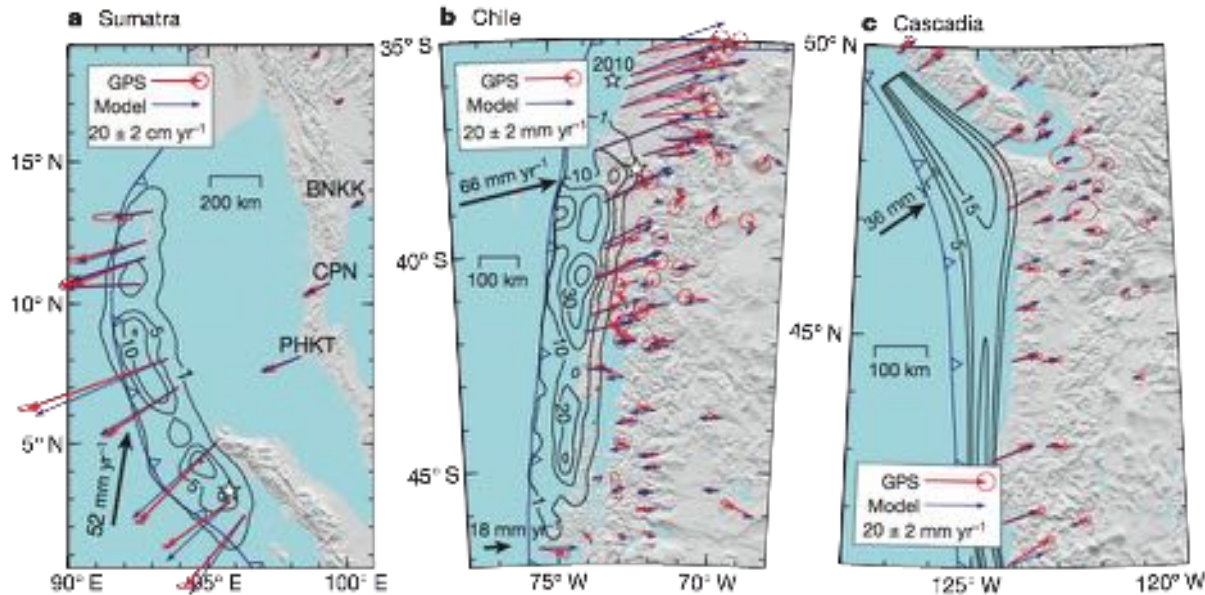


Fig. 4.11: Comparison of geodetic models at three well studied subduction zones [Wang et al., 2012]

is thought to be partly contingent upon the orientation of abyssal fabric with respect to the trench. The age of the downgoing plate (A), the convergence rate (V), and the slab dip (δ), all of which are potentially interrelated, are important parameters that contribute to the *thermal parameter*:

$$\Phi = AV \sin \delta \quad (4.1)$$

This parameter is a proxy for the temperature of the plate at a given depth (larger Φ means cooler temperature) which is a fundamental control on the width of the seismogenic zone and the depth of mineral reactions within the slab. This last is key to the flux of water into the subduction wedge as a result of de-watering reactions. Hydrous minerals in the slab crust and upper mantle release H_2O , a process that controls volcanism, wedge dynamics, and global water budgets.

Thus, a good understanding of “what goes down” is the foundation upon which interpretations of subduction zone processes must be built. This understanding is built from a synthesis of ODP data, active source seismology experiments, and OBS observations, as well as geomagnetic and bathymetric surveys (e.g. Nedimovic et al. [2009], Figure 4.12). At the point of subduction, the sediments, crust, and upper mantle of the downgoing plate contain weight percents of water bound within the structure of hydrous minerals. Some water is also carried as pore fluid, but this is mostly lost during shallow compaction. Additionally a small quantity of water is bound within nominally anhydrous minerals. As the plate subducts and heats up, these hydrous minerals become thermodynamically unstable and break down, releasing their water in the process. Different minerals undergo these dehydration reactions at different depths, resulting in a spectrum of depths of release of hydrous fluid, from 40–150 km.

As these hydrous fluids rise into the wedge, they hydrate the olivine-dominated mantle in the cold nose of the wedge, forming the mineral serpentine. This has significantly lower seismic velocities and higher V_p/V_s ratio than olivine, and thus the serpentinisation progress (fraction reacted) can be observed using seismic imaging techniques: the serpentinised nose of the wedge has markedly lower velocities than the adjacent peridotitic mantle, sometimes so low that there is an inverted

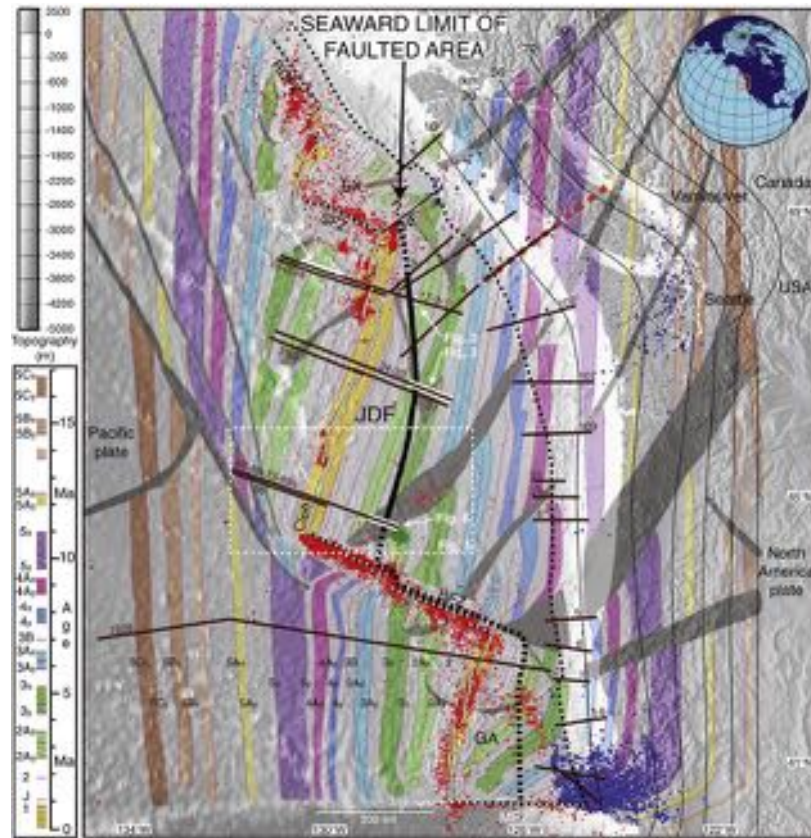


Fig. 4.12: Compilation of data on Juan de Fuca plate [Nedimovic et al., 2009]

velocity jump (i.e. low to high, as opposed to the usual high to low) at the Moho of the overriding continent (Figure 4.13).

Seismic images of this sort also reveal eclogitisation of the basaltic oceanic crust at depths >40 km. Eclogite is an assemblage of primarily garnet and omphacite (clinopyroxene) which are seismically faster than basalt/gabbro. As a result, the onset of this reaction is marked by a reduction in velocity contrast between the slab crust and the mantle.

An emerging technique which has important potential for informing us about fluids, in particular, is the magnetotelluric method (e.g. Figure 4.14). This measures conductivity (or, inversely, resistivity), which is a function of temperature and is also strongly sensitive to the presence of interconnected fluids and melts. This technique has the potential to observe fluid transport pathways within the mantle wedge, which may allow us to answer long-held questions regarding channelisation and the nature of arc melts. This imaging technique can also be used complementarily with seismic analysis, to help resolve trade-offs between heterogeneities in melt/temperature/composition.

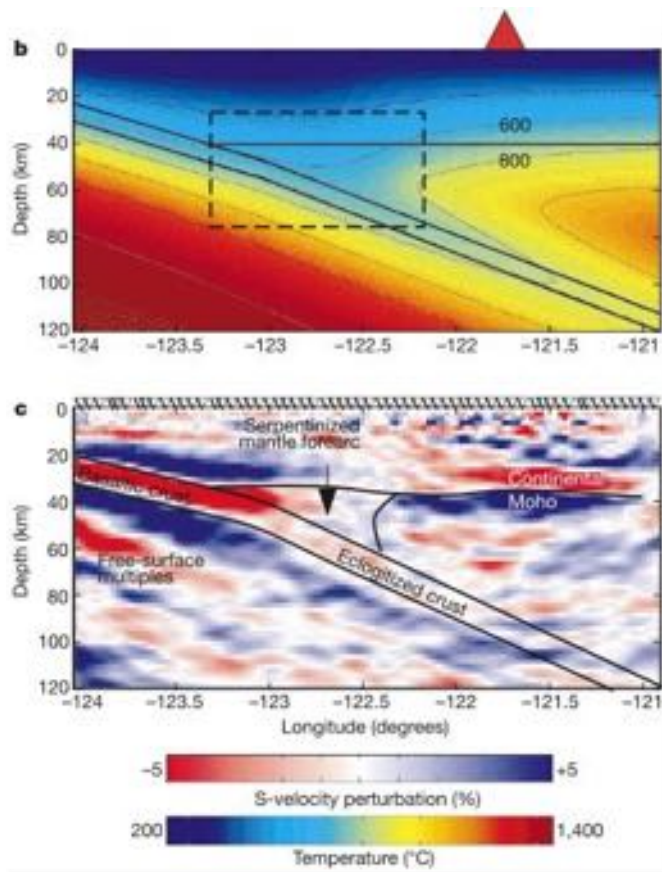


Fig. 4.13: Top: thermal model of Cascadia subduction zone, showing cold nose of the wedge. Bottom: S-velocity perturbations, with interpreted structure. From Bostock et al. [2002].

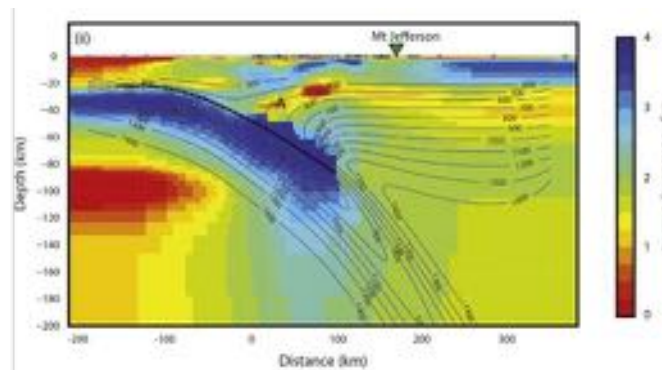


Fig. 4.14: Preferred model from an EM inversion using an onshore/offshore MT transect in central Cascadia. N.B. this model is under-resolved, and importantly includes prior information specifying a slab. From Evans et al. [2013].

of 70 broadband instruments was installed in June 2014, centered on the volcano (Figure 4.16).

Using a combination of reflection (and refraction) data collected during active source seismic experiments, we may image the structure of the shallow subduction system. We observe the megathrust interface as well as structures within the accretionary prism and overriding plate, for example megasplays that carry tsunamigenic risk. These images inform us about potential rupture characteristics, with important consequences for hazard. In more detail, the nature of the reflective character of the interface is thought to be related to its physical properties (e.g. thickness, presence of water) that in turn control seismogenicity. Nedimović et al. [2003] show a good agreement between a change in reflection character of the plate interface and the transition (inferred from thermal and dislocation studies) between locking and aseismic sliding (Figure 4.15). The down-dip limit of the frictionally unstable portion of the fault is a key control on the maximum size of earthquake that may occur, since magnitude is proportional to area and, hence, fault width. Thus the reflection character may inform us about potential seismic hazard and fault behaviour.

Further from the plate interface, iMUSH (information at <http://imush.org>) is an ongoing collaborative experiment attempting to image Mt. St. Helens in more detail and with a greater variety of observational techniques than have ever before been brought to bear on a single volcano. The total data collection will take 4 years, and will entail passive seismic monitoring, multi-shot active-source seismics, magnetotelluric imaging, and extensive geochemical sampling to complement the existing database. This experiment brings together researchers from the University of Washington, Rice University, Columbia University, Oregon State, as well as the USGS.

Passive seismic:

A 100 km aperture array

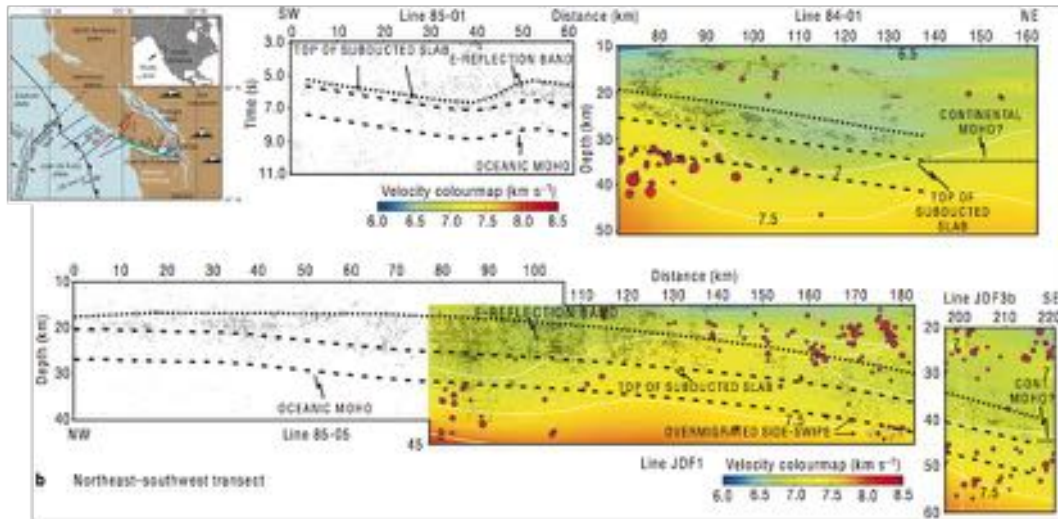


Fig. 4.15: Preferred model from an EM inversion using an onshore/offshore MT transect in central Cascadia. N.B. this model is under-resolved, and importantly includes prior information specifying a slab. From Nedimović et al. [2003].

These stations will record local and teleseismic earthquakes during their 2 year lifetime; in theory, they will allow tomographic imaging down to ~ 100 km depth, as well as monitoring shallower seismicity caused by magma movements. Receiver function and ambient noise techniques will contribute to detailed 3D imaging of crust and upper mantle.

Active seismic: 23 explosive charges in roughly concentric rings around the volcano provided the sources for this part of the experiment; these charges were placed in boreholes and were of considerable magnitude: the largest two were recorded as $M_L = 2.3$. The receivers were arrayed in SE-NW and SW-NE refraction lines, as well as shorter radial lines, and in dense lines in the volcano's immediate vicinity (see Figure 4.17): around 4200 sensors in all. The 150 km offset refraction lines should image down to the 15 km moho, and an iterative analysis scheme of travel time tomography, waveform tomography, and adjoint tomography will lead to a highly detailed image of the crustal structure within the arrays.

Magnetotelluric: A wide-aperture array of 150 wide-band MT stations, with a nominal site spacing of 7.5 km, will shortly be deployed, bridging the gap between a previous edifice-scale study and the coarse Earthscope coverage. This technique aims to answer a

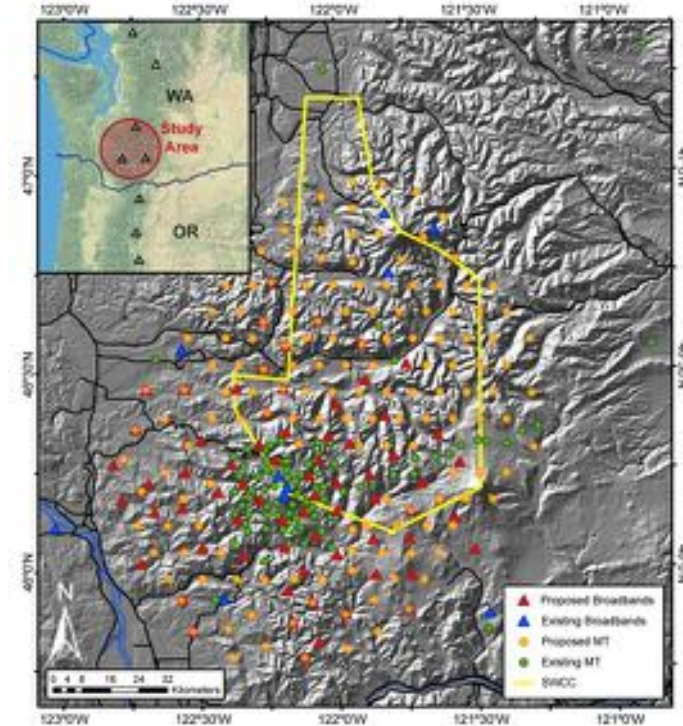


Fig. 4.16: Intended deployment of all passive stations.

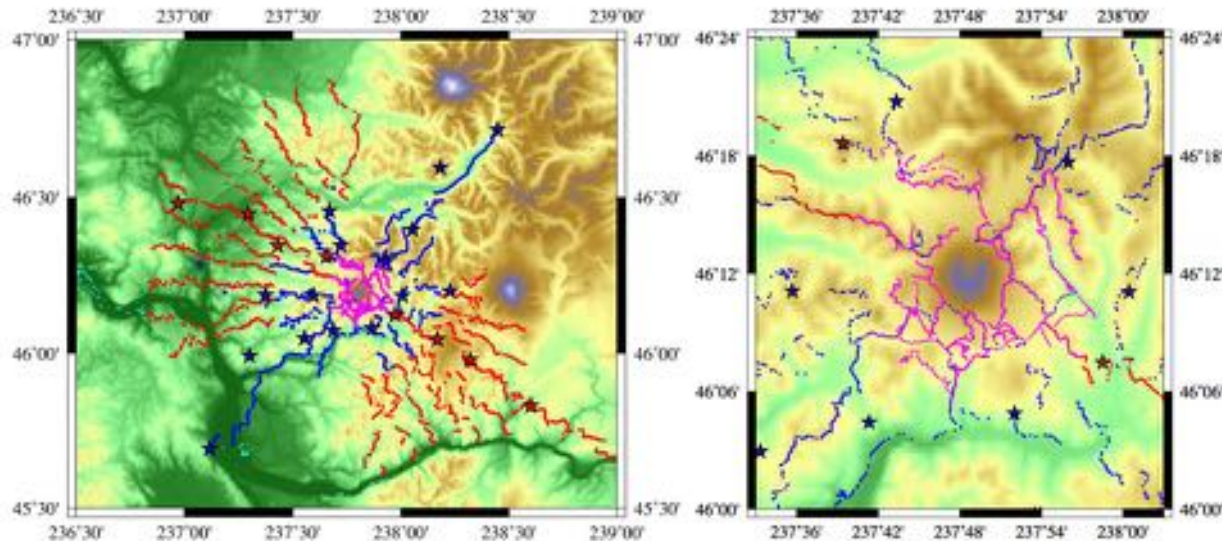


Fig. 4.17: Planned active-source experiment: shots are stars and receivers are dots. Left is the entire deployment, right is a close-up around Mt St. Helens. Purple receivers are deployed throughout, blue receivers are deployed for the first set of shots, red ones for the second.

principal question: where and in what volumes do arc magmas stall within the crust?

Geochemical: Systematic sample collection will complement existing petrological datasets. In-situ U/Th/Pb dating on zircons will identify xenolith inclusions that are co-magmatic with recent volcanic activity. For those inclusions with amphibole and pyroxene phenocrysts, geothermobarometric techniques will be applied to obtain crystallisation histories. The resultant constraints on last equilibration P,T conditions (putatively identifying magma chambers/stalling sites) can be compared to the geophysical results.

4.1.3. Episodic Tremor and Slip

HANNAH RABINOWITZ

In addition to being an area of interest for those studying megathrust earthquakes, Cascadia is notable in its role as the site where the phenomenon of episodic tremor and slip (ETS) was first observed. First, we consider the frictional stability conditions of a subducting plate in order to put the ETS phenomenon into context (Figure 4.18). The shallowest part of a subducting plate (the upper ~ 10 km) is thought of as stably sliding due to the velocity strengthening character of shallow sediments [Ikari and Saffer, 2011, Marone and Scholz, 1988, Scholz, 1998]. Seismicity generally nucleates below this depth up to depths of around 35 km where material begins to deform by more plastic mechanisms [Hyndman et al., 1997].

In 2001, through analysis of GPS data, scientists were able to record a new mechanism for release of strain in subduction zones [Dragert et al., 2004]. Geodetic signals in the Cascadia region that show repeated episodes of increased slip in the opposite direction of plate motion have been demonstrated to be contemporaneous with emergent seismic signals that are correlated across local seismic networks (Figure 4.19) [Dragert et al., 2004, Rogers and Dragert, 2003]. ETS in Cascadia is characterized by repeating slip events that last for tens of days and recur approximately every 14 months. These signals are also seen in other places such as in Japan [Obara, 2002, Obara and Sekine, 2009] though the repeat times in different locations vary slightly. These events have also been demonstrated to migrate in space during each recurrence (Figure 4.20)

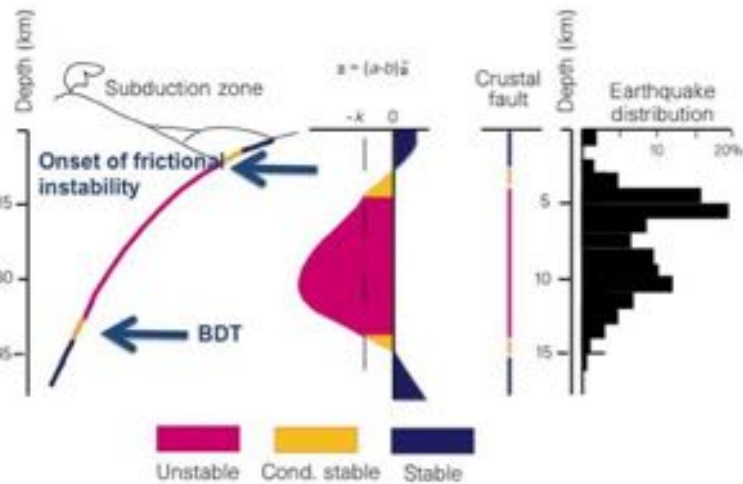


Fig. 4.18: Frictional stability in subduction zones after Scholz [1998]. Earthquake nucleation occurs in the unstable regime (pink).

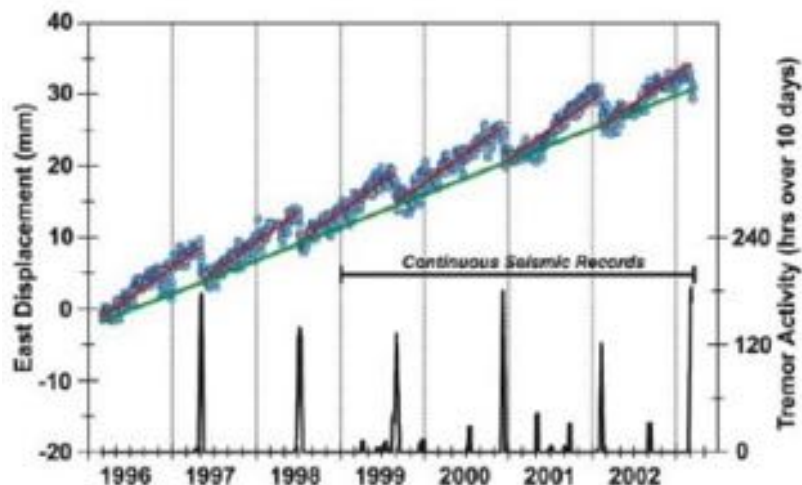


Fig. 4.19: Episodic tremor and slip can be recorded using GPS (blue data) as well as cross-correlated seismic signals. The coincidence of these measures provides confidence that this strain is being accommodated during tremor events rather than by aseismic slip. [Rogers and Dragert, 2003]

[Kao et al., 2009]. Proposed mechanisms for ETS have focused on the effect of elevated pore fluid pressure in generating low frequency events at the conditions of the lower transition in frictional stability (Figure 4.21) [Burlini et al., 2009, Saffer and Tobin, 2011].

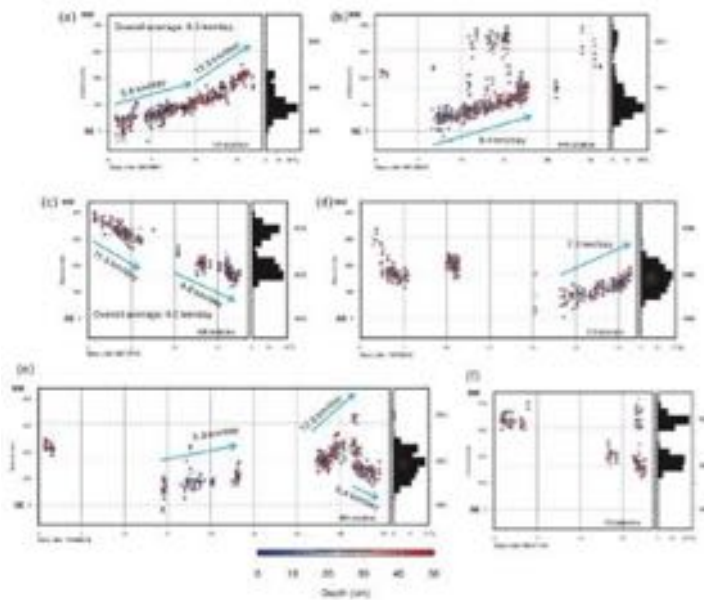


Fig. 4.20: Migration of ETS in Cascadia. [Kao et al., 2009]

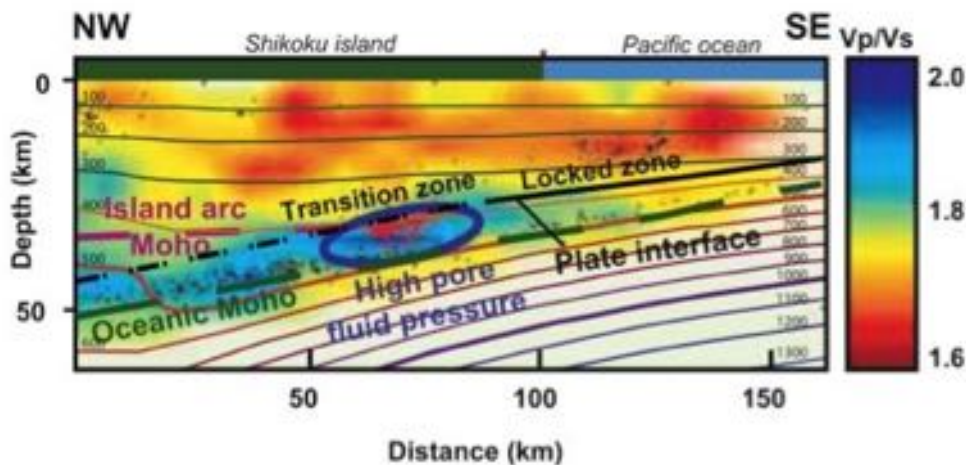


Fig. 4.21: Earthquakes (black dots) and low frequency events/ETS (red dots) overlaying a v_p/v_s map. The ETS events correspond to areas of high pore fluid pressure. [Burlini et al., 2009]

ETS has been an area of active recent research, largely due to the implications for seismic hazard [Dragert et al., 2004]. Specifically, the discovery of ETS changed the way that megathrust faults are thought to be loaded. Rather than being loaded continuously by constant convergence between two plates, megathrust loading is now thought to have a saw-tooth component where faults are loaded from below during the tremor events and loading decreases during the quiet periods. The discovery of this stress-release mechanism has provided another potential constraint on the lower-limit of megathrust rupture propagation, allowing for better informed estimates of the largest expected earthquake in a given subduction zone.

4.1.4. Crustal structure and seismicity of North Cascades

GE JIN

This section is basically a summary of Van Wagoner et al. [2002], which is based on the results of a joint inversion of local earthquake locations and crustal seismic velocity around the Seattle area. Figure 4.22 shows a map of *P*-wave velocity at 2.5 km depth in this area, together with the major fault locations and geological units.

The local stress environment mainly is controlled by the clockwise rotation of Oregon block relative to the North American plate, and the subduction of the Juan De Fuca plate. Locally, the shallow stress field is dominated by a N-S trending compression, while the deeper (sub-crustal) structure

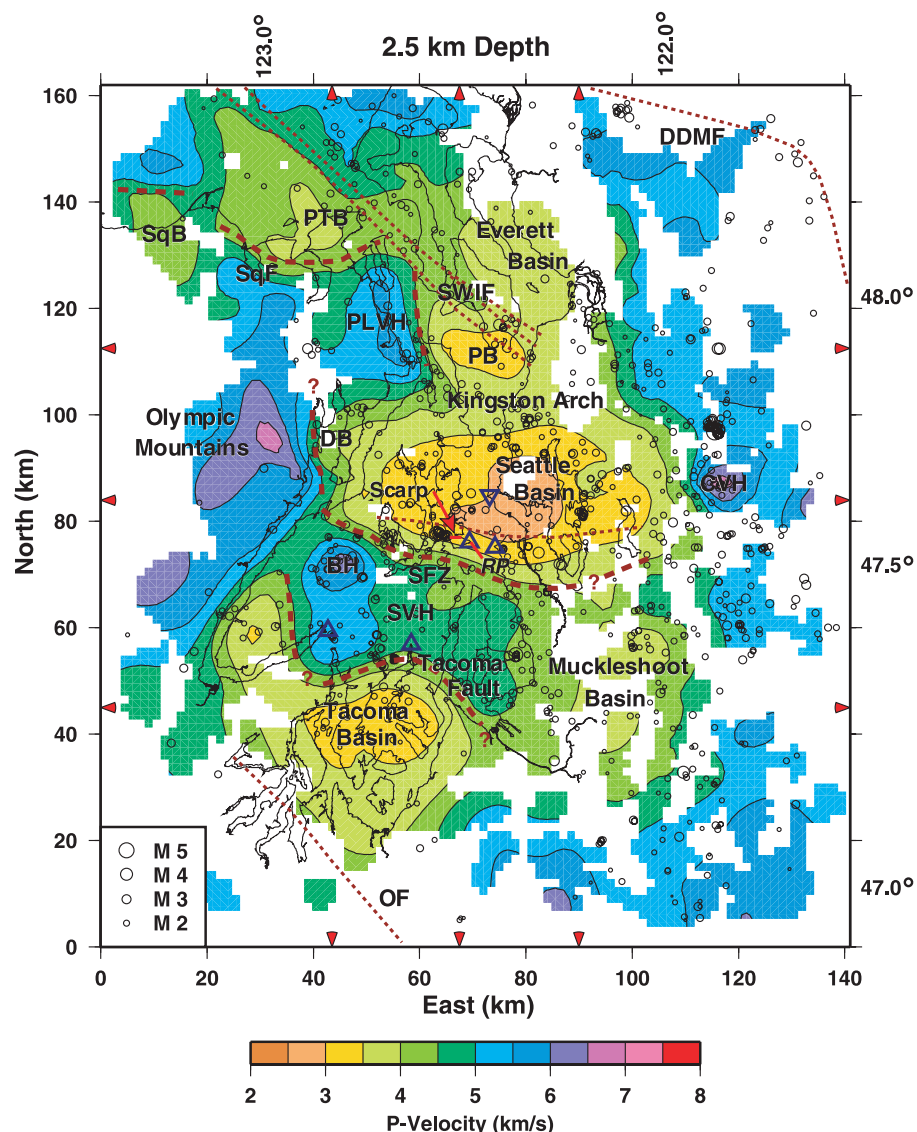


Fig. 4.22: *P*-wave velocity map at 2.5km depth. Black open circles are earthquake locations.

is mainly controlled by the eastwards subduction. As a result, the seismicity in this region can be divided into two groups: the crustal events with the P-axis (compressional axis) trending mainly N-S direction (Figure 4.23), and deep earthquakes related to subduction.

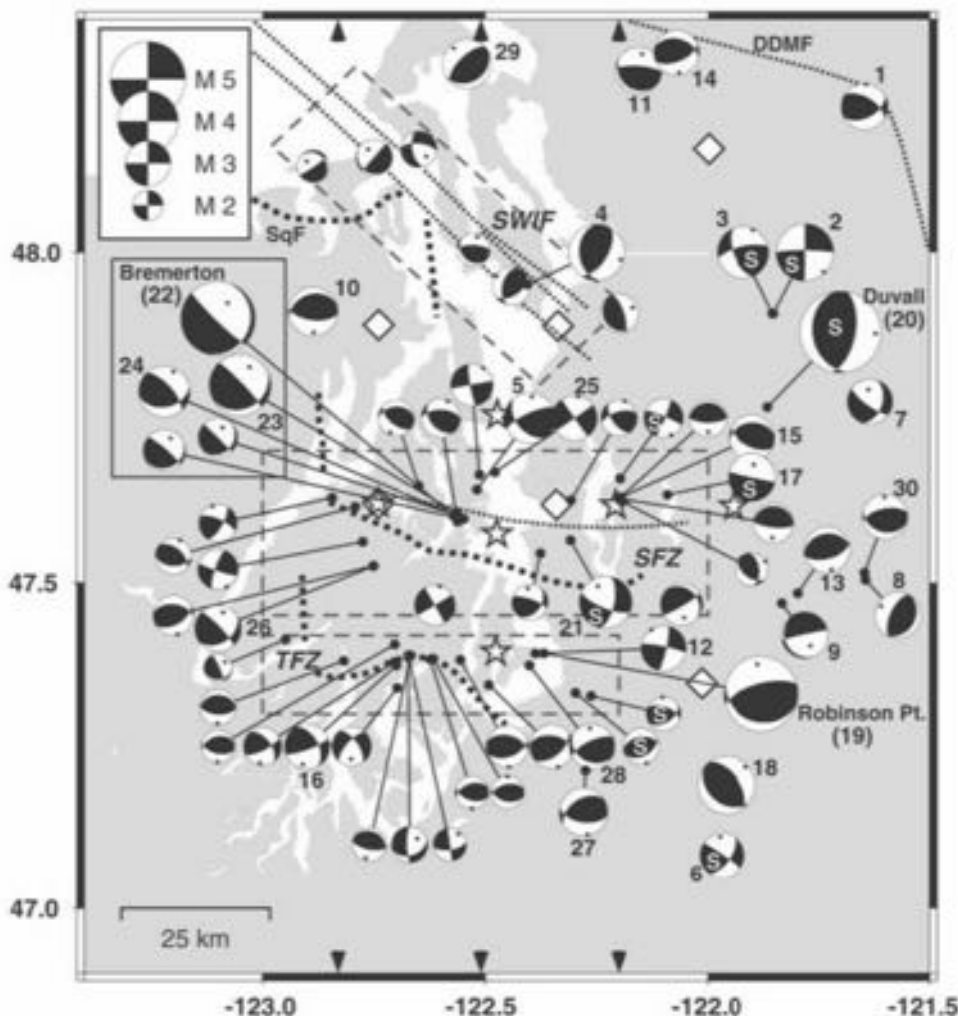


Fig. 4.23: Focal mechanisms of the local earthquakes

From the seismic velocity structure (Figure 4.22) we can easily identify different geological units. The sedimentary basins are associated with slow anomalies, and they are separated by several E-W trending velocity highs which are either anticlines or uplifted by the surrounding thrust faults. The Olympic mountains are associated with fast velocities because they contain Crescent Formation basalt and basement.

The local seismicity mainly concentrates between the depths of 15 to 25 km within the central part of the study area; these earthquakes are interpreted as occurring within the Crescent basement. The focal mechanisms reveal primarily strike-slip and thrust events, with N-S P-axes that have average plunge less than 20°, as shown in Figure 4.23.

The Seattle fault zone (SFZ) is associated with frequent shallow earthquakes and could be seismically hazardous.

4.1.5. Volcano Seismology

YANG ZHA

Volcanic eruptions have great societal impacts and often cause significant human and economic losses. Seismic signals preceding and during volcanic eruptions can help us understand their physical mechanisms better and facilitate forecasting volcanic hazard. Compared with tectonic earthquakes, which are usually generated by releasing the stress built up due to relative plate motion, volcanic earthquakes have a large variation of focal mechanisms, many of which are ambiguous (Figure 4.24). Volcanic earthquakes also have distinctive signal characteristics.

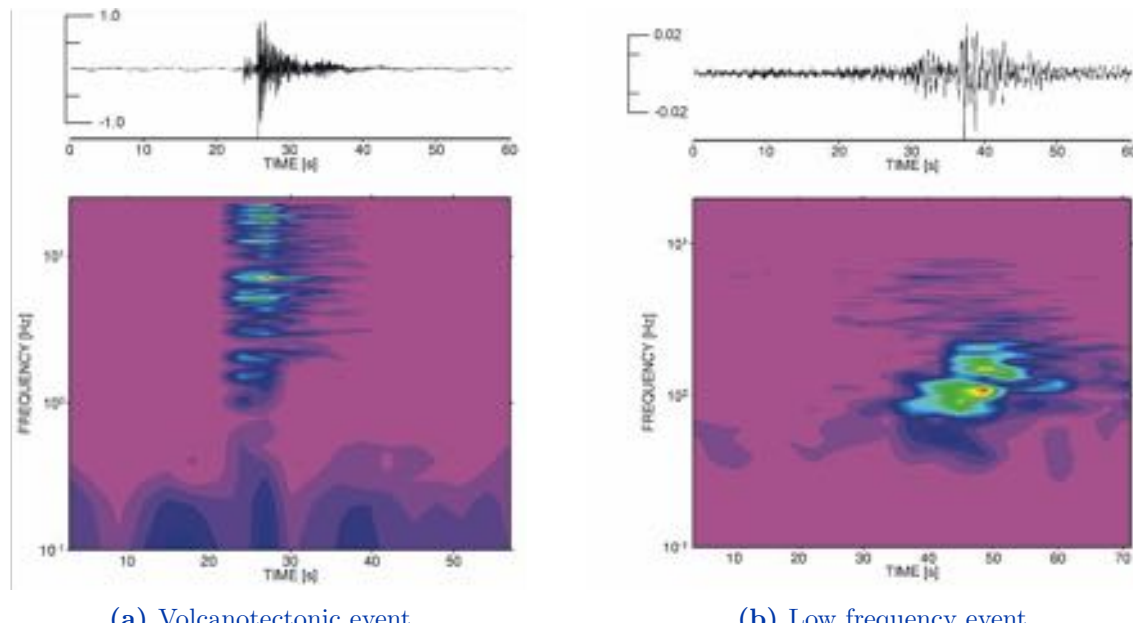


Fig. 4.24: Both events are from Mt. Merapi, Indonesia. [Wassermann, 2002]

Volcanic seismic signals can be generally divided into two main categories: transient and continuous signals [McNutt, 2005]. Within the category of transient signals, the major relevant events are volcanotectonic (VT) earthquakes and low frequency (LF, or long period, LP) events. VT earthquakes are thought to have a double couple shear failure mechanism, similar to a tectonic earthquakes. Deep (> 2 km) VT events are characterized by clear onset of P - and S -wave arrivals and high frequency content (> 5 Hz). Shallow (< 2 km) VT events, on the other hand, have more emergent P wave but no clear S -wave arrival. By contrast, LF events usually have a weak high frequency onset, followed by quasi-monochromatic oscillations. LF events are believed to be induced by the opening and resonating of cracks as magmas are moving in the shallow part of the volcano [Wassermann, 2002]. Other types of transient signals include hybrid events (combination of VT and LF events), explosions and rockfalls.

Volcanic tremor is the most common continuous seismic signal. Volcanic tremor signals can last between minutes and months and are very narrow band. Nearly all volcanoes show tremor at different stages of their eruption and volcanic tremor is the preferred parameter for diagnosing immediate hazard in volcano early eruption warning. Harmonic tremors have nearly constant energy at a few resonance frequencies (Figure 4.25), while spasmodic tremors have higher or more broadband

frequency content and exhibit pulsating signals.

Nearly all volcanic eruptions are preceded by some kind of seismic activity. However, seismic activity does not directly indicate the timing of an oncoming eruption. Seismic activity may begin months or hours before an eruption, making effective temporal forecasting a challenge. McNutt [1996] reviewed the generic volcanic earthquake swarm model (Figure 4.26). In the generic model, high frequency VT earthquake swarms begin first in the eruption cycle, reflecting brittle failure of the country rock near the volcano due to increasing magmatic pressure or transport of magma from depth. When magma arrives at shallow depth, volatiles begin to exsolve from the magma, altering its rheology and acoustic properties. Thus, at shallow depth the signals generated by magma movement are rich in low frequencies. The appearance of LF events and tremor are followed by a period of quiescence, with relatively low seismicity rate, before the final volcanic eruption. The difficulty for accurately forecasting an eruption lies in the lack of a deterministic precursor shortly before the eruption.

On May 18, 1980, Mount St.Helens in Washington erupted catastrophically after 59 days of increased seismicity. The sequence started on March 20, 1980, when an M=4 event occurred. Seismicity rate quickly increased to eight M > 4 event per hour on March 27. The seismicity rate then gradually decreased, with no immediate precursors in the hours before the catastrophic eruption (Figure 4.27). However, it is believed that the shaking of a 5.1 earthquake uncapped the volcano and initiated the eruption.

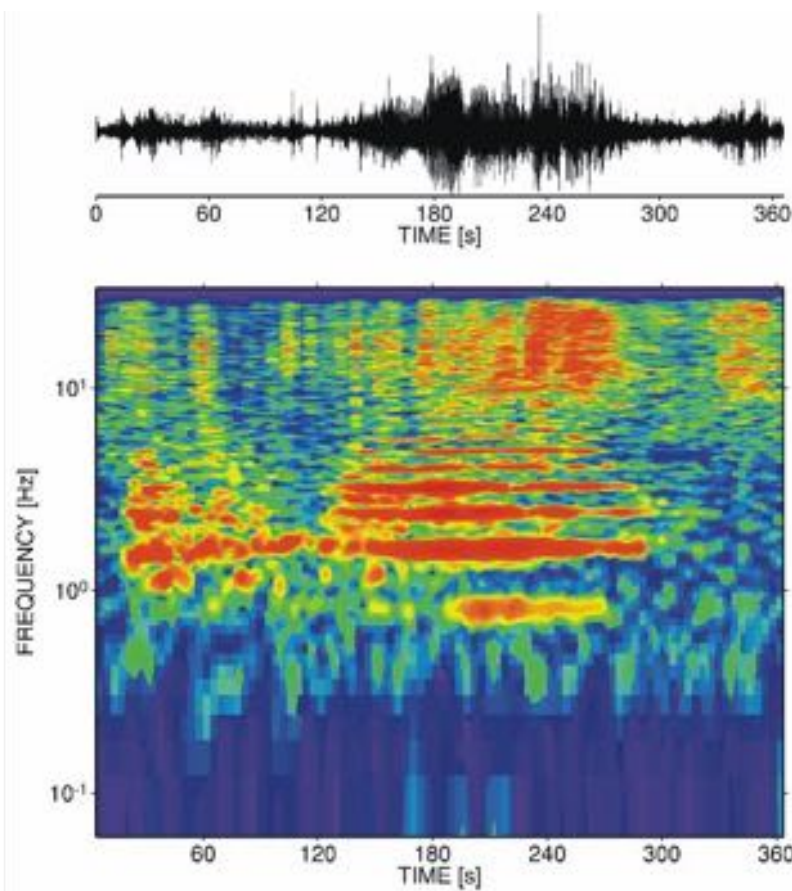


Fig. 4.25: Example of a waveform and spectrogram of harmonic tremor from Mt. Semeru, Indonesia. [Wassermann, 2002]

The difficulty for accurately forecasting an eruption lies in the lack of a deterministic precursor shortly before the eruption.

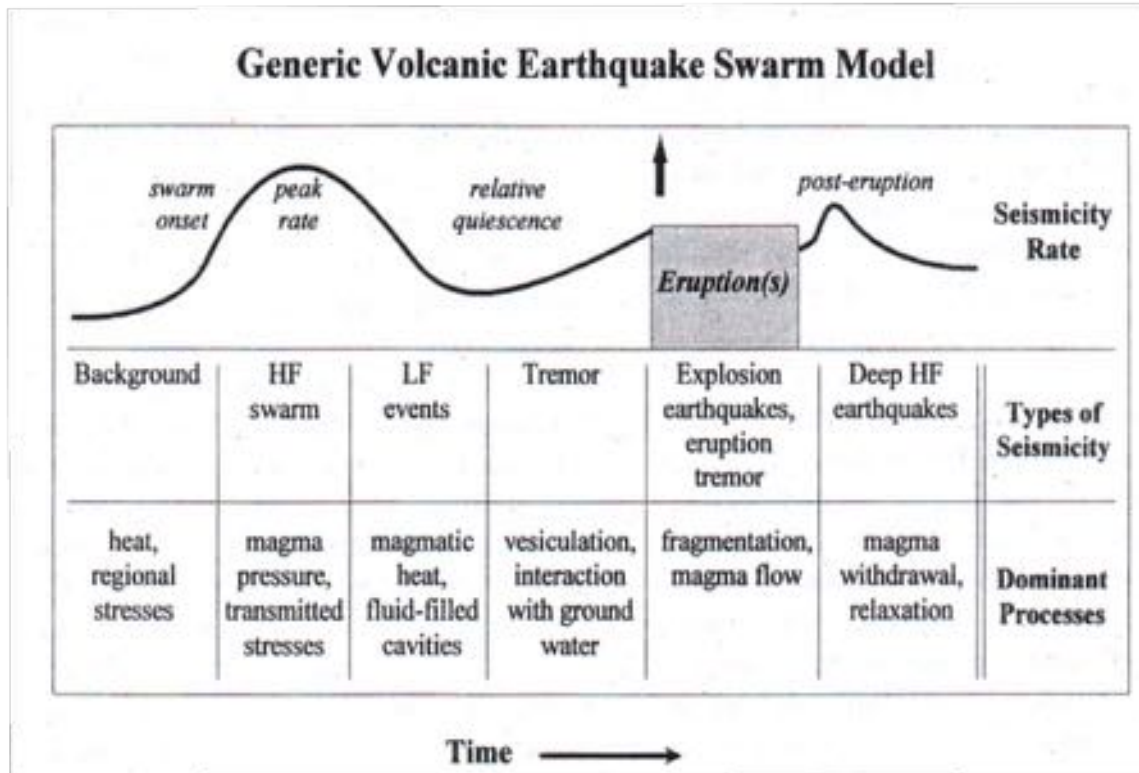


Fig. 4.26: Schematic diagram of the time history of a generic volcanic earthquake swarm model. [McNutt, 1996]

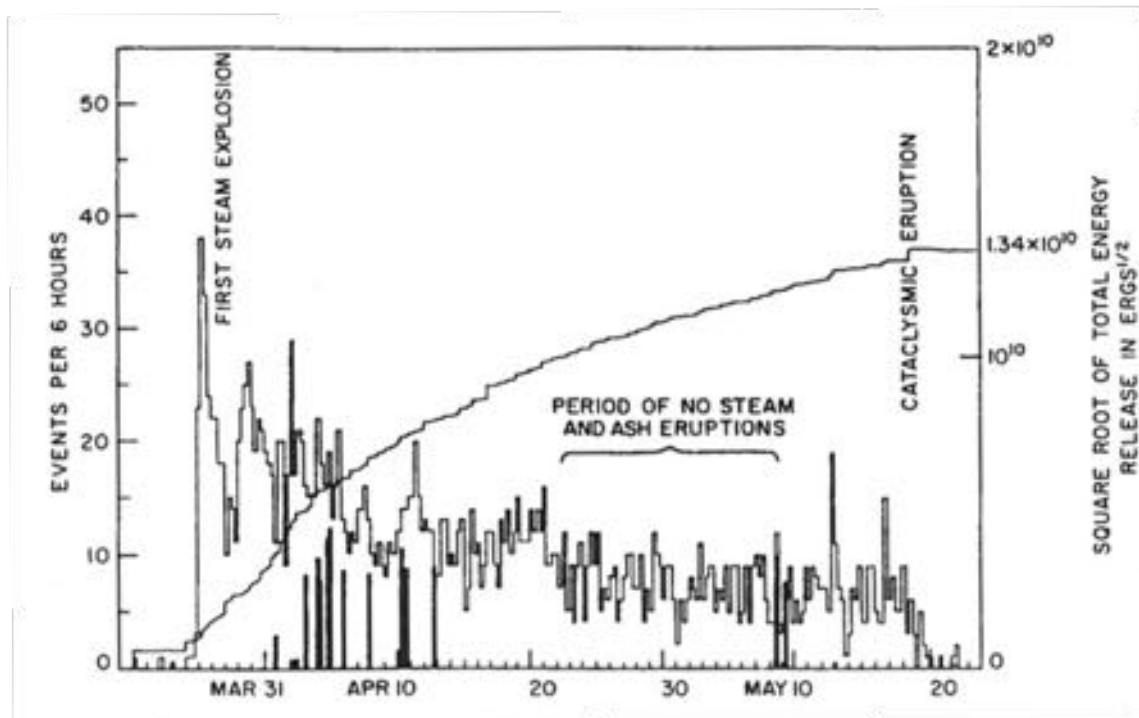


Fig. 4.27: Counts of earthquakes $> M 2.5$ preceding and during the 1980 Mount St. Helens eruption. [McNutt, 1996, Malone et al., 1981]

4.2. Volcanic Features

4.2.1. Mt. Rainier

CHLOE GAO

Mount Rainier is an active stratovolcano that, at 4393 m height, is the highest peak of the Cascade Range. Its geological features, high elevation, hydrothermal alteration, icecap, and glacier-fed radial valleys also make it the most dangerous volcano in the Cascades. When it erupts, Mount Rainier could produce tephra, lava flows, pyroclastic flows and surges, as well as lahars that could pose a greater threat than the eruption itself (Figure 4.28).

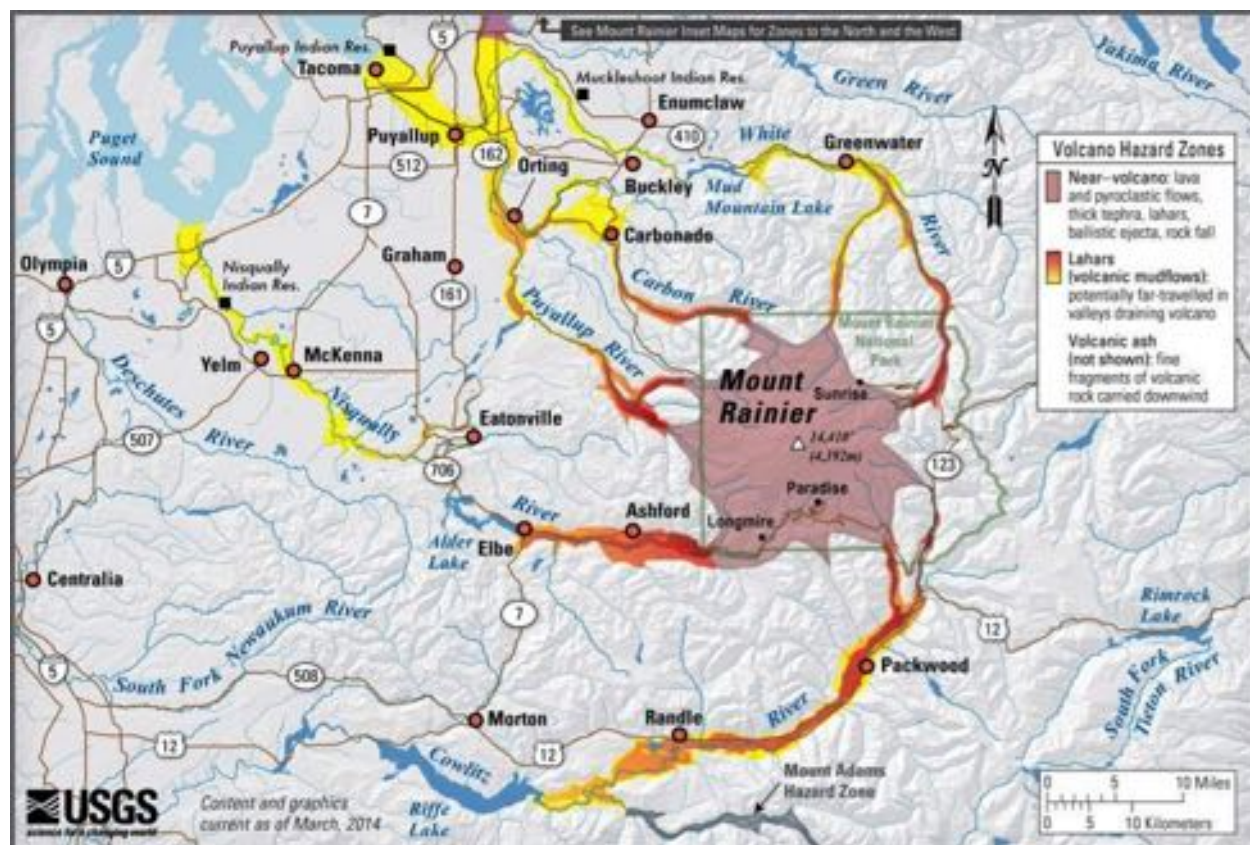


Fig. 4.28: This map shows potential impact area for ground based hazards during a volcanic event in Mount Rainier.

Volcanic eruptions usually produce plumes of gases mixed with solid particles of rocks. These particles rise together with the hot gases until reaching a height at which they are no longer buoyant. At that point, tephra/volcanic ash (the particles in the plume) falls, covering a large area. Wind carries the particles away from the vent; the particles' size and the fall deposit thickness decreases as with increasing distance from the vent.

Compared to other Cascades volcanoes, Mount Rainier is not a significant source of tephra. In the past 10,000 years, relatively few eruptions at Mount Rainier have left layers of pumice (tephra) from gas-rich magma. The many volcanoclastic sediments between the pumice layers were produced by gas-poor magma or steam-driven eruptions.

Tephra is a mixture of hot gas with rock particles that is less dense than air, but sometimes eruptions produce a similar mixture more dense than air. Whereas the low density gas-particle mixture rises to produce tephra, the higher density mixture flows along the Earth's surface to 1) produce pyroclastic flows, if it is made up mostly of rock particles (gas-poor), or 2) produce pyroclastic surge, if it is made up mostly of gas (gas-rich). Pyroclastic flows and pyroclastic surge usually happen simultaneously, the former has high density and its path is controlled by topography, the latter, being made up of mostly gas, has low density, and its path is not so much controlled by topography. They are highly dangerous due to their typical high speeds of more than 10 meters per second, and at points close to the source, their speeds can reach greater than 100 meters per second. These flows are particularly hazardous due to their high temperature, often exceeding 300°C.

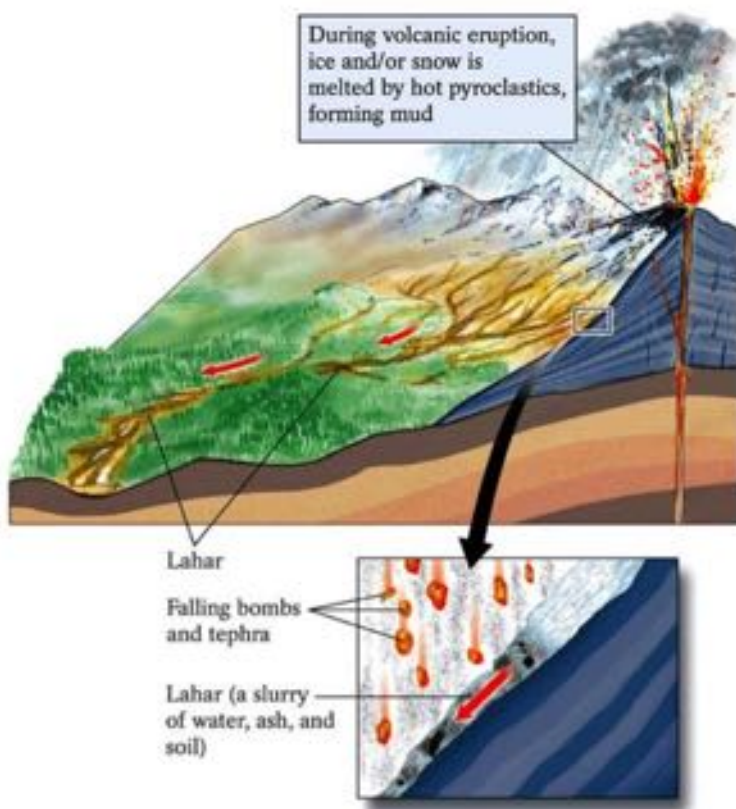


Fig. 4.29: Schematic of eruptive hazards.

Mount Rainier has few deposits of both pyroclastic flows and surges. Two possible reasons are: 1) Mount Rainier does not produce much of them; 2) most of the pyroclastic flows and surges meet snow and ice on their way downhill, melt them, and mix in to form debris flows.

Lava flows are flows of molten rock that were erupted non-explosively and flow downhill to cool and solidify. Slow-moving, very viscous andesite lava flows make up most of Mount Rainier. Even though they destroy everything upon contact, their main hazard is their interaction with snow and ice, causing melting to and consequent debris flows and floods. The only lava flow that erupted from Mount Rainier built the summit cone, and probably the ridges of the Emmons Glacier as well.

As mentioned before, lava flows and pyroclastic flows melt snow and ice giving rise to the greatest volcanic hazard: debris flows. These slurries of water and sediments (Figure 4.29) are sometimes called mudflows and in volcanic events, lahars. They flow at speeds that range from tens to hundreds of miles per hour and destroy things upon contact. There were at least 60 debris flows at Mount Rainier in the past ten thousand years. Debris flows can be cohesive or non-cohesive, the former form from clay from chemically altered rocks, and the latter from a mixture of pyroclastic flows and lava flows with snow and ice melt.

Mount Rainier has two types of lahars:

- **Meltwater-generated lahars:** Mount Rainier has much glacial ice; pyroclastic flows and lava flow melt the ice and form these lahars.
- **Landslide-generated lahars:** Landslides can happen when magma intrudes into a volcano or may be triggered by earthquakes. Magma releases heat that creates acidic water that can convert volcanic rock into weak rocks by hydrothermal alteration. When these weak clay-rich rocks fail in landslides, they form lahars.

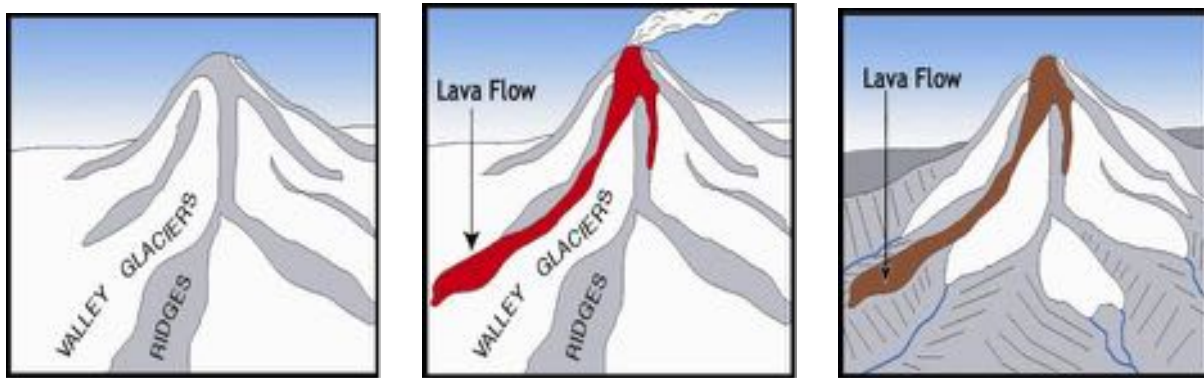


Fig. 4.30: Formation of ridges modulated by the presence of glaciers at Mt. Rainier.

Mt. Rainier also has been formed by its glaciers. During the Pleistocene, glaciers on Mount Rainier were much more voluminous than they are in present day, and they filled all of the valleys on the mountain (Figure 4.30). Lava flows travel along the path directed by topography and of least resistance. They flowed along the sides of the glaciers and piled on top of each other. Over time, the glaciers slowly melted and exposed the lava flow ridges that now perversely appear to have flowed along the topographic highs.

4.2.2. Mt. St. Helens

CELIA EDDY

Mount St. Helens is an active stratovolcano located in the Cascades Volcanic Arc. It is located within the Gifford Pinchot National Forest, about 100 miles south of Seattle. Water from the volcano drains into three main river systems: The Toutle River to the north and northwest, the Kalama River to the west, and the Lewis River to the south and east.

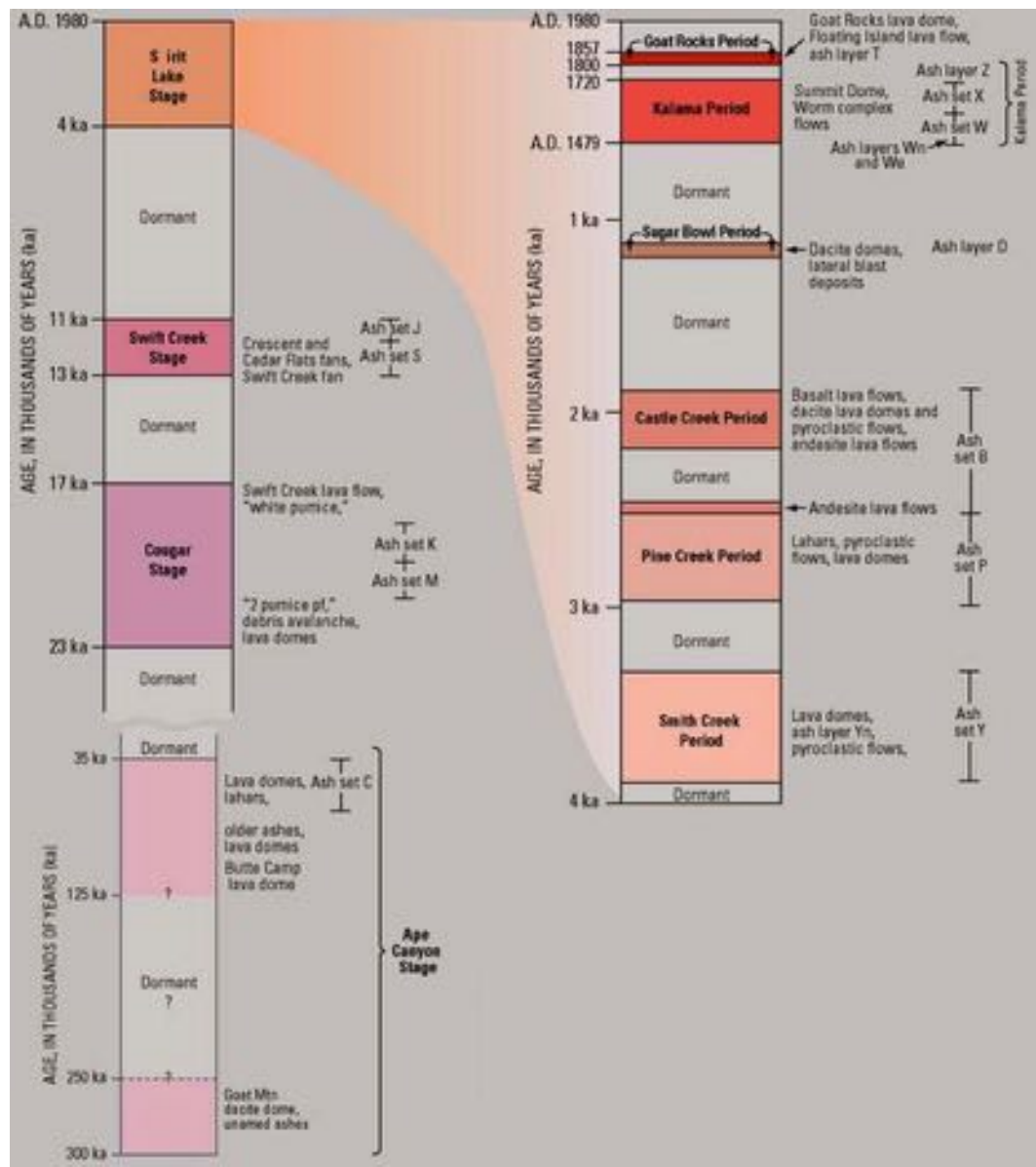


Fig. 4.31: Eruptive stages of Mt. St. Helens. Figure from USGS.

Subduction of the Juan de Fuca plate beneath the North American Plate at ~ 40 mm/year leads to arc volcanism along the northwest coast of the United States. The volcanic arc extends from Lassen Peak in Northern California to Mt. Baker in Washington, and continues even further north into Canada. Although volcanism began in the Cascades Arc about 37 Myr ago, most of the present-day volcanoes are less than 2 Myr old. St. Helens is relatively young compared to other major

volcanoes in the range; the current volcanic edifice has formed within the past 40 kyr. During the Holocene, St. Helens has been the most active volcano within the arc.

Although the present-day edifice has formed relatively recently, there is evidence for intermittent volcanism in the Mt. St. Helens region for the past 500 kyr. The eruptive history of St. Helens can be divided into four main eruptive stages, separated by dormant intervals for which no volcanic products have been recognized (Figure 4.31). In the early stages, the volcano consisted of a cluster of domes, surrounded by tephra and debris fans of fragmented volcanic rocks.

The first stage, Ape Canyon, extends from the onset of volcanism in the region at ~300 kyr until 35 kyr ago. During the Ape Canyon stage, volcanism produced a cluster of lava domes, mostly west of the present edifice. Ash layers extend over a large area indicating the occurrence of explosive eruptions. The second stage, Couger, persisted from 23 kyr - 17 kyr. Many explosive eruptions occurred during this stage, ejecting large amounts of ash, forming lava domes and flows, pyroclastic flows, large debris avalanches, and lahars. The largest observed lava flow in St. Helens eruptive history occurred during this stage; the Swift Creek Flow, up

to 200 m thick, reached 6 km down the Swift Creek drainage. The third stage, Swift Creek, lasted between 13 kyr - 11 kyr. During this stage there were many pyroclastic flow and lahars, and expansive tephra deposits. Together, these three make up the ancestral stages of St. Helens volcanism. The current stage of volcanism, Spirit Lake, began 4000 years ago.

The eruptive stages differ primarily in the composition in the erupted lavas. Ancestral lavas consist of a mixture of dacite and andesite, while the modern lavas are more diverse, ranging from olivine



Fig. 4.32: Cryptodome on the north flank of St. Helens in the days preceding the eruption on May 18, 1980.



Fig. 4.33: Ash cloud during the May 1980 eruption of St. Helens. View from the south; lateral blast not evident.

basalt to andesite. This indicates progression from a simple to a more complex magmatic system as the volcano matured; more mixing occurs between silicic and mafic pools of magma as the volcano evolved.

Intermittent volcanism in the Spirit Lake stage is divided up into shorter eruptive periods. For this stage there is better preservation of deposits and good age estimates from carbon and tree-ring dating. As a result, we have a more detailed eruptive history of the present stage. The Spirit Lake stage consists of seven periods of volcanism. The Smith Creek period occurred between 4000-3300 years ago, during which time the most voluminous eruption in St. Helens history happened. This eruption was approximately four times larger than the eruption in 1980. The Pine Creek period occurred from 2900-2500 years ago and was characterized by smaller-volume eruptions. During the Castle Creek period, from 2500-1600 years ago, there was a change of composition of the erupted lavas. Olivine and basalt are present in lavas from this stage, indicating intrusion and mixing with a mantle-derived magma that contaminated the crustal magma system. During this period, clusters of domes from earlier periods were transformed into the classic cone-shaped composite volcano through multiple basalt and dacite flows erupted within a short period of time. During the Sugar Bowl period around 1200 years ago, there was short-lived growth of three lava domes and there is evidence for lateral blasts similar to the one that occurred during the 1980 eruption. The Kalama period, from 1479-1720 A.D., was characterized by large-volume eruptions that lead to growth of a large dome at the summit. From 1800-1857, the Goat Rocks period was the last period of activity before the modern eruptive period. The last significant eruption before 1980 occurred in 1857.



Fig. 4.34: Before and after the May 1980 eruption of St. Helens, looking from the North.

In the spring of 1980, activity began at St. Helens. The main eruption was preceded by an earthquake swarm beginning on March 20, 1980. This swarm lasted for several months, during which time there were several small eruptions at the volcano. Magma intruding into the volcano caused the north flank to swell and form a cryptodome. By the time of the eruption on May 18th, the north flank of the volcano had swelled almost 500 feet (Figure 4.32).

On May 18, 1980 at 8:32 A.M. there was a magnitude 5.1 earthquake. A few seconds later, the north flank of the volcano collapsed, leading to the largest debris avalanche in recorded history during which 2.5 cubic km of material travelled at speeds of 170-250 km/hr. This collapse reduced the confining pressure on the partially molten, volatile rich rock, leading to the lateral blast and

eruption. The pyroclastic flow from the eruption flattened vegetation and buildings over an area of 600 square km, and traveled at 250-1080 km/hr. Tephra was erupted for more than 9 hours, with the ash plume reaching more than 20 km into the atmosphere (Figure 4.33). The ash then moved east at about 60 mph and was deposited over 11 states. Lightning generated in the ash cloud also started forest fires. Ice, snow, and water on St. Helens mixed with debris to form lahars, which flowed down the Toutle and Cowlitz rivers. In total, the eruption released 24 Mton of thermal energy and ejected more than 0.67 cubic miles of material. Figure 4.34 shows pictures taken just before and after the eruption. The elevation of the summit was reduced from 9677 ft to 8365 ft.



Fig. 4.35: Whaleback feature seen in the crater on St. Helens in February 2005.

The eruption caused extensive damage. 57 people were killed, including USGS volcanologist David Johnston. 250 homes, 45 bridges, 15 miles of railways, and 185 miles of highway were destroyed, causing \$1.1 billion in property damage. Ash fallout also destroyed crops over a large region.

In the years following the 1980 eruption, a new dome grew (Figure 4.34). A glacier also formed in the crater of St. Helens the winter after the eruption. It grew in thickness rapidly at a rate of 4.3 m/year. The rapid growth was due to both heavy winter snowfall and sun-shading by surrounding cliffs to the south of the glacier. It was divided in half by recent volcanic activity between 2004-2008. Figure 4.35 shows a whaleback feature in February 2005, part of new growth of the dome. Since 1980, vegetation has come back quickly in the area surrounding the volcano. Of the volcanoes in the Cascades Volcanic Arc, St. Helens is considered to be one of the most likely to erupt in the future.

4.2.3. Columbia River Basalts

NATALIA ZAKHAROVA

The Columbia River Basalt Group (CRBG) is a large igneous province (LIP) that covers over 70,000 square miles of the Pacific Northwest (Washington, Oregon and Idaho), with a total estimated volume of 53,700 cubic miles [Martin et al., 2005]. The flood basalts erupted from linear fissures between 17.5 and 6 Ma ago (late Miocene-early Pliocene). The CRBG consists of a sequence of over 300 tholeiitic basalt flows, the majority of which erupted during a period of 2.5 million years (17-14.5 Ma ago). During this peak activity, many individual flows exceeded 1,000 km³ in volume, and traveled hundreds of miles from their vent system [Martin et al., 2005]. Despite their huge volumes and great distances traveled, the stratigraphic units in the CRBG can be reliably identified and correlated on a regional basis, mostly due to a remarkable geochemical homogeneity of individual flows [Hooper, 2000]. Based on the combination of geochemical composition, paleomagnetic properties, and lithology, the CRBG is divided into five main formations (in ascending stratigraphic order): the Imnaha, Grande Ronde, Picture Gorge, Wanapum, and Saddle Mountains Basalts (Figure 4.36), each of which is further subdivided into members and flows [Reidel, 1998, e.g.]. The most voluminous formation is the Grande Ronde Basalt, erupted 16.5 to 14.5 Ma ago, which constitutes about 85% of the CRBG volume and consists of 17 individual members [Reidel et al., 1989].

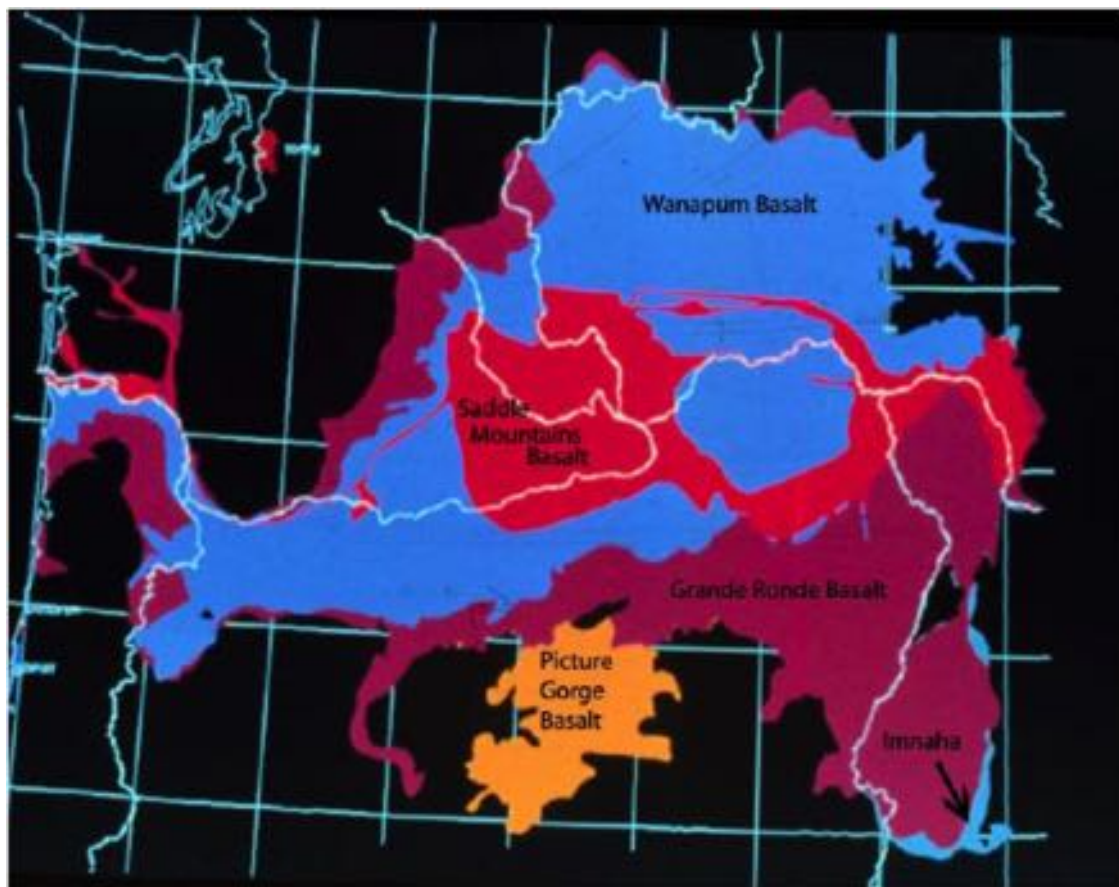


Fig. 4.36: Geologic map of the Columbia River Basalt Group [Martin et al., 2005].

As with other LIPs, formation of the Columbia River flood basalts is commonly attributed to a mantle plume, or hotspot activity. Although this theory is not universally accepted, the CRBG is generally associated with the passage of the North American plate over the Yellowstone hotspot [Camp, 1995, Smith et al., 2009, e.g.], as it best explains the eruption of such a large volume of tholeiitic basalt within such an unusually short period and within such a restricted area [Hooper et al., 2007]. Unlike the younger magmatism of the Snake River Plain, also produced by the Yellowstone hotspot, the CRBG lies off the projected track of roughly southwestward plate motion (Figure 4.37). Camp [1995] explained this apparent discrepancy by a two-phase plume spreading model consisting of a wide plume head and a more focused plume tail (Figure 4.37). According to this model, the CRBG, along with the Oregon Plateau lavas, were produced by the plume head that rapidly spread outward under a thinner transitional lithosphere and accreted terrains, westward of the continental craton roughly 16-15 Ma. The subsequent Snake River Plain magmatism, in contrast, was produced by the plume tail and closely tracks the southwestward motion of the North American plate.

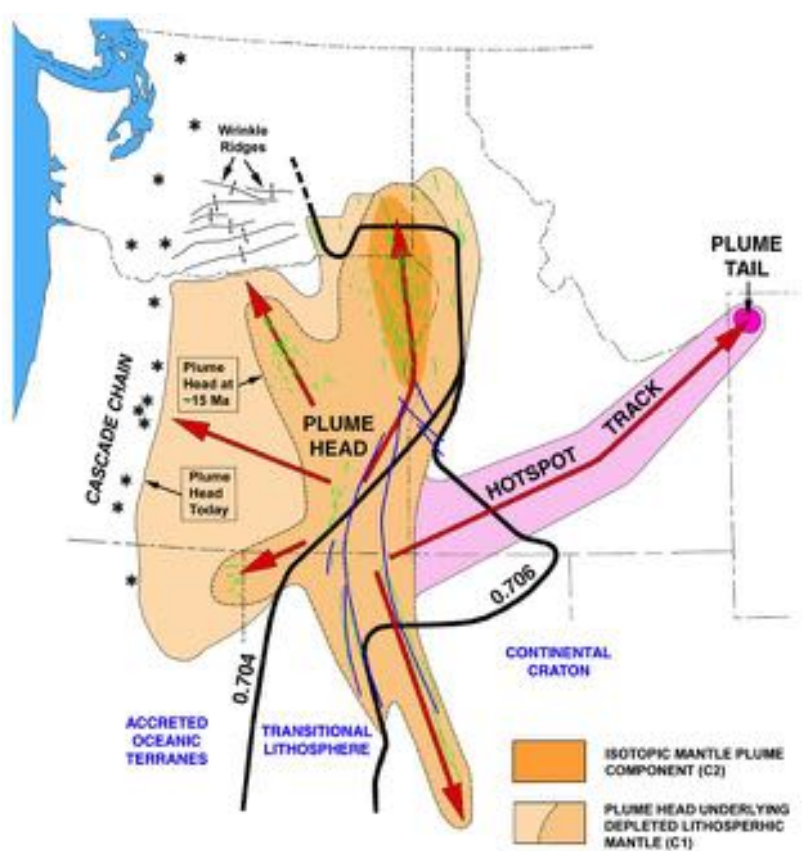


Fig. 4.37: A model of the spread of the Yellowstone mantle plume [Camp and Ross, 2004], showing (1) the approximate position of the plume head after impingement and rapid spreading (15.0 Ma), (2) its approximate position today after moderate rate spreading associated with asthenospheric drag and counterflow above the subducting plate, (3) the track of the plume tail connecting that CRBG with the modern-day position of the Yellowstone hotspot. The short lines located above the area of first-stage spreading are surficial dikes; the longer curvilinear lines indicate the linear magnetic anomalies, which are thought to be buried intrusions or keel dikes. The approximate boundaries of distinct lithospheric domains beneath the plume head are delineated by the $^{87}\text{Sr}/^{86}\text{Sr}$ isopleths.

The Columbia River Basalt Group is located in the intermontane region between the Cascade Range and the Rocky Mountains of the Pacific Northwest, and forms a broad plain also called the Columbia Plateau [Martin et al., 2005, e.g.]. In the central part of the plateau, the CRBG is underlain predominantly by early Tertiary continental sedimentary rocks and overlain by late Neogene and Quaternary fluvial and glacial-fluvial deposits. Farther east, the CRBG is directly underlain by metasediments of the Paleozoic continental margin [Reidel et al., 2002].

The Columbia Plateau consists of three structural-tectonic regions or subprovinces: the Yakima Fold Belt, the Palouse Slope, and the Blue Mountains (Figure 4.38). The Yakima Fold Belt is the western portion of the Columbia Plateau, where CRBG flows and sediments were folded and faulted during and after the flows were emplaced. This resulted in a series of anticlinal ridges and synclinal valleys that controlled the thickness and distribution of subsequent CRBG flows. Immediately east of the fold belt, the basalts erupted on the Palouse Slope, which is a gently westward dipping paleoslope of pre-Miocene age overlying the North American craton [Reidel, 1998]. The Palouse Slope is significantly less deformed, with only a few faults and low-amplitude, long-wavelength folds. The Blue Mountains is a broad NE trending anticlinorium that extends over 250 km from the Oregon Cascades to the eastern part of the Columbia basin and was growing during the eruption of the basalt. It overlies the Mesozoic accreted terrains and Eocene and Oligocene volcanic rocks. Dikes and vents for the CRBG occur in the Palouse Slope and Blue Mountains provinces [Reidel, 1998].

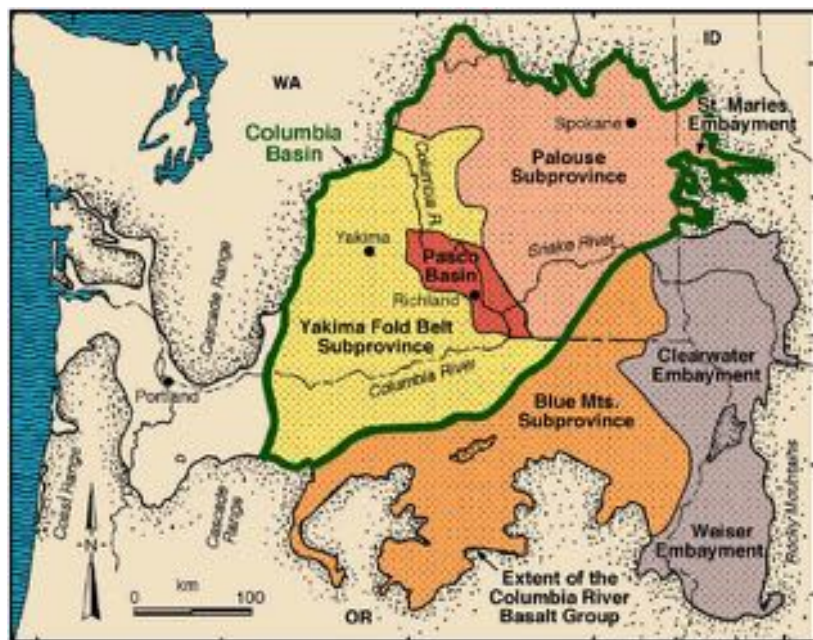
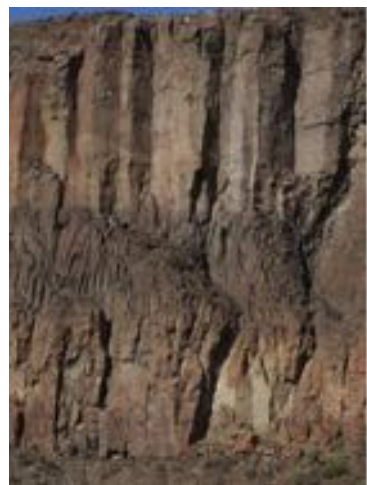


Fig. 4.38: Principal structural features of the Columbia River Flood Basalt province [Martin et al., 2005].

[Reidel, 1998]. The Palouse Slope is significantly less deformed, with only a few faults and low-amplitude, long-wavelength folds. The Blue Mountains is a broad NE trending anticlinorium that extends over 250 km from the Oregon Cascades to the eastern part of the Columbia basin and was growing during the eruption of the basalt. It overlies the Mesozoic accreted terrains and Eocene and Oligocene volcanic rocks. Dikes and vents for the CRBG occur in the Palouse Slope and Blue Mountains provinces [Reidel, 1998].



(a) A simplified flow schematic [Long and Wood, 1986].



(b) Low frequency event.

Fig. 4.39: Colonnades and entablature in a CRBG flow

Each CRBG formation consists of tens to hundreds individual flows, each representing a single extrusive event. A single flow may cover as much as $5,000 \text{ mi}^2$ and extend for over 300 miles in one

direction [Ho and Cashman, 1997, Reidel, 1998]. A single flow typically averages around 90 ft in thickness but can be as thick as 300 ft. Most flows display complex patterns of internal structures that include porous, glassy and brecciated flow tops, and dense flow interiors, usually dominated by colonnades and entablatures (Figure 4.39) [Long and Wood, 1986, e.g.]. Colonnades consist of relatively well-formed polygonal columns that separated by cooling joints, and usually occur in the basal portion of flows, although they can also constitute the entire flow thickness. The columnar joints result from contraction during slow cooling, as the columns grow perpendicular to the cooling front (resulting in vertical columns in subhorizontal flows). Entablatures are characterized by a greater abundance of cooling joints that are more randomly oriented than in colonnades, and they often occur further away from cooling boundaries.



Fig. 4.40: Examples of columnar joints in the Columbia River Flood Basalt.

In simple terms, formation of the colonnades happens as follows: As a lava flow cools, the temperature field within it changes in accord with Fourier's law for heat conduction. The cooling front

moves inside the body causing thermal contraction cracks to occur perpendicular to isothermal surfaces. The networks of interconnected tension fractures tend to divide solids into prisms bounded by three to eight sides (the pentagons are, in fact, as abundant as commonly known hexagons [Budkewitsch and Robin, 1994]). The joints in the colonnades also commonly exhibit surface markings known as striae [Grossenbacher and McDuffie, 1995]. They represent a single increment of joint growth. As the result, the long slender joint faces of individual columns are built from a stacked succession of short crack segments. In general, large columns signify slower cooling while narrow columns result from faster cooling. Many CRBG flows exhibit spectacular colonnades that vary from about a foot to many feet in diameter (Figure 4.40).

4.3. Surface Processes

4.3.1. Tsunamis and Surface Expressions of Earthquakes

JONATHAN GALE

Paleotsunamis and their parent megathrust earthquakes have been part of native stories for hundreds of years. Specifically the 1700 Cascadia earthquake can be characterized in some detail by these stories (Figure 4.41).

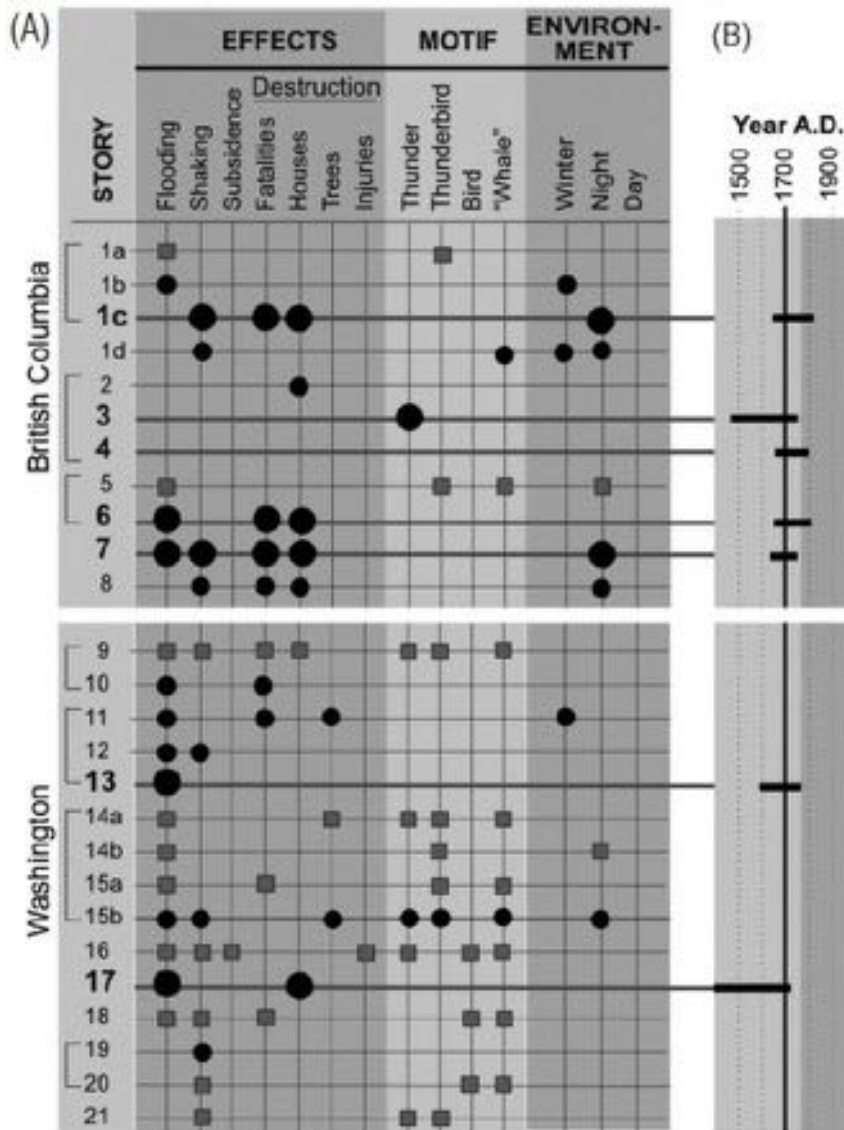


Fig. 4.41: Story Motifs related to Cascadian Earthquake and Tsunami Phenomena [Ludwin et al., 2005]

The entire Cascadia subduction zone appears to have evidence for paleotsunami activity. As part of the trip itinerary, we pass along parts of the coast that have this evidence for past megathrust earthquakes - notably the low lying Aberdeen area in Grays Harbor County. Several sites in this area have paleotsunami evidence for such earthquakes.

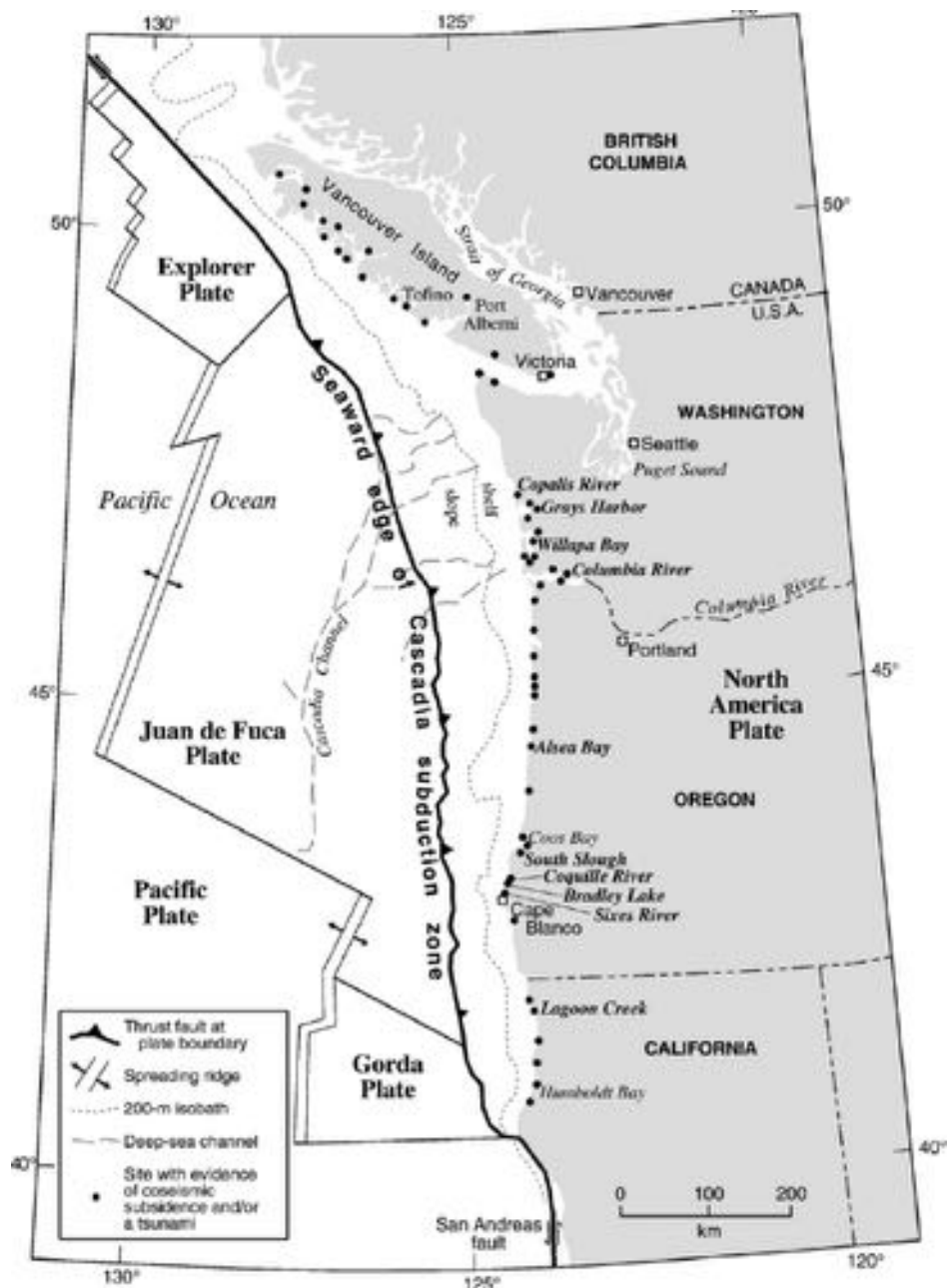


Fig. 4.42: Map of Cascadia Subduction Zone with land level changes and paleotsunami locations.

Paleotsunamis have been recorded in the low areas along the Pacific coast and Puget sound. Buried trees that died during these events are used for dating the 1700 earthquake. For older events, radiocarbon was used to measure the ages of the washed up marine material. Japanese records of tsunamis have also been used to match the local sand flows on the Cascadia margin with specific dates and times.



Fig. 4.43: Photo from Oregon's Salmon River of a peat layer overlain by tsunami sands which are covered by grey-green layers of marine plants and sediments. Two Native American campfire pits buried by the peat, paleotsunami deposit. (From PNSN)

4.3.2. Glacial History and Features of Washington

MIKE WOLOVICK

Glaciers are solid-state rivers. At the most fundamental level, they function as a drainage system for snow, just as rivers function as a drainage system for rain. In mountainous terrain, snow accumulates at high elevations where it is cold year-round. Glacial flow transports this snow to lower elevations, where it melts during the summer months. The runoff enters the normal fluvial system and eventually reaches the ocean, completing the hydrologic cycle.

In a valley glacier setting, the glacier is generally divided into two regimes based on elevation: the accumulation zone and the ablation zone, separated by the equilibrium line altitude (ELA) [Cuffey and Paterson, 2010]. In the accumulation zone, higher on the mountain, net snowfall exceeds net melt over the annual cycle. In the ablation zone, lower down, net melt exceeds net snowfall. Both zones experience snowfall in the winter, but in the ablation zone summer melt eats away all the winter snow and cuts down into the underlying glacial ice. In the accumulation zone, summer melt (if it occurs) is insufficient to remove winter snow. The excess snow is compacted by the pressure of subsequent years' snowfall (and by in situ refreezing of summer melt) until it is metamorphosed into glacial ice, which has a characteristic blue color.



Fig. 4.44: Crevasses on the lateral shear margin of Nisqually Glacier on Mount Rainier. Glacier surface is partially covered by avalanche debris. Picture by Mike Wolovick.

The ELA also marks a transition in strain rate within the glacier, and thus in deformation structures observable in the field. Within the accumulation zone, the glacier experiences extension and

thinning, while in the ablation zone the glacier experiences compression and thickening [Cuffey and Paterson, 2010]. If a glacier is in balance, the thickening or thinning is exactly compensated by surface mass balance. In the accumulation zone the loss of thickness due to extension is replenished by net annual snowfall, while in the ablation zone the gain of thickness due to compression is planed off by net annual melt. However, glaciers are rarely in balance, so fluctuations in thickness and length are common. In addition, local strain rates differ from the average within that region of a glacier due to flow around bedrock obstacles, curves in the glacier's path, and junctions with tributaries or distributaries.

The upper surface of a glacier contains many deformation structures that are readily observed from a distance. The most common are crevasses (Figure 4.44), or tensile cracks. Crevasses open when the glacier experiences extension, and the tensile stress causing extension is greater than the overburden pressure of the ice. Crevasses form in the accumulation zone, around local flow irregularities, and in shear margins along the trunk of a glacier (shear can be broken down into perpendicular tension and compression along the principal axes). Once formed, crevasses are advected downstream by glacial flow, and may be subsequently overprinted by newer generations of crevasses at alternate orientations. As a result, glacier surfaces often become progressively more broken up and chaotic as they travel downstream.

Glaciers erode bedrock by abrasion and quarrying [Clarke, 2005]. Abrasion works through the action of small rocks embedded in the underside of the glacier. As the glacier slides over the bedrock, these small rocks (themselves eroded from further upstream) gouge out grooves and striations in the rock surface. Quarrying works through fluctuating water pressure. When the ice slides over a bedrock bump, a cavity forms in the lee of the bump that is usually filled with water. Subglacial water pressure varies both in response to fluctuations in meltwater input and as a result of unforced fluctuations in the subglacial hydrologic system. Varying water pressure creates time-varying stresses in the rock that result in fracture.

Glaciers transport sediment either through direct ice flow or through subglacial water. Avalanches onto the upper surface of a glacier are common in mountainous regions and this debris is transported downstream and eventually deposited at the terminus. Sediment produced by subglacial erosion is ploughed downstream by ice sliding and can also be transported upwards into the body of the glacier by compressional deformation in the ablation zone. When meltwater fluxes are high in the summer, subglacial water forms an organized hydrological network with a dendritic network of pressurized conduits that carry water to the terminus [Clarke, 2005]. Water flow rates within these conduits can be quite high, and they are therefore capable of transporting sediment in a similar manner as energetic subaerial rivers.

Sediment transported by direct ice flow is generally composed of till. Till is a poorly sorted mixture of everything from mud to boulders [Clarke, 2005, Cuffey and Paterson, 2010]. It is roughly similar to what you would get if you applied a jackhammer and an industrial bulldozer to the rock and dumped the results in a large pile. Till deposits include lateral moraines, deposited at the sides of the glacier trunk, medial moraines, deposited in the middle of the glacier trunk (often downstream of the confluence of two tributaries), and terminal moraines, deposited at the downstream end (terminus) of the glacier trunk. Lateral and medial moraines are parallel to ice flow, terminal moraines are perpendicular to ice flow. Very large boulders (up to house-sized) known as erratics can be deposited out of place by ice flow.

Sediment deposited by glacial meltwater has similar characteristics to other fluvial sediments. Un-

derneath the glacier itself it may form eskers, which are sinuous mounds of sediment deposited by subglacial conduits [Clarke, 2005]. Once the meltwater emerges from the glacier's terminus into the proglacial environment, it may deposit sediment into deltas, fans, etc, and otherwise behaves like a fluvial system from that point on.

The Pliocene has seen cyclical fluctuations of large-scale ice sheets on the North American continent. The cyclicity is related to orbital forcing of the Earth's climate, but the response of the climatic and glaciological systems to the forcing is nonlinear and has changed over time. In the beginning of the Pliocene, the ice age cycle was dominated by the 40 ka obliquity cycle [Lisiecki and Raymo, 2005]. About one million years ago, for reasons that are still debated, the ice age cycle transitioned to the 100 ka eccentricity cycle.

During the last glacial period, North America was covered by the Laurentide ice sheet in the east and the Cordilleran ice sheet in the west. Modern-day Washington State was partially covered by the Puget Lobe of the Cordilleran ice sheet. This lobe covered Puget Sound and the surrounding lowlands but did not penetrate significantly into the Southern Cascades or the Olympic Mountains (Figure 4.45) [Porter and Swanson, 1998]. Smaller valley glaciers were widespread in the mountains.

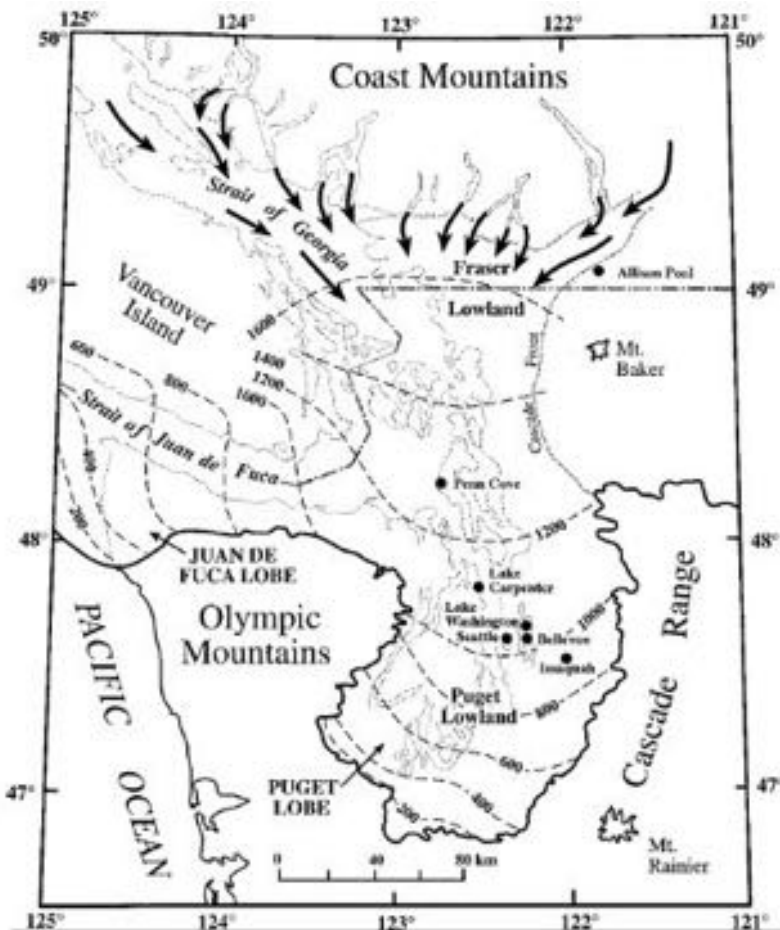


Fig. 4.45: Map of the Puget lobe of the Cordilleran ice sheet. From Porter and Swanson [1998].

Smaller valley glaciers were widespread in the mountains.

4.3.3. Olympic National Park Rainforest

KEREN MEZUMAN

Temperate rainforests are defined by their mid-latitude (temperate) location and climatic conditions: annual precipitation of $>140\text{cm}$ and a mean annual temperature of $4 < T < 12^\circ\text{C}$. The Olympic National Park (Figure 4.46) falls under this category, and receives the most rainfall in the continental US. The park is a UNESCO World Heritage Site and has been an area of conservation since the early 1900s. The three main sections of the park are the Hoh, Queets and Quinault Rainforests, all of which are along valleys that were carved during the last ice age ($\sim 13,000$ ybp).

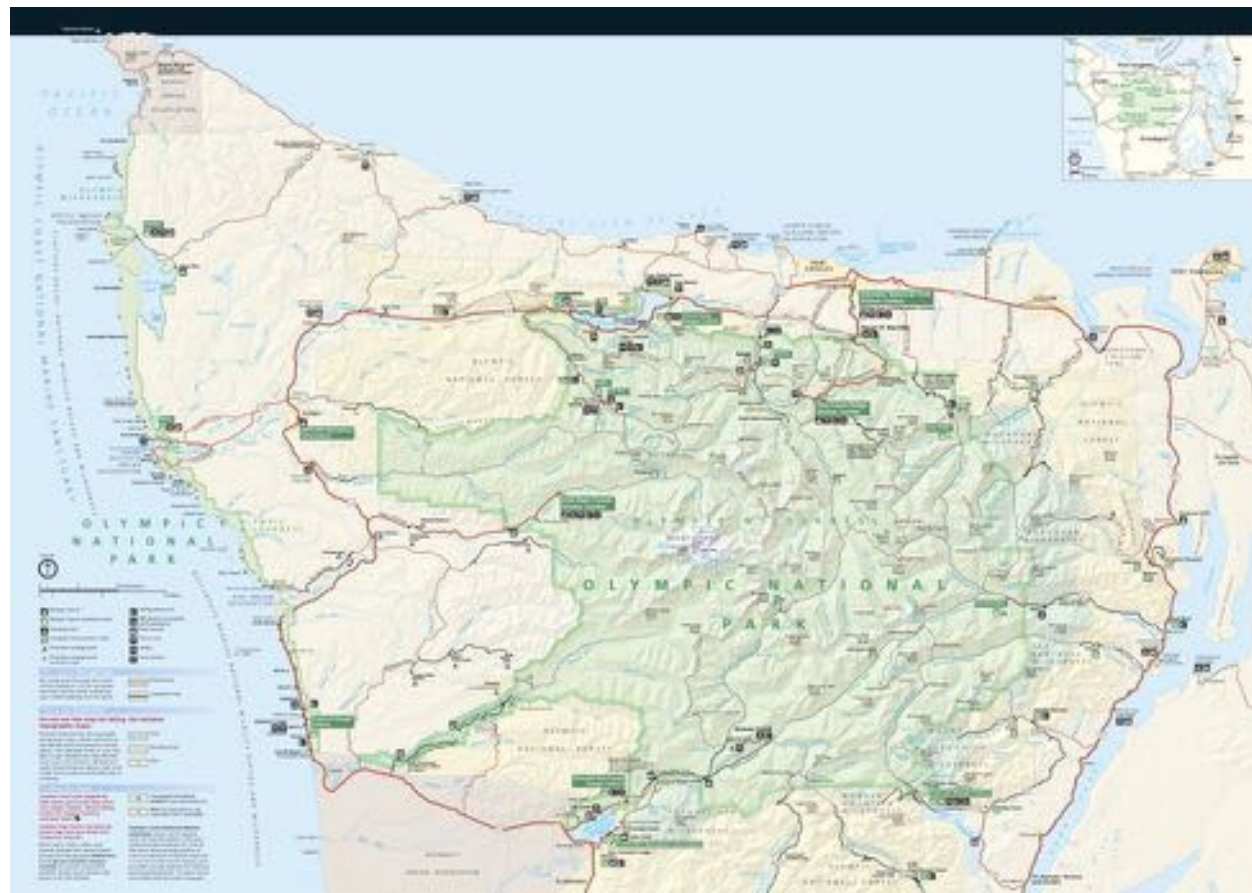


Fig. 4.46: Map of the Olympic Peninsula. Source: National Park Service 2014

The weather forcing is mainly driven by moist air carried from the Pacific Ocean, which condenses and rains on the peninsula as the Olympic and Cascade Mountains block the west-flowing air. The park experiences about 400cm annually [Witczuk et al., 2013]. Summer time is the dry season, and heavy night fog supplies moisture to the system. The Cascade Mountains to the Northeast protect the Olympic peninsula from cold Arctic air masses, keeping the temperature fluctuation mild. Another significant water supply system is snow meltwater, as some of the mountains on the Peninsula get as much as 10 meters of snow annually. Stream chemistry has been shown to be effected by bedrock weathering rather than precipitation chemistry, dominated by Ca , HCO_3 and SO_4 [Edmonds and Blew, 1997].

The diverse ecosystem of the Olympic Park is attributed to its remote location. Mountainous geography, the peninsula structure and effects of changing sea level, and glaciers made it hard for settlers to thrive. The most prominent feature of the park is its diverse and abundant population of trees. There are more than 12 different conifers within its territory, including Douglas Fir, Sitka Spruce, and Western Hemlock. These conifers have a successful germination rate of about 1/10K [NOAA, 2014b]. Some of the trees have been growing for hundreds of years, with occasional individuals thought to be older than one thousand years. The massive old trees reach over 200 feet tall. The iconic feature of the forest is the wide variety of epiphytes (plants growing upon other plants); more than 130 species of moss, lichens and ferns are found in this rainforest. Lichens are a symbiotic system of a fungus and photosynthetic algae, and their sensitivity to acidity is used as a direct measure for rain acidity. The endemic fauna thrives within the deadwood that slowly decays and supplies plentiful nutrients. An annual mean of 3594kg/ha of overstory litterfall was measured at the park [Edmonds and Murray, 2002]. The number of different species of insects is unknown, and many microhabitats in the park are yet to be surveyed. Among the park's unique wildlife is a population of fewer than one thousand Olympic Marmots. This population has been on the decline for the past 30 years, with evidence implicating the invasion of non-native coyote predators [Witczuk et al., 2013]. The Roosevelt Elk is another native to the area and its population has slightly risen thanks to conservation efforts, to about 4000-5,000 individuals. The elk population has an indirect effect on riverbank erosion due to interaction with riparian communities [Beschta and Ripple, 2008].

The air quality at the Olympic National Park is relatively good. However, some air masses originating in Asia transport pollution across the Pacific and into the park and, together with industrial sites across the State, affect the ecosystem of the park. Elsewhere, it has been observed that increasing amounts of nitrogen deposition disrupts the eco-balance allowing weed species to grow faster, affecting lichen communities (lichens adapted to low nitrogen are being replaced by lichens adapted to a more polluted environment). Surveys in Olympic Park have found that current nitrogen deposition rates in the park are low and have not affected lichens [Geiser and et al., 2010]. These findings are supported by research on nitrogen deposition effects on diatom communities, with water chemistry indicating ultra-oligotrophic with ammonia and nitrate concentration often at or below detection limits [Sheibley et al., 2014]. Topospheric ozone is transported to the Park from nearby urban areas and trans-Pacific sources [Barna et al., 2000]. Current concentrations are below levels known to be harmful to plants, but levels are being regulated as extreme air pollution events get more frequent with shifts in climate. Contaminants such as mercury, pesticides, and industrial by-products have been observed in snow, sediment, vegetation, and fish [Frenzel et al., 1990, Landers et al., 2008]. Mercury concentrations in fish are among the highest of eight western national parks, exceeding safe consumption thresholds for wildlife and humans [Mast et al., 2010].

4.3.4. Waterbodies and Coastal Ecology of the Olympic Peninsula

NANDINI RAMESH

The two major water bodies visited on this trip were the Olympic Coast and the Puget Sound. The Olympic Coast is the stretch of coastline of the Olympic Peninsula bordering the Pacific Ocean, and the Puget Sound is the large estuarine water body separating the Olympic Peninsula from the rest of Washington State.

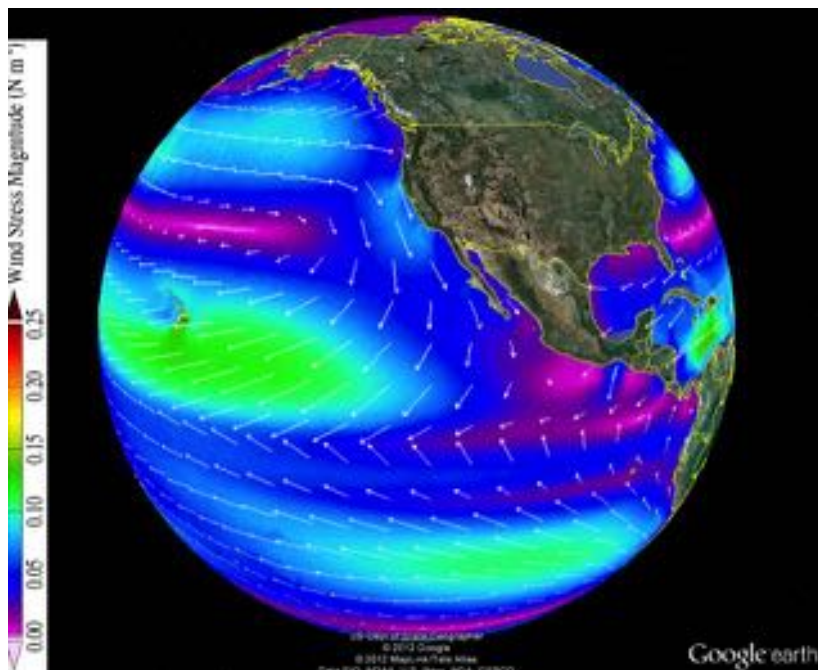


Fig. 4.47: Pattern of wind stress near the Pacific coast of the USA.



Fig. 4.48: Juan de Fuca Eddy.

ocean to the surface, enabling the growth of phytoplankton, which in turn supports entire ecosys-

The Pacific coast of the Olympic Peninsula stretches for 73 miles (117.5 km) and comprises both rocky and sandy beaches. The strong winds of the region produce high-energy waves at the coast. This has resulted in erosional features along the coast such as sea stacks, cliffs, caves, and arches, seen in particular on the stretch of Ruby Beach.

The Olympic Coast lies in the region of transition from westerly winds at lower latitudes to southwesterly winds at higher latitudes, near the boundary between the North Pacific subtropical gyre and the North Pacific polar gyre (Figure 4.47). The divergent winds at the coast resulting from this transition drive an upwelling eddy that remains in place near the Olympic Coast known as the Juan de Fuca Eddy [NOAA, 2008] (Figure 4.48).

Regions in the ocean dominated by upwelling motion are highly biologically productive. Photosynthesizing phytoplankton form the base of the food chain in many ocean ecosystems. While the sunlight that they require is abundant at the surface of the ocean, nutrients are not. Upwelling motion brings nutrients from lower depths in the

tems. In addition, runoff from coastal water bodies can supplement coastal regions with nutrients. The Juan de Fuca Eddy draws nutrients both through upwelling motion and from the outflow from the Puget Sound through the Strait of Juan de Fuca into the Pacific Ocean [NOAA, 2008], producing a region of high nutrient concentrations that facilitates the growth of an abundance of species in the region.

There are four types of habitats found along the Olympic Coast [NOAA, 2013]:

Open Ocean: The open ocean habitat receives its nutrient supply, as described above, from the circulation of the Juan de Fuca Eddy. At the base of the food chain are autotrophic phytoplankton species. The food chain ranges from these to large marine mammals such as harbor seals, orca, and migratory humpback whales.

Kelp Forests: The continental shelf is dominated by seasonal kelp forests. The base of the food chain here are bull kelp (Figure 4.49) and giant kelp, which grow rooted to the seafloor. They die out in winter and are regenerated through rapid growth in the summer with growth rates of up to 2 feet per day for bull kelp. The kelp forests provide an important nursing ground for young fish, as the tall stalks both provide shelter and concentrate nutrients. In addition, they shelter several species of crabs, sea snails, starfish, sea cucumbers, and sea otters. These forests also provide feeding grounds for several species of seabird.



Fig. 4.49: Underwater photograph of bull kelp. Image credit: Royal British Columbia Museum.

Rocky Reefs: The jagged rocks of these environments serve to concentrate nutrients. They are particularly important for mollusk species.

Intertidal Zone: The intertidal zone in this region forms many tidal pools as a consequence of the jagged, rocky topography. These tidal pools support a variety of species, such as sea anemones, sea



Fig. 4.50: Schematic of the intertidal zone environment.

cucumbers, starfish, and mussels. Further inland, this environment also supports crabs, barnacles, and limpets. The subdivisions of the intertidal zone are shown in Figure 4.50.

Puget Sound is an inland estuarine system with source waters from the rivers of the watersheds of the Olympic Peninsula and the Cascades. Rather than being a result of erosion by water bodies of the region, the topography of the Sound is a product of erosion by the glaciers and ice sheets of the Last Glacial Maximum [NOAA, 2014a]. Puget Sound is divided into five regions: the Strait of Juan de Fuca, Hood Canal, Central Puget Sound, South Puget Sound, and Whidbey Basin (Figure 4.51). The total length of the Sound is 95 miles (153 km), and ranges in width from 1 to 3 miles (1.6-4.8 km).

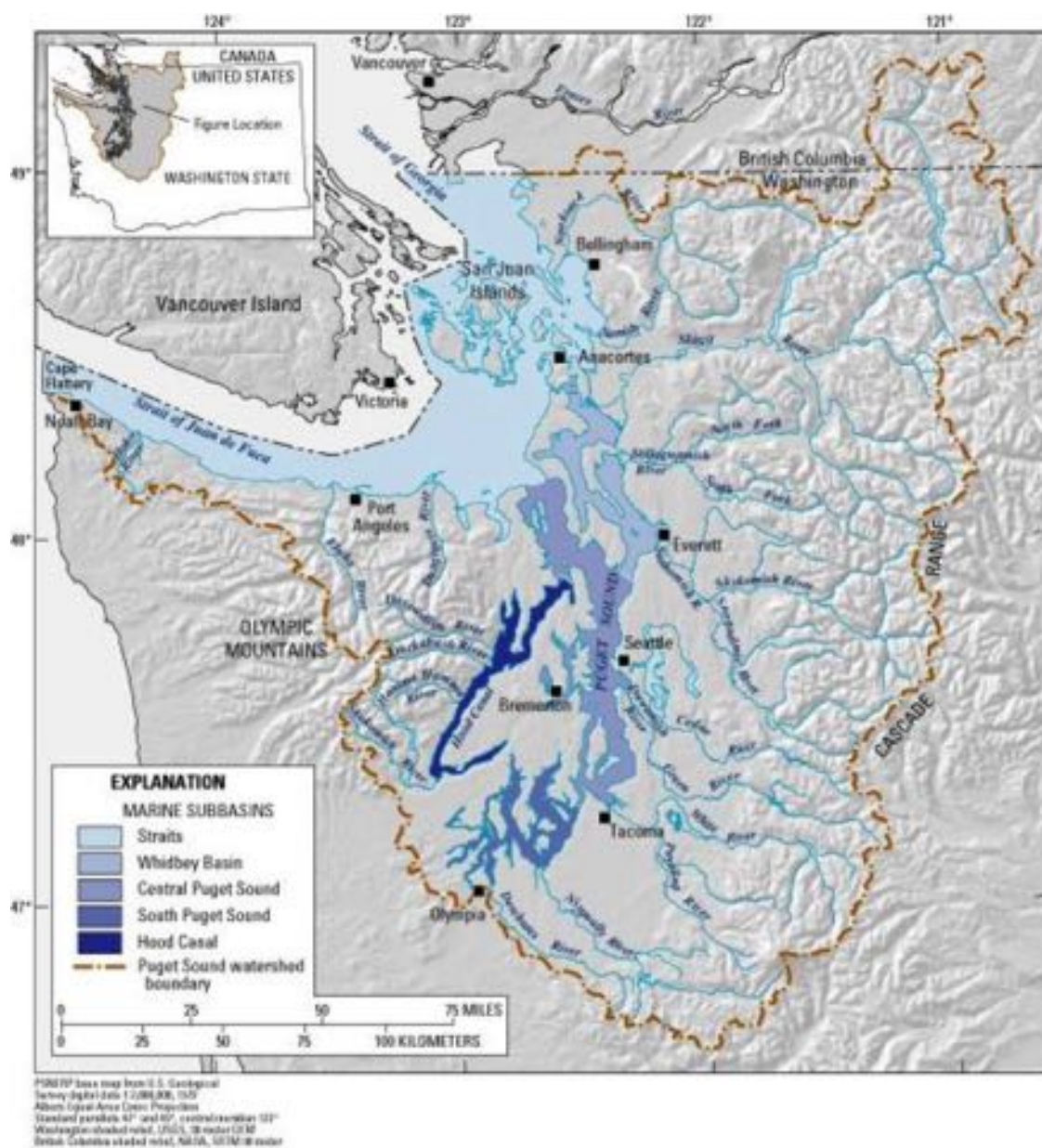


Fig. 4.51: Subdivisions of the Puget Sound from USGS Washington Water Science Center.

The high precipitation and presence of glaciers in the region surrounding the Puget Sound give rise to numerous small rivers, which feed into the Sound. An estimated 20% of the total volume of the Sound is replenished each year by inflow from rivers [NOAA, 2014a]. The following is a list of the rivers that drain into the Puget Sound: Cedar, Duwamish, Nisqually, Skokomish, Hama Hamma, Duckabush, Dosewallips, Skagit, Stillaguamish, Snohomish, Puyallup.

The complex topography of the Sound acts both to amplify and dampen the tides. The circulation is primarily tidally driven, with velocities as high as 5 m/s reached in narrower parts such as Deception Pass [Lincoln, 2014]. The waters are also well-mixed as the result of tidal action. This can be seen in the temperature variations throughout the Sound, which range only from 8-17 °C, as well as in salinity, which ranges from 27-30 psu.

The tides have a pair of highs and a pair of lows each day. These are known as the Higher High Water (HHW), Higher Low Water (HLW), Lower High Water (LHW), and Lower Low Water (LLW). Of these, the Low Waters have more variability. The tidal range also varies according to the local topography, with the general pattern being one of increasing tidal range from north to south. The highest tidal range is 4.4 m [Lincoln, 2014].

The other driver of the flow is the density difference between the salty waters of the Pacific and the fresh water of the rivers. This density difference results in a saltier inflow at depth and a fresh outflow at the surface. Tidal mixing complicates this simple flow, and results in the waters of the Sound being composed of 10% river discharge and 90% Pacific seawater [NOAA, 2014a].

The major ecosystems of the Puget Sound are the kelp forests and intertidal zones described above. There have been 221 species of fish found in the Puget Sound, including a variety of cod and salmon species [NOAA, 2014a].

5 Detailed Itinerary and Description of Sites Visited

5.1. Day 1, August 3, 2014: Ophiolite complex on Fidalgo Island

NATALIA ZAKHAROVA

- 10:10 am** Arrived at the Seattle-Tacoma International Airport, picked up rental cars
11:15 am Left the airport, drove north on I-5
11:45 am Stopped at Safeway for lunch and to buy food for the following 4 days
1:00 pm Continued driving north on I-5 toward Mt. Vernon, then turned west on Route 20 to Anacortes (Fidalgo Island)
3:00 pm **Stop 1:** the viewpoint at Cap Sante Park in Anacortes
3:40 pm Continued driving west on Fidalgo Island to Washington Park
3:55 pm **Stop 2:** Green Point, Washington Park
4:25 pm Left Green point and drove to Mt. Erie
4:45 pm **Stop 3:** Mount Erie viewpoint, Mount Erie Park
5:20 pm Left Mt. Erie and drove south to Deception Pass State Park campground

Stop 1: Cap Sante Park viewpoint in Anacortes



(a) Cap Sante Park's viewpoint



(b) An outcrop of meta-sedimentary rocks

Fig. 5.1: Cap Sante Park, viewpoint of Mt. Baker.

This stop offers spectacular 360° views of Fidalgo Bay, the City of Anacortes, marinas, and the Cascades with snow-capped Mount Baker (Figure 5.1). The viewpoint is located on a hill made up of coarse-grained sedimentary rocks about 60 million years old. Although not a part of the Fidalgo ophiolite per se, these rocks represent near-shore sediments that could be found overlaying the oceanic crust. The outcrop exhibits various sedimentary fabrics and glacial features such as

striations and glacially smoothed surfaces. One can also observe glacial till deposits down by the water to the northwest of the viewpoint, which stand out due to their lighter color and noticeably poor consolidation. Another interesting observation that can be made at this stop (as well as en route throughout the day) is the differences in vegetation on various islands scattered in the bay, which is related to bedrock geology. Ultramafic rocks, in particular, the low-crustal and mantle sections of the ophiolite complex, weather into soils poor in potassium and other essential nutrients, which cannot support vegetation. Therefore, the ophiolite islands can be recognized from the distance by their lack of vegetation.

Stop 2: Green Point, Washington Park

The name of this stop comes from the exposures of serpentinite, a metamorphosed mantle rock, found along a picturesque rocky shore in Washington park. It represents an upper-mantle section in the basal portion of the Fidalgo ophiolite. The rocks that we examined on the northern side of the beach at Green point had rusty-brown color characteristic of weathered mantle rocks in many ophiolite outcrops. We observed dunites and pyroxenites intersected by an extensive network of carbonate veins (Figure 5.2). The ophiolite rocks at this location are overlain by loose glacial deposits.



(a) Pyroxenite banding in dunite



(b) Carbonate veins.

Fig. 5.2: Mantle section of Fidalgo ophiolite at Green point, Washington Park.

Stop 3: Mount Erie viewpoint, Mount Erie Park

The rocks found on Mt. Erie represent the crustal section of the Fidalgo ophiolite that lie sequentially above the mantle serpentinite at stop 2. Here they consist mainly of diorite, a slightly more felsic rock than gabbro, commonly found in ophiolitic crustal sections. They are interpreted to represent magmas formed below a chain of subduction-zone volcanoes. U-Pb zircon ages are 167.5 Ma [Tucker, 2014]. Thus, the Fidalgo ophiolite is interpreted to represent the lithosphere of a Jurassic volcanic arc. The whole sequence was tipped on its side during accretion, so the deepest portion, the serpentinite, is now found to the west (Washington Park), the uppermost portion,

i.e. the ocean floor lavas and sedimentary rocks, is found toward the east, and the intracrustal intrusives are in the middle (Mt. Erie). The stop also offers spectacular views from small platforms on the summit knobs (Figure 5.3).



Fig. 5.3: A view south from stop 3 at Mount Erie on Lake Campbell and Skagit Bay.

5.2. Day 2, August 4, 2014: Metamorphism and Accretion

ZACH EILON

9:00 am	Review before leaving campsite and depart
10:15 am	Stop 1: Bedrock quarry near Sharpe Road
11:00 am	Stop 2: Bridges at Deception Pass and lunch
12:00 am	Lunch at overlook between bridges
1:00 pm	Stop 3: Rosario Beach, Deception Pass State Park
4:30 pm	Stop 4: Location of Oso landslide
4:45 pm	Stop 5: Stop on side of the road, 6 mi W of Darrington
6:30 pm	Arrive at Horseshoe Cove Campground and have dinner

In preparation for what we will see today, we reviewed the classic structure of oceanic crust that is expected within an ophiolite sequence, although in practice it is rarely all observed (Figure 5.4). We re-familiarised ourselves with the classification of ultramafic (Figure 5.5) and plutonic (Figure 5.6) rocks, several of which we will see today, as well as over the course of the field trip. Note the important evolutionary sequence from gabbro/diorite, through tonalite, to granodiorite, and finally granite.

Stop 1: Bedrock quarry near Sharpe Road

Outcrop in the heather on the side of the hill just below the concrete foundation.

Initial observations:

Rocks are hard and crystalline, with sugary texture. A dark-green matrix includes dark, 1-3mm crystals exhibiting 90° cleavage: these are pyroxenes.

Explanation:

The colour and the texture indicate that this outcrop consists of a de-vitrified lava; the green colours may be attributed to the minerals chlorite and epidote, which grew during metamorphism. The larger pyroxenes result from recrystallisation during metamorphism.

Summary:

This outcrop comprises meta-volcanics from uppermost extrusive sequence beneath the pillow lavas (not seen here).

Other notes:

Some trace veins also evident. Whitish colour, hard to scratch - probably quartz.

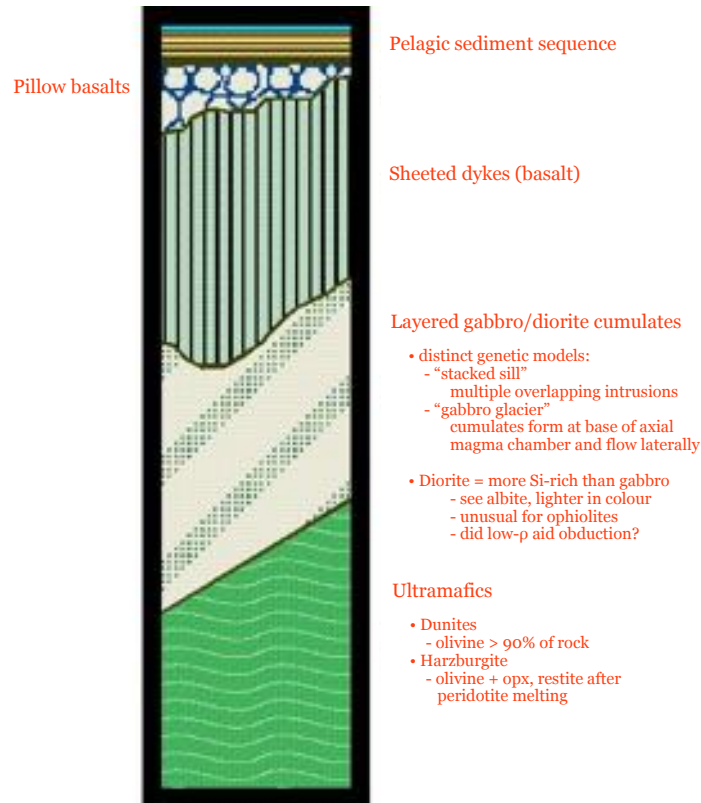


Fig. 5.4: Ophiolite Sequence.

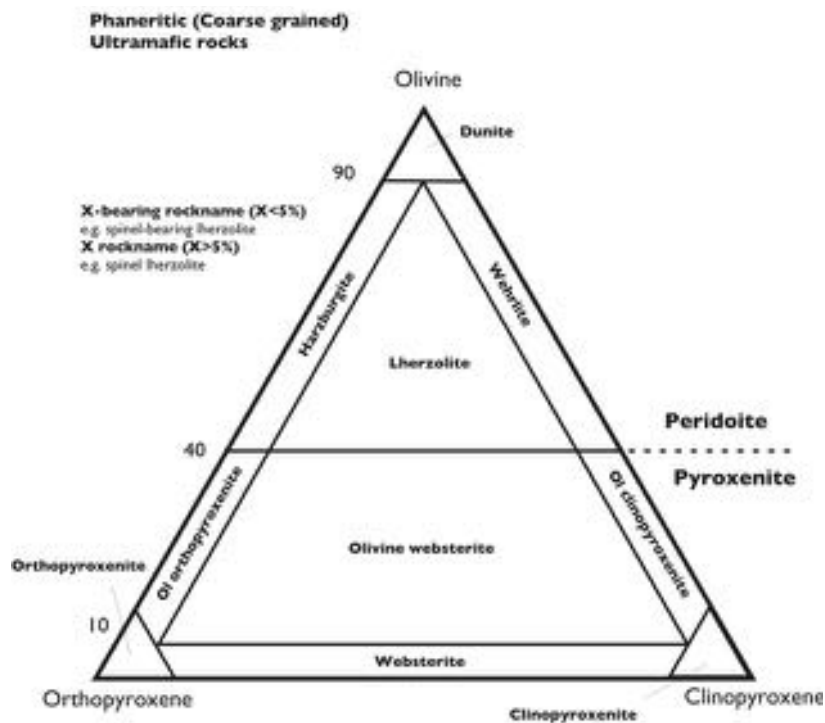


Fig. 5.5: Classification of ultramafic rocks. Image credit: J D Price, 2011.

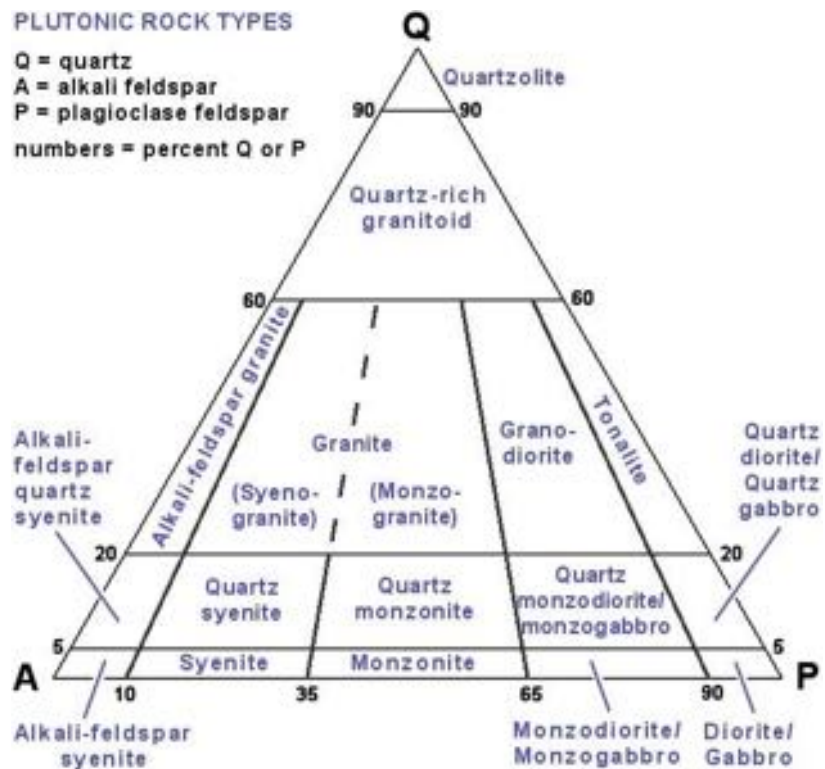


Fig. 5.6: Classification of plutonic igneous rocks.

10m up section from last stop, above the concrete foundation.

Initial observations:

Rocks are less hard and generally lighter. They contain small clasts, which are rounded and comprise non-interlocking crystals. Some quartz crystals are observed. The weathering of this outcrop is somewhat distinct from the previous stop, with more bulging rounded faces. Outcrop is heavily weathered and overgrown with lichen¹. Hard to obtain a fresh face.

Explanation:

The clastic nature of this rock indicates that it had a sedimentary protolith, but later metamorphism is evident from texture and the presence of some alteration minerals.

Summary:

Slightly metamorphosed volcanoclastic sediments at the top of an obducted oceanic crustal section.

Just next to parking spot on the way back from the last two stops.

Initial observations:

Very fine-grained, dark rock, which cleaves easily. Foliation evident in places, as well as suggestion of initial bedding. The colour of this mudstone is mostly dark, but much more reddish in some layers, presumably due to Fe content.

Explanation:

The absence of large clasts and homogeneity of fine grain size, as well as the colour, indicates that this rock is a mudstone/argillite. The strong foliation along which it cleaves is a product of metamorphism to a slate texture.

Summary:

Metamorphosed pelagic ocean sediments with unclear stratigraphic relationship to the volcanoclastics we saw last stop.

Stop 2: Bridges near Deception Pass

North side of bridges at Deception Pass. Phenomenal exposure in cliffs above road.

Initial observations:

Grey/green altered sedimentary rock with clear bedding features and quartz veins that are folded and boudinaged. Small faults cross-cut the cliff in multiple directions, with several good examples of slickensides particularly evident in the quartz veins (Figure 5.7). The bedding dips steeply ($\sim 40^\circ$) into the cliff face (East). Further up (N) the bedding pattern is clearer, with alternating sequences of pebbly conglomerates grading into (green/greyish) sandstones and thence to (darker) mudstones.

Explanation: The alternating fining-up sequences comprise a series of turbidites. There was some disagreement about the younging direction, which should in theory be in the direction of the fining. It is possible that the heavily faulted and folded nature of this outcrop resulted in different younging directions in different places. This outcrop included several fault zones with a thrusting sense (see field sketch), and the major fault structures dipped northwards, implying N-S convergence. Pervasive deformation is also indicated by the strongly folded bedding planes and boudinage of more competent vein material.

Summary:

Heavily deformed turbidite sequence, with some well-preserved brittle and ductile deformation structures.

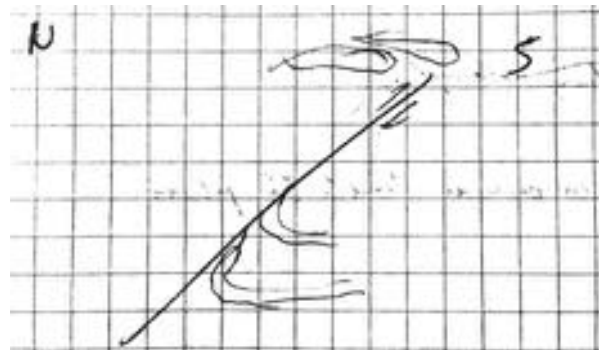
Other notes:

Excellent spot for lunch on Pass Island w/ remarkable views. Little shade from the sun.

¹Which, as we'll learn later, is a symbiotic amalgam of a fungus and an algae.



(a) Outcrop on NE side of road, N of bridges



(b) Carbonate veins.

Fig. 5.7: Field sketch of small fault (total height 40 cm) with displaced quartz veins.

Stop 3: Rosario Beach, Deception Pass State Park

North of Rosario Beach, on rocks along the coast.

Initial observations:

Clearly bedded rock with black/dark layers (2-10 cm thick) of fine-grained material alternating with harder, sugary, dark layers. Lots of small folds are evident, including isoclinal folds, as is boudinage of the harder material (Figure 5.8).

Explanation:

This rock comprises mud/silt stone layers, that are soft and weather preferentially, interbedded with harder cherty layers that weather proud. The deposition of cherts indicates seafloor deposition (of diatoms/radiolaria) on seafloor deeper than the CCD. The intense deformation into

beautiful structures indicates that this rock has been highly strained.

Summary:

Layered cherts and mudstones that have been heavily folded and lightly metamorphosed.

Other notes:

Fun and easy climbing and textbook small-scale folding structures.

**Fig. 5.8:** Banded cherts showing small-scale folding and boudinage.

30 m above last point, on top of the headland.

Initial observations:

Bumpy, black, fine-grained crystalline rock outcropping in scrubby grass. The “bumps” are between 30 and 60 cm in length. Some are broken open and appear to have radial fracture lines, with zoning of colour. Less than 20 m all around this outcrop we find more of the interbedded cherts/mudstones from the previous stop.

Explanation:

These are pillow basalts! They are fine grained because of the rapid cooling, and dark coloured because of their mafic composition. The colour zonation is likely due to differential weathering as a function of radius from the centre of the pillows that results from different cooling times and hence initial vesicularity etc.. The radial fractures are a result of tensional stresses introduced by rapid quenching with radial heat flow. Observations of the cliffs on the west face of the headland show that these pillow basalts cross-cut the sedimentary layers from the previous stop, indicating that the pillows have intruded (Figure 5.9).

Summary:

Pillow basalts from the top of the ophiolite sequence, intruded into the surrounding abyssal sediments.

Other notes:

Excellent view of the Bull Kelp bloom (Figure 5.10). These kelp die each year and re-grow during the summer at rates of 10” per day! They are rooted to the bottom and provide an important habitat for wildlife, including manatees, and breeding fish. The most recent day’s growth has a different appearance and is edible.



Fig. 5.9: Side of cliff, showing pillow basalts cross cutting the cherty layers.



Fig. 5.10: Kelp beds in channel below cliff.

Stop 4: Oso landslide

Initial observations:

We drove past the landslide deposit from the 22nd March 2014 land/mud-slide (one cannot stop due to ongoing construction). Currently the whole area is covered with construction crews, but one can see the incredibly long landslide runout, where all the trees and the town were demolished.

Explanation:

Forty-three people were killed as the SW flank of an unstable hill collapsed, resulting in a mud and debris flow running out for more than half a mile, covering the rural neighbourhood of Steelhead Haven. The suspected cause was soil saturation and weakening following heavy rainfall. There is a distinctive hummocky terrain to the runout deposit² due to coherent blocks within the flow.

Summary:

Destructive runout deposit of a recent, historic landslide (Figure 5.11).

Other notes:

The diminutive hill from which the landslide came belies the destruction wrought.



Fig. 5.11: Oso landslide provenance and deposit from car.

Stop 5: Stop on side of the road, 6 mi W of Darrington

Initial observations:

Looking up at the mountains to our north, we observed large scale structures at the crest of the ridge, and evident within the trees on the south slope. A stair-step morphology to the ridge crest indicated large-scale layering, dipping to the west. A change in the dip of the bedding was evident with apparently steeper dips in the ridge further west.

Explanation:

This large scale layering is found within a Mesozoic sedimentary section that comprises the accretionary wedge. The change in dip of the layers could be a result of a SW striking, NW-dipping thrust fault. Major SW-striking faults are expected in this region, related to continental margin convergence, but should be normal in sense. Either our “Swiss geology” from afar is inaccurate, or this might be a reactivated structure.

Summary:

Mesozoic accretionary sequence seen from miles away, on ridge line.

²Which we would later see echoed at volcanic landslides.

5.3. Day 3, August 5, 2014: Mt. Baker from afar

HANNAH RABINOWITZ

9:40 am	Departed campground
10:30 am	Stop 1: Mt. Baker Overlook on the way to Anderson-Watson Trail
11:45 am	Stop 2: Anderson-Watson Trailhead
12:45 pm	Lunch in an alpine meadow
3:20 pm	Stop 3: Upper Baker Lake Dam
4:20 pm	Stop 4: Boulder Creek
5:00 pm	Stop 5: Hot Springs
5:45 pm	Returned to Horseshoe Cove Campground

After a quick breakfast, we left the campground, driving south on some road. On the right hand side we observed lavas of the Sulfur Creek stage that are mostly covered by trees. We drove by the Upper Baker Lake Dam, a hydroelectric plant. The dam walls expose layers of metasedimentary rocks. As we drove up the mountain, a brave little quail ran in front of the car, bringing the caravan to a halt. Jonathan had to run out of the car to encourage the quail to leave the road.

Stop 1: Mt. Baker Overlook

We stopped on a mountain road to discuss the geology and glaciology of the Mt. Baker area and how Mt. Baker (to the NW, Figure 5.12) fits into the context of the Cascade Range. The lithology present at the overlook is primarily phyllite, which can be seen from the micaceous sheen as well as the cleavage.

Looking down into the valley, one can see Anderson Creek. The bedrock here is primarily Cretaceous Shuksan Greenschist, which continues to Mt. Shuksan to the North. The Shuksan Greenschist is bounded to the East by the Stray Creek dextral strike-slip fault. This fault is one of a series of faults that are responsible for smearing old terrains in the Western United States hundreds of kilometers northward as a result of partitioning due to oblique subduction in this region (see the Geologic History of the Pacific Northwest section of this guide). Underlying Mt. Shuksan is the older Jurassic Nooksack Formation composed of sandstones and argillites.

On Mt. Shuksan, two large glaciers (Sulfide Glacier and Crystal Glacier) are visible. White Salmon Glacier is further to the West. From this viewpoint, one can clearly see Mt. Baker's Park Glacier across the valley, which exhibits a clearly visible ablation zone where blue ice is exposed where the overlying snowpack has melted. This blue ice is the result of the metamorphism of ice at the bottom of the glacier. Because the blue ice is darker than the white snow, it absorbs more radiation than the overlying snow. This (as well as the even darker rock fall deposits) account for some of the variability in melting in different parts of the glaciers.

Now, in preparation for our upcoming visits to Mts. Ranier and St. Helens, we paused for a quick overview of the Cascade Range. The northern extent of the Cascade Range is composed of the Garibaldi Volcanic Belt, which consists of three volcanoes in Canada and Mt. Baker and Glacier Peak in the United States. The northern volcanoes have less output than the more southern components of the chain and Mt. Baker is northernmost volcano that appears to have significant output. Volcanoes further south in the Cascade Range generally have larger output (or better preservation of erupted material?) than those further to the north. In the Mt. Baker area, this



Fig. 5.12: Mt. Baker from the overlook.

effect is reflected by the paucity of cindercones that contribute to volcanic output. In addition to the marked change in output represented by Mt. Baker, the volcano is also unique in that it is the most mafic of the volcanoes in the Garibaldi Volcanic Belt suggesting a more open pathway which allows magma to travel to the surface more quickly.

Mt. Baker's edifice is about 20 ka and has been growing for the last 40,000 years. The most recent eruption at Mt. Baker was ~5,900 years ago. Some crags on the volcano (the Black Buttes) are slightly offset to the SW suggesting older episodes of volcanism and have been dated to ~0.5 Ma. Further to the east is evidence for more destructive caldera-style episodes (~1 Ma). This is marked by ignimbrites flowing into the caldera and filling in the Kulshan Caldera depression created by the eruption.

Stop 2: Anderson-Watson Trail

We went for a hike further up the road from Stop 1. The Anderson-Watson Trail is highly recommended for anyone who is interested in a ~2 hour roundtrip hike (albeit with ~ ±500 ft elevation change) culminating in an idyllic view of Mt. Baker. Along the trail, we found various volcanic and metasedimentary rocks including some metamorphosed rocks with well formed augen, which offer a nice opportunity to practice interpreting strain markers. We stopped for lunch in an alpine meadow surrounded by flowers with a beautiful view of Mt. Baker (Figure 5.13).

Stop 3: Upper Baker Lake Dam

Here, we saw metamorphosed mudstone (slate or phyllite) of the Nooksack Formation with S-striking quartz veins and faults (180/57 W) with foliation dipping to the north (253/56 N)³. The outcrop exhibits good foliation and early mica development. Walking over the bridge over the dam, we discussed hazard preparedness in association with volcanic activity at Mt. Baker. In 1975, Mt. Baker started emitting elevated levels of SO₂. In response to this increased activity, officials began improving volcanic monitoring instrumentation in the area (for example, installing a seismic network to monitor volcanic tremor) and planning for hazard response in the event of an eruption. They realized that, in the event of a likely eruption, dam levels should be lowered to reduce the risk from lahars and pyroclastic flows, which would follow river channels away from the volcano. Though the 1975 Mt. Baker eruption never happened, the increased awareness that followed in the wake of the volcanic activity proved to be important 5 years later when Mt. St. Helens erupted in 1980. Richard, a hot springs soaker from Hamilton, confirmed that flooding hazards associated with the dam are a constant concern and that major flooding affects locals every few years.

³Here we use the notation (strike/dip dip-direction).



Fig. 5.13: Lunch stop on the Anderson-Watson trail.



(a) Oxidized rocks at Boulder Creek



(b) Tree trunk preserved in a cold lahar deposit at Boulder Creek.

Fig. 5.14: Observations at Boulder Creek.

Stop 4: Boulder Creek

A small trail to the side of the bridge here leads to a streambed. The boulders making up the streambed are primarily black and red in color. Both are basaltic in composition, the red color deriving from the *in situ* oxidation of the volcanic debris (Figure 5.14) where the reddish surficial deposit was associated with contact with the stream water. Walking along this streambed, we reached an outcrop of lahar deposits from an 1845 cold lahar (a lahar not associated with a volcanic eruption). These deposits are poorly sorted. One notable feature of these lahar deposits is a large tree trunk lying within the deposit (Figure 5.14) that allows precise dating of the flow.

Stop 5: Hot Springs

After our stop at Boulder Creek, we drove to a nearby out-of-the-way hot spring. Driving N on Baker Lake Rd from NF 1112 (the road leading to Baker Lake Dam), we drove over a bridge (the one over Boulder Creek). After this stop, we continued along Baker Lake Rd for <100 m before turning left onto NF 1130. We continued on NF 1130 for about a mile before it forked. We took the right fork (NF 1144). After a sharp turn, this road leads to the parking lot for the hot springs. To get to the hot springs, we walked along a trail initiating from the west side of the parking lot. After about an hour soaking in the hot springs, we headed back to camp. Note: clothes changing facilities are not provided!

5.4. Day 4, August 6, 2014: North Cascades National Park

CELIA EDDY

8:30 am	Discussion at the car before leaving campsite
8:45 am:	Depart Horseshoe Cove Campground
10:15 am	Stop 1: Newhalem
10:40 am	Stop 2: Gorge Creek Outlook
11:15 am	Stop 3: Outcrop at Mile 124.5 on Route 20
11:30 am	Stop 4: Outcrop at Mile 125.2 on Route 20
12:00 pm	Stop 5: Diablo Lake Overlook, lunch
1:00 pm	Stop 6: John Pierce Falls
1:45 pm	Stop 7: View over Ross Lake
2:30 pm	Stop 8: Washington Pass Overlook
3:15 pm	Stop 9: Outcrop at Mile 167.6 on Route 20
5:40 pm	Arrive at Daroga State Park Campground and have dinner

Leaving Horseshoe Cove Campground, we drove south on Baker Lake Road and then southeast on Burpee Hill Road towards Concrete where we turned east onto Route 20 (North Cascades Highway). We drove through the Sulphur Creek Lava Flow, a subaerial lava flow from Mt. Baker erupted approximately 8000-9000 years ago. We also drove through parts of the Nooksack Formation, Jurassic sedimentary rocks that form the basement of Mt. Baker. Driving up Burpee Hill, we passed through pyroclastic flow deposits from Mt. Baker.

Between Concrete and Marblemount, we saw landslides and fluvial deposits on the north side of the road. At Marblemount, we made a sharp left turn on Route 20 to follow the Straight Creek Fault. This fault separates Mesozoic metasediments to the west and the 220 Ma Marblemount meta-quartz diorite to the east. The quartz diorite is a muscovite-chlorite-epidote-albite-quartz rock that contains small amounts of biotite and hornblende. This and equivalent plutonic formations extend southeastward from the Straight Creek Fault for ~150 km before disappearing beneath Miocene Columbia River Basalts. After entering North Cascades National Park, we observed outcrops of Nappequa Schist around miles 112-113 on Route 20. Between miles 115-116 we saw outcrops of Oligocene granodiorite, exhibiting a rounded weathering pattern. We continued driving east into the Skagit Gneiss Complex, which is ~60-70 Ma. The first 7 stops of the day are all within this complex.

Stop 1: Newhalem

The outcrop is on the left when you enter Newhalem, just after the visitors' center. The Newhalem orthogneiss is a ~75-60 Ma biotite gneiss, containing a complicated network of quartz veins and fractures (Figure 5.15). The wavy quartz veins are migmatite, indicating that the rock started to melt on a large scale. The straighter pegmatite dikes are evidence of a later hydrothermal overprint. On a smaller scale, biotite is drawn out into concentrated layers. This gneiss is in the lower to middle part of the crustal section.

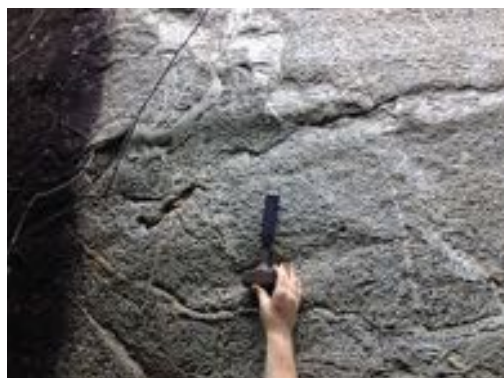


Fig. 5.15: Migmatite quartz veins in the Newhalem orthogneiss.

Stop 2: Gorge Creek Outlook

The outcrops are a short walk from the parking lot. The Skagit orthogneiss is more strongly foliated than the previous outcrop, indicating more deformation relative to the New Halen orthogneiss. There is little migmatization, but evidence is present of both brittle and ductile deformation; there are large fault surfaces with slickensides (Figure 5.16) as well as smaller-scale folds. Large radial blast fractures in the outcrop have an obvious anthropogenic explanation. After examining the outcrops at the overlook, cross the road and walk out onto the bridge. There is a nice view of a tall, narrow waterfall.

Stop 3: Outcrop at Mile 124.5 on Route 20

This outcrop is still within the Skagit gneiss complex. It is strongly banded, with mica dominating the darker layers. The lighter layers contain large clasts of augen. There are ‘sigma’ shear markers indicating dextral shear (Figure 5.17). There are many small garnets within the dark layers. This is a porphyroclastic augen gneiss that has undergone multiple phases of shear deformation.



Fig. 5.16: Slickensides on a fault surface.



Fig. 5.17: Shear markers in augen gneiss.

Stop 4: Outcrop at Mile 125.2 on Route 20

This gneiss outcrop contains significantly more garnets than the previous orthogneiss, indicating both higher-pressure conditions and a different, more aluminum-rich, source rock. This is a ~70-68 Ma metapelite, with a shale protolith (Figure 5.18).



Fig. 5.18: Garnet-rich metapelite

Stop 5: Diablo Lake Overlook

We ate lunch overlooking Diablo Lake until approximately 12:40. Then we walked to the outcrop directly across the road from the overlook. The outcrop contains many intersecting dikes indicating a large melt network (Figure 5.19). These are quartzo-feldspathic pegmatites within the gneiss that date to 53 Ma. The gneiss itself is approximately 61 Ma, but there are older zircons within the gneiss that date to 2.6 Ga, demonstrating recycling of the crust. This gneiss is not strongly banded and is somewhat faulted.

Stop 6: John Pierce Falls

This gneiss outcrop is on the side of the road. It is very strongly banded and contains large amounts of mica. There are many small-scale folds. Pegmatite bodies dating to 54-52.5 Ma are pervasive,



(a) View over Diablo Lake.



(b) Pegmatites in gneiss.

Fig. 5.19: Diablo Lake.

though they are not as large as at the previous stop. Lenses of leucosome, very light-colored rock, have formed within the bands. A large dike has intruded into the gneiss; there is a clear contact on either side of the dike between the fine-grained dike and the coarser-grained gneiss. The dike itself is granitic to granodioritic and it is slightly foliated, particularly on the sides, as a result of shearing as it intruded the gneiss. On either side of the dike, the density of pegmatites is high and decreases with distance from the intruded rock. There are also smaller dikes present (Figure 5.20). This meta-greywacke outcrop presents evidence for large-scale melt production.



(a) Small fold.



(b) Dike intruded into gneiss.

Fig. 5.20: Gneiss outcrop.

Stop 7: View over Ross Lake

Last stop heading out of the Skagit Gneiss Complex, with a nice view over Ross Lake (Figure 5.21). The Ross Lake Fault marks the end of the complex. The complex is bounded on the other side by the Entiat Fault. After this stop, we began driving through the Golden Horn Batholith, which is a 49 Ma granitic pluton that is not genetically related to the Skagit Gneiss Complex. Passing into the more granitic rocks, we noted that the weathering patterns changed. With increasing amounts of K-feldspar, the color of the weathered rocks becomes more peachy-beige as the rocks weather to clay. The drainages have a beige color that is typical of granite weathering.



(a) View over Ross Lake.



(b) Cars parked at viewpoint.

Fig. 5.21: Ross lake.

Stop 8: Washington Pass Overlook

A short walk from the parking lot is an overlook in the middle of the Golden Horn Batholith. One can see Liberty Bell to the right and the Early Winter Spires just to the left of Liberty Bell, while Kangaroo Ridge is directly ahead, behind a glacially carved valley (Figure 5.22). Decompression fractures provide evidence for how the pluton has been unroofed (Figure 5.23). We also saw strange trees that grow in spirals in both directions, but primarily clockwise. One hypothesis for this is strong unidirectional wind leading the trees to grow that way, but we are not sure.

Note that this is also a nice spot for lunch, if you leave earlier in the morning or spend less time at the previous stops.

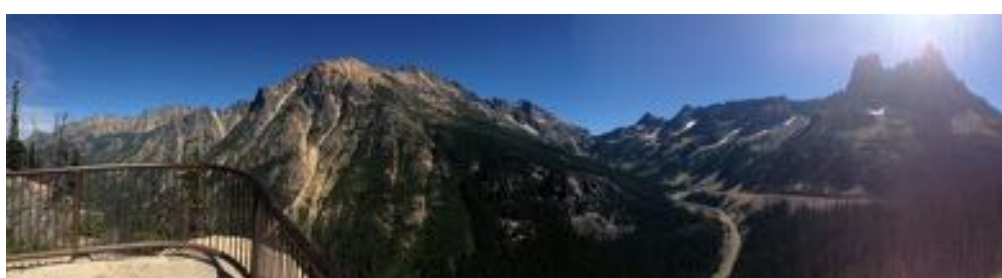


Fig. 5.22: View from Washington Pass Overlook



(a) Spiral trees.



(b) Decompression fractures.

Fig. 5.23: Washington Pass.**Stop 9: Outcrop at Mile 167.6 on Route 20**

This outcrop by the side of the road is a light-colored granite, containing a large amount of K-feldspar. This granite evinces a rapakivi texture, with the pink feldspar crystals inside white plagioclase crystals (Figure 5.24). There are also some fine-grained mafic enclaves with amphiboles in plagioclase. At this stop, we also contrasted the granite to samples that Philipp collected at several outcrops along the road. We compared samples of tonalite, granodiorite, and granite. The fraction of K-feldspar is greater in the more granitic samples, while the granodiorite is dominated by quartz and the tonalite has only a very small fraction of K-feldspar. This indicates increasing fractionation of the melt grading from tonalite to granite. The granite represents the shallow crust, while granodiorite and tonalite represent the shallow-to-mid-level crust.

**Fig. 5.24:** Rapakivi texture in granite

increasing fractionation of the melt grading from tonalite to granite. The granite represents the shallow crust, while granodiorite and tonalite represent the shallow-to-mid-level crust.

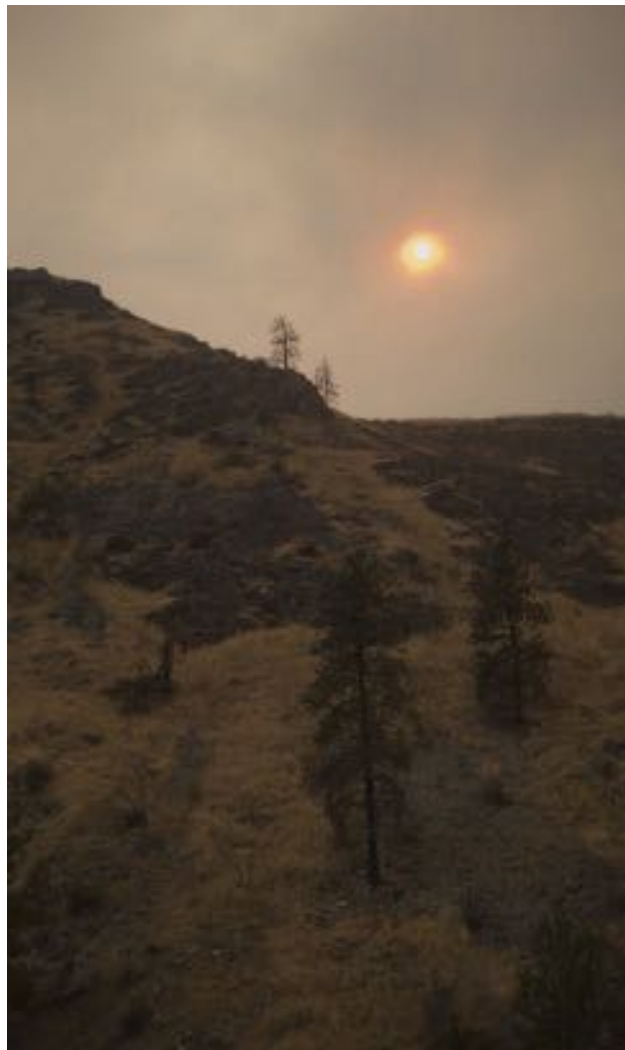


Fig. 5.25: View of the sun driving through Chelan county. Smoke visible from nearby fires.

Our final drive to the campsite took us through Chelan and Okanogan Counties, which were affected by the devastating Carlton Complex wild fires. It was the largest fire in Washington State history (source: wikipedia). The fire was still ongoing as we passed through the area, and smoke was visible.

5.5. Day 5, August 7, 2014: Columbia River Basalt and Petrified Forest

JONATHAN GALE

9:00 am	Departed campsite
10:30 am	Stop 1: Vantage Road
11:05 am	Stop 2: Viewpoint Overlooking Columbia River
11:20 am	Stop 3: Palagonite and Pillow Basalt along HWY 26
11:40 am	Stop 4: Gingko Petrified Forest
12:30 pm	Stopped for supplies in Ellensburg and lunch
1:30 pm	Departed for Mt. Rainier via southern route toward Yakima
5:00 pm	Arrived at Silver Springs campground

Today we went the furthest east on the trip, saw both desert and snow, extrusive and intrusive rocks.

Our day began at Daroga St Park campground on the Columbia River. It concluded at Silver Springs Campground on the outskirts of Mt Rainier National Park. From Daroga, we drove along US 97 to SR 28 to Quincy, WA and south on SR 281. We looked across the Columbia River for the Entiat Thrust and amphibolites. Once we turned away from the river, roadside exposures of Columbia River Basalt and related sedimentary sequences were visible where the road dipped below the otherwise-flat terrain. The first such exposure could be seen near Sutton Salvage. Mile 20 on SR 28 has a good view of the valley. From SR 281, we turned onto I-90 W and exited at Silica Rd SW, then turned left on Vantage Rd SW.



Fig. 5.26: Columnar Jointed Columbia River Basalt

Stop 1: Vantage Road

Natalia gave an overview of Columbia River Basalt volcanism. Over 300 mid-Miocene flows occurred 100s to 1000s of years apart covering over 200 mi. Individual flows are distinguishable from their vesicular tops and columnar joints, which result from top-down cooling. We discussed the connection of this volcanic episode with the Snake River Plain and Yellowstone, as both are subsequent expressions of the same hot spot. Orange-colored weathered material is called palagonite. It is present in all of the basalt outcrops viewed over the course of the day. We discussed the study of Columbia River Basalt reactivity as it relates to carbon sequestration and aquifer management.

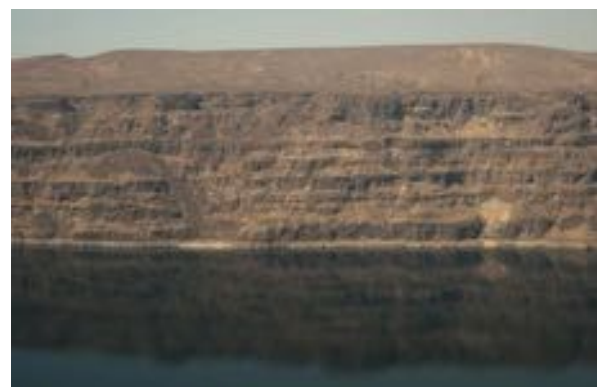


Fig. 5.27: Layers of Columbia River Basalt flows show the internal structure created by cooling from above.

From Stop 1, we returned to I-90 W and exited at a designated scenic viewpoint with the bridge to Vantage, WA visible in the distance.



(a) The Columbia River across from Vantage with I-90 Bridge.



(b) Layered Basaltic Flows Demonstrating the Multiple Eruption and Cooling Histories.

Fig. 5.28: The Columbia River.

Stop 2: Viewpoint Overlooking Columbia River

A great view of a series of flows can be seen across the river from this viewpoint. The columnar joints and vesicular tops make distinguishing the different flows easy in an outcrop like this.

From this stop we returned to I-90 until just before the bridge to Vantage over the Columbia River where we exited onto HWY 26 and followed it past 243 to where it makes a left turn.

Stop 3: Palagonite and Pillow Basalt along HWY 26

CAUTION: THIS STOP IS A DANGEROUS ROADSIDE STOP WITH LITTLE ROOM FOR MULTIPLE VEHICLES TO PULL OVER AND TRUCKS COMING AROUND A BLIND TURN. This stop has distinct pillow basalts interspersed between palagonitic material. Some pillows have internal structure reflective of their cooling history. Others have 3 dimensional structure visible.

From Stop 3, we returned to I-90 W into Vantage and followed signs to Gingko Petrified Forest St Park.

Stop 4: Gingko Petrified Forest

We examined the woods of the petrified logs in the area north of the visitors' center. Silica replacement has altered many of the logs while maintaining their overall forms and structures. The logs were preserved in part by the rapid burial of material by the basalt flows. They have subsequently been uncovered and put on display.



Fig. 5.29: Palagonite and Pillow Basalts



Fig. 5.30: Petrified Gingko Forest Wood

We continued on to Ellensburg and from there we drove south on I-82 to Yakima and continued west on US 12. Along US 12, 123 and 410 we followed legs F then E from the Roadside Geology of Mount Rainier National Park and Vicinity produced by the Washington State Department of Natural Resources. Due to time constraints, we made no dedicated stops prescribed by the guide, but communicated the passing features via 2-way radio. We ended at Silver Springs, exiting Mt Rainier National Park along 410 and stayed in the surrounding Snoqualmie National Forest.

5.6. Day 6, August 8, 2014: Hiking Burroughs Mountain at Mt. Rainier National Park

YANG ZHA

8:40 am	Departed campsite
9:05 am	Stop 1: Ice contact lava columns. Road side between White River Campground and Sunrise.
10:30 am	Stop 2: Parking lot at Sunrise
11:00 am	Starting hiking
11:30 am	Stop 3: Little ice age moraine of Emmons glaciers
12:30 pm	Stop 4: On top of 2nd Burroughs Mtn
1:00 pm	Lunch
1:30 pm	Stop 5: Pumice of the C tephra
1:50 pm	Stop 6: Igneous inclusion in andesite
2:15 pm	Stop 7: Back into granodiorite basement
3:30 pm	Stop 8: Old mine at Glacial Basin
4:30 pm	Back to White River Campground and drove back to campground
5:30 pm	Returned to Silver Springs Campground

This day was dedicated to a 6 hour hiking on to the Burroughs Mountain at the northeastern side of Mt. Rainier National Park (Figure 5.37). Total hiking distance ~9 mi. The trail starts with a elevation climb from 6400 ft at Sunrise to 7400 ft at top of 2nd Burroughs Mtn (3.2 mi), followed by a descent to 4232 ft at White River Campground (6 mi). We were joined by USGS scientist Tom Sisson, who presented a thorough and informative overview of volcanism at Mt. Rainier.

We left the campsite and drove to White River Campground (the end of the trail, elevation 4232 ft). We parked one car here in order to shuttle drivers to the upper parking lot at Sunrise after the hike.

Stop 1: Roadside of Sunrise Park Rd between White River Campground and Sunrise

On the downhill side of the road we saw andesitic lava flows from the modern Mt. Rainier (< 500 ka). Tom pointed out that large volume lava flows are mostly found on ridge crests instead of valley floors. This is intriguing because lava flows should gravitationally fill the (lower) valley floors. One explanation was that the valley-filling lava had been eroded away. But, given the young age (~40 ka) of these lavas, there has not been enough time to erode away hundreds of meters of rocks. So this model was rejected.



Fig. 5.31: Lava cooling feature at Stop 1

These ridge-forming lava flows have narrow, glassy columns pointing perpendicular to the ridge slope (Figure 5.31). These are cooling features resulting from lava being chilled against glacier ice. The direction of columns corresponds to direction of maximum cooling, indicating that lava was cooled from below and from the side. In the valleys where ice was thick, lava flows were cooled rapidly, resulting in impediments to downhill flow. On the ridges, where ice was thin, lava melted away the ice and advanced further. After the glaciers retreated following the last glacial maximum, the lava flows are left on the ridges. The fact that these ice contact features are ubiquitous and one rarely sees valley floor lava suggest that these valleys were covered with thick ice during nearly all of Pleistocene. The top of these lava flows can, therefore, be used to infer ice thickness at the time of the eruption.

We also saw some coarse-grained inclusions within the andesitic lava. These are porous, and are compositionally more mafic than the lava (according to Tom). These inclusions have been dated to be around the same age of the erupted lava. This suggests that these are genetically related to the lava (although slightly older), possibly included during some magma mingling activity.

Stop 2: parking lot at Sunrise (elevation 6400 ft)

As we were getting ready for the long hike, Tom gave us a preparatory overview of Mt Rainier (Figure 5.32). There are two summit craters at Rainier: East Crater, which is taller and younger (pictured in Figure 5.32), and West Crater. Both craters have steam vents with temperature measured to be up to 100°C. There is a subglacial crater lake inside East Crater. Below the summit we saw Emmons glacier to the left (east) and Winthrop glacier to the right (north). Toward the volcano in the intermediate foreground is Steamboat Prow, which consists of coarse fragmental deposit.



Fig. 5.32: View of Rainier summit from Sunrise

We started hiking from Sunrise parking lot towards Burroughs Mountain, which erupted sometime within the period 480,000-490,000 years ago. This was the earliest large-volume lava flow following the onset of the modern Mt. Rainier edifice.

Stop 3: Little ice age moraine of Emmons glacier

As we hiked up the mountain, we got a better view of the Emmons glacier valley. To the north side of the valley (right side in the picture) we saw a sharp scarp along the valley. Outside the scarp there are developed forest, but inside the scarp there are no trees on the slope and very small trees in the valley. This turned out to be the limit of the glacier during the little ice age; at the peak of little ice age the valley was covered by ice up to the tree line. Coring of trees date the cessation of the little ice age to ~1850. Mike pointed out the terminus of the Emmons glacier (Figure 5.33). It is at the base of a dirty, seemingly rocky slope where a subglacial stream flows out.

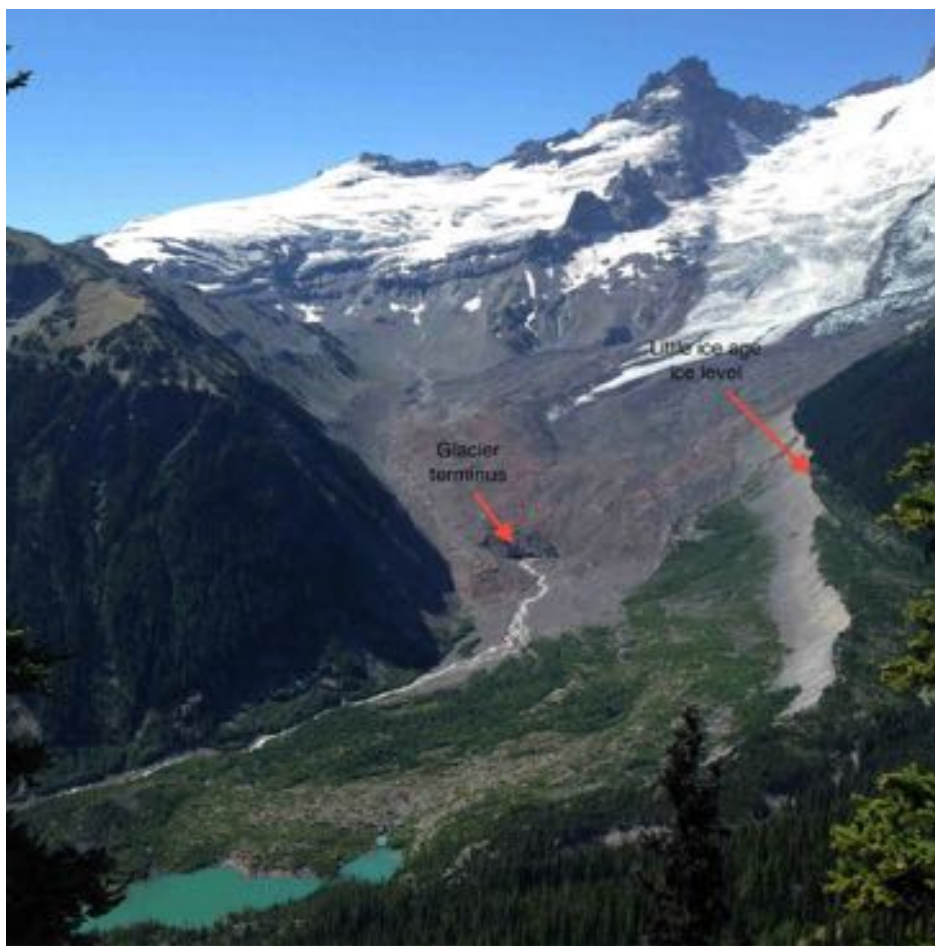


Fig. 5.33: Emmons glacier and little ice age tree line.

Stop 4: On top of 2nd Burroughs Mountain (elevation 7400 ft)

After we hiked to the top of the 2nd Burroghs Mtn, we took a closer look at Steamboat Prow. Steamboat Prow consists of coarse fragmented deposit that stratigraphically underlies the Burrows Mtn lava flow. The fragmental deposit dips away from the present summit by as much as 20 degrees, suggesting that a high edifice existed early in the growth of modern Rainier. This means that modern Rainier either was built on a tall ancestral Rainier or grew very fast.

Paleomagnetic measurements on the deposited clasts show that those near the top of Steamboat Prow have uniform magnetic orientations (i.e. were deposited hot), and those at lower elevation have random magnetic orientations (i.e. were deposited cold). The explanation is that the initially hot pyroclastic flow entrained glacial deposit on the way down, which lowered its temperature and transformed it into a lahar.

Stop 5: Pumice of the C tephra

After deciding not to climb up to the 3rd Burroghs Mtn, we began descending down to the Glacier Basin Trail. Near the beginning of the descent we stopped to look at the pumice from the C tephra deposit. This is from a 2200 ybp eruption, the most voluminous of the Holocene ($\sim 0.1 \text{ km}^3$). This is a compositionally diverse eruption. Most of the deposit is brown-ish andesite, but this contains light-colored dacite streaks: a possible result of magma mingling (Figure 5.34). There are also grey-ish vesicular andesites. Geochemical analysis showed that both are very high in Sr, similar to the Sr concentration of a 2500 ybp eruption. The interpretation is that these dacite streaks and vesicular andesites are residues, left over in the shallow magmatic system after the 2500 ybp eruption, and they were mixed with the 2200 ybp magma and flushed out of the system.



Fig. 5.34: Vesicular andesite (left) and regular andesite with white dacite blebs (right) at C tephra

Stop 6: Igneous inclusion in andesite

As we continued down the trail, near the base of the lava flow, we again saw some fine-grained andesitic enclaves that are reportedly geochemically more evolved than the surrounding andesite (Figure 5.35). They are interpreted to result from magma mingling activity.



Fig. 5.35: Plutonic inclusions in andesitic lava

Stop 7: Back into granodiorite basement

A short distance downhill from the last stop (about 100 m elevation drop), we crossed a distinct lithologic boundary between the younger andesitic lava and older, crystalline granodiorite basement.

We continued down the Burroghs Mtn Trail to the junction with the Glacial Basin Trail. The team split into two groups. One continued up and right (SW) to Glacier Basin Trail (1.5 mi round trip), the other headed back directly (E) to the White River Campground parking lot (2.4 mi from the junction).

Stop 8: Old mine at Glacier Basin



Fig. 5.36: Glacial basin

We hiked up the Glacier Basin Trail. At the end of the trail there is a nice view of the Emmons Glacier (Figure 5.36). An old mine used to operate here, drilling into the basement granodiorite for useful minerals (e.g. sulphite). We also saw some vertical radial dikes in the lava flow.

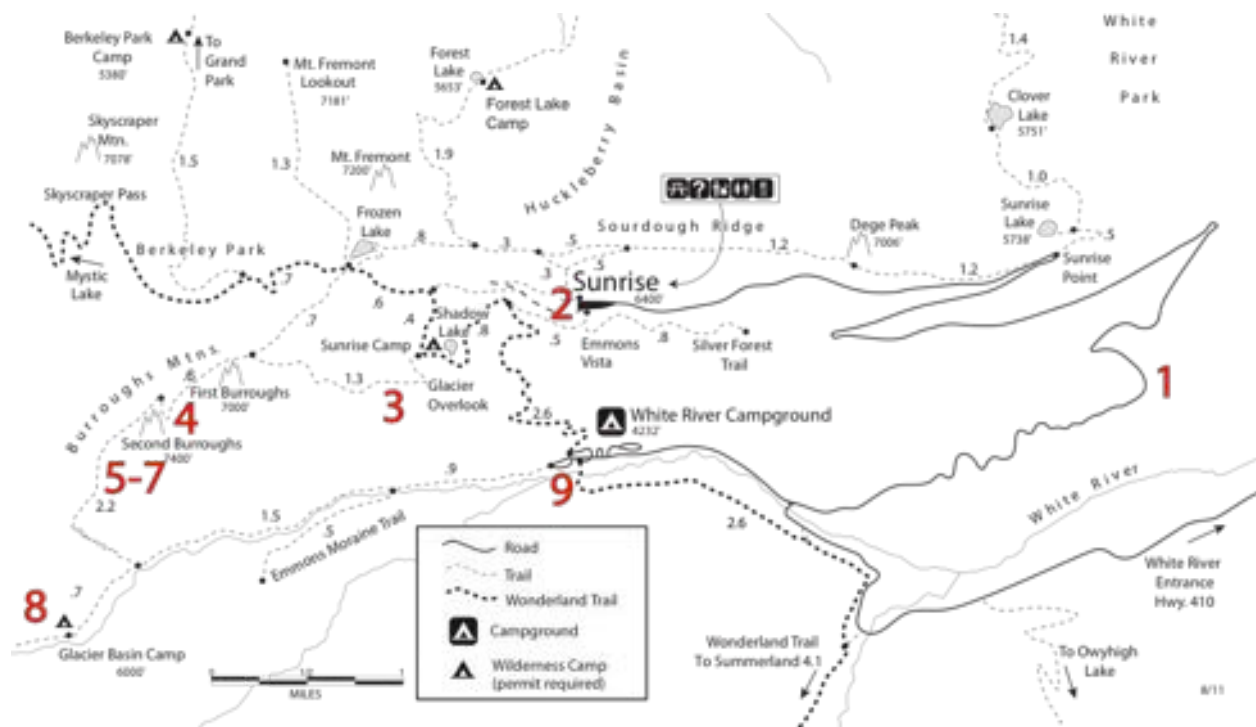


Fig. 5.37: Trail map and approximate location of each stop

5.7. Day 7, August 9, 2014: Hiking on south side of Mt. Rainier

MIKE WOLOVICK

7:45 am	Depart campsite
8:50 am	Stop 1: Arrive at Paradise Visitors Center
10:20 am	Begin hike towards Parorama Point
12:30 pm	Stop 2: Lunch spot
1:30 pm	Stop 3: Glacier Vista
2:00 pm	Stop 4: Moraine Trail
3:30 pm	Leave Paradise
5:30 pm	Arrive at Iron Creek Campground

Left camp without breakfast to beat crowds (we went on a Saturday). Saw plutons from the Tatoosh Range (14 ma) on the drive. When we arrived at Paradise visitors' center we found the parking lot already PACKED with people. We purchased breakfast at the Paradise Inn (Figure 5.38a) and prepared lunches for the hike.

Stop 1: Paradise

Began hike on trail towards Panorama Point. Early stages of the trail are paved and crowded. This trail is on the south side of Ranier, whereas yesterday's Burrough Mountain hike was on the northeast side. There are more (and larger) glaciers on the north side of the mountain because it faces away from the sun. In the andesite along the train, we observed lighter-colored lenses containing plagioclase phenocrysts (Figure 5.38b). Flow banding is also visible.

St. Helens is visible in the distance to the south (Figure 5.38c). We can see the north face of it, including the amphitheater and new dome. Mt Adams is also visible in the distance.

Phillip's musings: it's difficult to come up with a universal theory of eruption styles. The processes are too complex. My private thoughts: multi-phase flow is hard, man. So many different timescales are relevant. I feel your pain.

Stop 2: Panorama Point

This was a scenic spot for lunch, with good views and space for groups to eat (Figure 5.38d).

Pyroclastics visible on trail up to Glacier Vista, in between what look like andesite flows. Andesite breaks in slaty pieces because of conjugate fracture pattern. The group split up after lunch. The self-styled 'exploration group' (Johnathan, Zach, Jingle, Yang, and Mike) climbed two more minor peaks to obtain a fantastic view of the upper part of Nisqually glacier, before meeting up with the main group again at Glacier Vista.

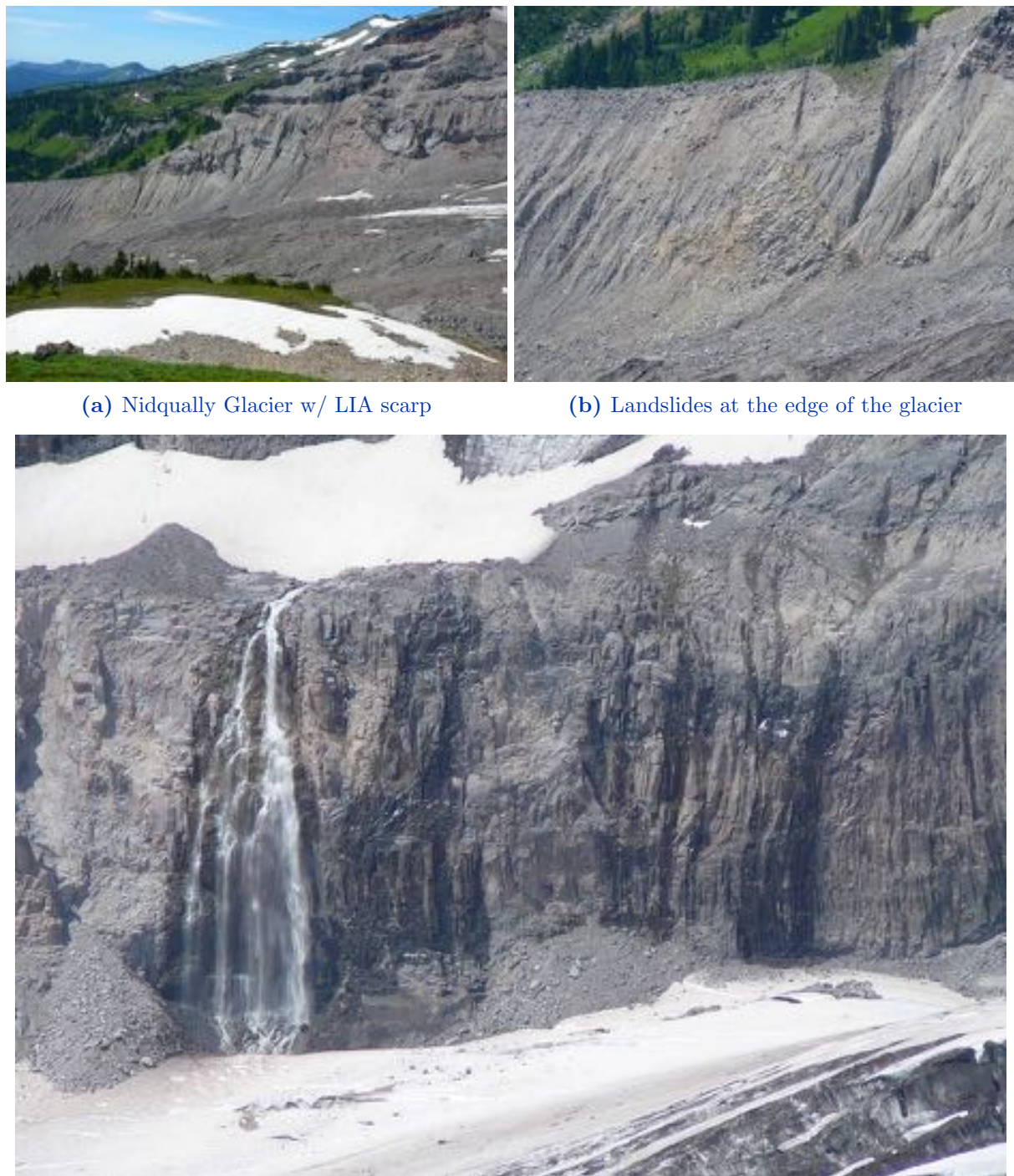
Stop 3: Glacier Vista

At Glacier Vista, Nisqually Glacier is visible in the valley (Figure 5.39a). The little Ice Age scarp and lateral moraine are visible on the opposite valley wall (Figure 5.39a). The glacier toe is covered in debris (Figure 5.39a). There is a contact visible in rocks exposed below the LIA scarp on the opposite valley wall. We speculated about coherent landslide blocks or exposed basement (Figure 5.39b). A waterfall emerging from beneath a small hanging glacier higher on the mountain

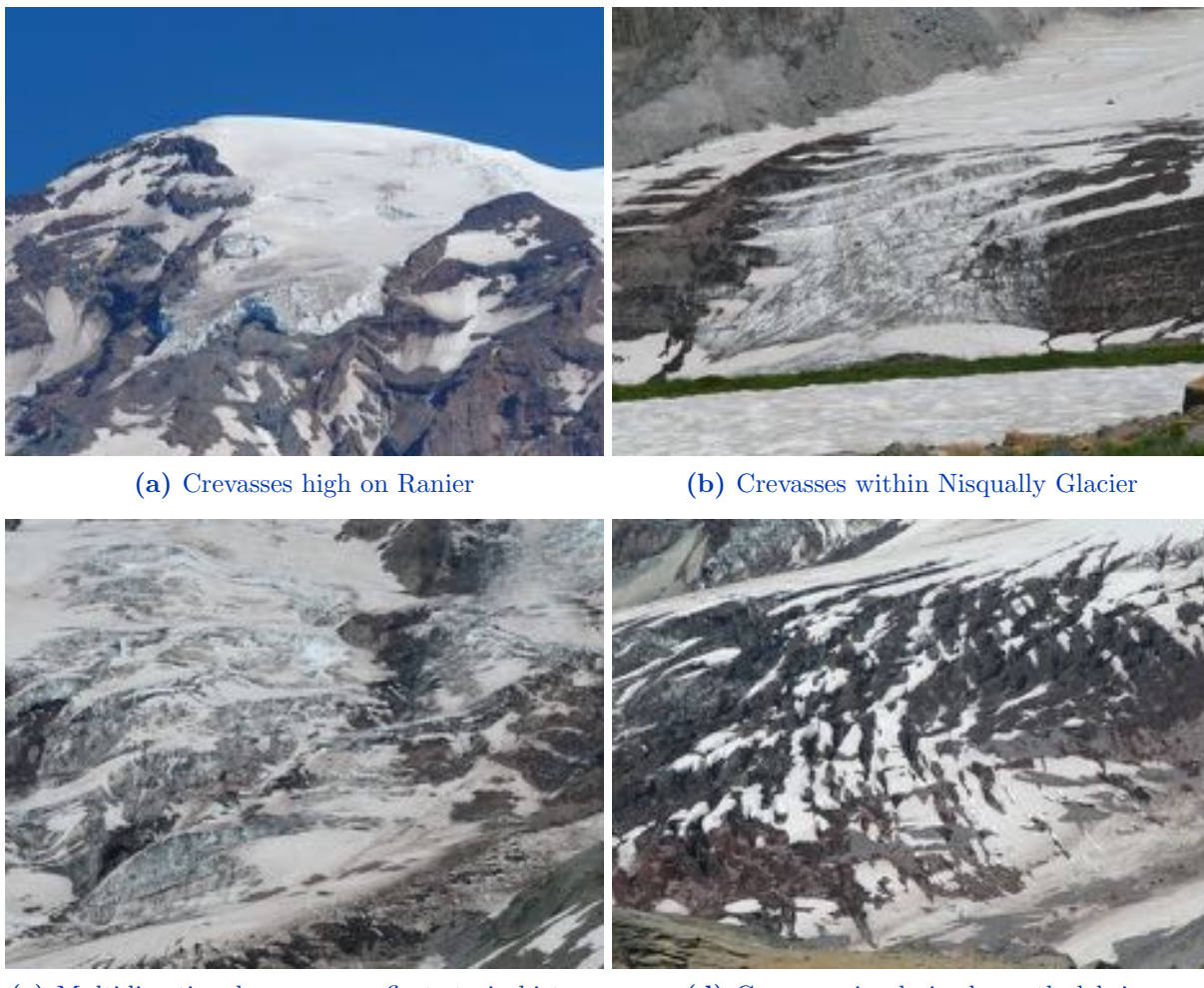
Fig. 5.38: Views on Paradise Hike, Mt. Rainier

can be observed entering the subglacial hydrology system beneath Nisqually Glacier (Figure 5.39c).

The deformation structures in the glacier reflect the overall strain rate regime that is expected for a mountain glacier. Above the equilibrium line altitude (ELA), in the accumulation zone, the glacier experiences extension and thinning to compensate for a positive surface mass balance. Subsidence caused by extension is (roughly) in balance with snowfall on the surface. Ice flux increases from the mountain peak towards the ELA, reflecting the increasing volume of snowfall that must be removed by ice flow. The extension is manifested in brittle failure features visible at the glacier surface, including crevasses and scarps (Figures 5.40a and 5.40b). Crevasses are tensile cracks that form when the ice experiences extension or shear (shear stress can be decomposed into compression and tension along the principal axes). Once they are formed, crevasses are simultaneously advected downstream and deformed by ice flow, resulting in a highly complex pattern of multiple crevasse orientations overprinted on each other in the main glacier trunk (Figure 5.40c). In addition, crevasses form to accommodate strain induced by local disturbances in the ice flow, such as turns in the glacier direction and resistant bedrock outcrops below the glacier. In places, debris-covered portions of the glacier can be distinguished from the surrounding mountainside because crevasses in the underlying ice pull the debris apart (Figure 5.40d).

Fig. 5.39: Glacial features

Below the ELA, in the ablation zone, the ice experiences compression and thickening to compensate for a negative surface mass balance. Uplift caused by compression is (roughly) in balance with melting at the surface. Ice flux decreases from the ELA to the glacier toe, reflecting the increasing volume of ice that has been lost to melting. Crevasses are less common downstream, reflecting the

Fig. 5.40: Crevasses and other ice deformation features in Nisqually Glacier

compressional regime that tends to close them. Some glaciers have thrust faults in the ablation zone, but these are hard to see from a distance on a debris-covered glacier (they are identified by dipping, arcuate bands of sediment outcropping at the glacier surface) and we could not see whether Nisqually has them. The debris cover on the glacier surface becomes thicker downstream, reflecting the selective removal of ice (but not sediment) by melting. Thick debris can act to insulate the glacier surface and reduce melting, counteracting the albedo effect seen with thin debris cover.

Like most mountain glaciers in the summer, this glacier toe hosts an outlet of the subglacial hydrological system. This outlet is a large (several meters) tunnel from which a proglacial stream emerges (Figure 5.41a). The fact that meltwater is released from a single coherent point, rather than diffusely across the entire toe, reflects a highly organized and efficient subglacial hydrological network. Underneath the glacier, small pipes feed into large pipes in a dendritic system similar to subaerial rivers and tributaries. These pipes can be carved into the bedrock, melted out of the overlying ice, or both (the outlet visible at the toe of this glacier appeared to be carved upwards into the ice, although we only saw it from a distance). These pipes carry a large volume of water without lubricating much of the basal area. Efficient subglacial hydrological networks are a common feature of glaciers that have to move large quantities of meltwater in the summer. Generally these

systems take several weeks to develop; in the interim, glaciers often experience a spring speed-up when water spreads out over the bed before the hydrological system has developed the capacity to move the water efficiently. Once the efficient system develops, large amounts of water may be in motion below the glacier, but the pipes that carry this water occupy only a small fraction of the basal area, reducing lubrication. However, sudden spikes in water input (such as from rainstorms) can temporarily overwhelm the system and cause water to spread out on the bed.

Stop 4: Moraine Trail

Several of us took the Moraine Trail, which is an ‘unmaintained’ path going out to the crest of one of the LIA lateral moraines of Nisqually Glacier and then back in a loop. The trail was steep and slippery but easy to follow, despite being ‘unmaintained’. The return part of the loop included a steep ascent that would have been dangerous going downhill. Take a right at the fork to make sure you take the steep slope going uphill, which is safer. Trail runs along the top of the LIA lateral moraine (Figure 5.41b).

Up close we observed that the glacier tongue splits in two, with exposed bedrock in the middle.

The ice surface is extremely dirty, and in places can be hard to distinguish from un-vegetated valley floor/walls. However, the ice surface (where it is exposed) appears darker than the rock and the glacier toe has multiple holes representing abandoned outlets of the subglacial hydrological system.

Both branches of the glacier tongue have water outlets. The larger branch has the hydrologic outlet roughly in the middle, while the smaller branch has an outlet near the contact with the lateral moraine.

Nisqually Glacier is relatively well-studied. Its terminus position has been monitored since the 1940’s because of water resource concerns in the downstream river valley. It advanced between the 1940’s and the 1970’s, then began a retreat that continues today. Currently, the terminus is in a position similar to where it was in the 1940’s. Retreat can also be inferred between the mid-1800s LIA moraines and the 1940’s, prior to continuous monitoring.

Fig. 5.41: Views from Moraine Trail



(a) Hydrological outlet at base of Nisqually



(b) Hiking edge of LIA lateral moraine

5.8. Day 8, August 10, 2014: Mt. St. Helens - Windy Ridge

HELEN JANISZEWSKI AND GE JIN

9:00 am	Departed campsite, drove toward Windy Ridge via Forest Road 25
9:50 am	Stop 1: Bear Meadow
10:20 am	Stop 2: Donnybrook Viewpoint
10:35 am	Stop 3: Windy Ridge
11:40 am	Began hike at Windy Ridge trailhead
12:15 pm	Stop 4: Windy Ridge Trail
12:50 pm	Lunch at junction between Abraham and Windy Ridge Trails
1:30 pm	Stop 5: Truman Trailhead
1:50 pm	Stop 6: Pumice Plain
3:55 pm	Returned to Windy Ridge parking lot
4:15 pm	Stop 7: Miner's Car
4:30 pm	Headed back to Iron Creek Campground via Forest Road 26. This road has very significant potholes.
5:30 pm	Arrived at Iron Creek Campsite

Stop 1: Bear Meadow

From this point Gary Rosenquist and his friends captured 22 pictures of the landslide and the following lateral blast at Mt. St. Helens on May 17, 1980 (Figure 5.42). After the eruption, the Rosenquist group struggled to escape the area by driving east. Ash blocked the sunlight and rained on their windshield. It took them hours to drive out and luckily their engine was not choked by the ash.

Activity prior to the eruption started as early as March 1980. As concern mounted, scientists started to closely monitor the volcano. In these two months, the north side of the volcano rapidly expanded, with outward growth eventually reaching a rate of about 1 m/day just before the eruption. A spike in small magnitude earthquakes was also observed. Restricted areas were established around the volcano, but these were based on the assumption that the volcano would erupt vertically. Bear Meadow was not cordoned off but, as Rosenquist *et al* found, was greatly affected by the eruption.



Fig. 5.42: Gary Rosenquist's photographs from the 1980 eruption, and the view of Mt. St. Helens from Bear Meadow.

The eruption started with an magnitude 5 earthquake that triggered a landslide. The mass movement of the landslide decompressed the magmatic system, which led to the ensuing lateral blast.

Stop 2: Donnybrook Viewpoint

The 1980 eruption created hummocky deposits, which are observable from this viewpoint. The eruption's lateral blast downed trees in the surrounding area such that, even today, they lie in a radial pattern pointing outwards from the volcano. Logs can still be seen floating in Spirit Lake over 30 years after the eruption. The blast brought material up to the ridge, which sadly killed the USGS geologist David Johnston, after he transmitted his last words: "Vancouver! Vancouver! This is it!". His remains were never found. The Johnston Ridge Observatory, which overlooks St. Helens today, is named after him.



Fig. 5.43: Spirit Lake with tree deposits, valleys and ridges

Stop 3: Windy Ridge

We were given a short lecture by Heather Wright, who works for the USGS Volcano Observatory - Disaster Response and Mitigation Program (Figure 5.44).

Mt. St. Helens has been active since 300 ka; however, much of the edifice construction has been relatively recent and most of the topography evident today is less than 3000 years old. Several dome structures exist in the center of the crater, including the 1100-1200 ybp Sugar Bowl Dome and the dome that formed after the 1980 eruption (Figure 5.45).

The eruption history of Mt. St. Helens can be divided into four different stages (from youngest to oldest): Spirit Lake, Swift Creek, Cougar, and Ape Cave. The most recent Spirit Lake stage is divided into six periods: Modern, Goat Rocks, Kalama, Sugar Bowl, Castle Creek, Pine Creek, and Smith Creek. The material from the Spirit Lake stage is more depleted in incompatible elements relative to other Cascade volcanos, suggesting that the source had already been depleted. During the Kalama Period the two largest eruptions produced more than 2 km^3 of erupted material, and the third largest had about 0.5 km^3 .

Biologists have found that only two species of trees are still floating in Spirit Lake after the 1980 eruption. Most trees have sunk to the bottom of the lake, where some are standing vertically. Due to the influx of decaying biologic material following the eruption, Spirit Lake became filled with bacteria such as E. coli, and even "brain-eating" bacteria. Fish were illegally restored to the lake, probably by a private airplane drop.

The most recent eruptive episode started in 2004, and several domes were produced from 2004-2008. These domes pushed on the crater glacier, making it the only advancing glacier in the North America.

At this location, Zach also gave us a short introduction to the iMUSH project, a seismic exploration of Mt. St. Helens (see Section 4.1.2).



Fig. 5.44: USGS geologist Heather Wright and her students/postdocs.



Fig. 5.45: The view of Mt. St. Helens from the Windy Ridge trail. The dome generated during the Sugar Bowl period can be seen in the center of the crater.

Stop 4: Windy Ridge Trail

Fig. 5.46: Left: Old lava flow. Right: volcanic breccia.

At a brief stop along the road from Windy Ridge we encountered volcanic breccia surrounded by pumice deposits (Figure 5.46). It is likely not from the modern eruptive period, and may be a block and ash flow - a cooler debris flow than a pyroclastic flow.

About 50m down the road we dug into some sedimentary layers (Figure 5.47). The deposit layer we found here is well-sorted alternating fine and coarse grained material, indicating that it is a fall deposit (air-transported). Differences in clast size are likely due to the waxing and waning of the eruptive cycle.



Fig. 5.47: Fall deposit from the volcano.

Stop 5: Truman Trailhead

The outcrop comprised low-density plagioclase-rich porphyritic rock (Figure 5.48). These rocks are usually formed within the magmatic system over a long period of time as it slowly cools. The residence time of the magma can be determined from isotope analysis using Thorium-230 and Radium-226 dating. In the case of Mt. St. Helens, a crystallization time from 2000 yr - 1 Ma is

measured. This can help to determine how much magma within the system is depleted and how much can stay molten during an eruption.

The porphyritic texture of the rock is generated by volatiles (primarily H₂O) within the magma that exsolve to form bubbles as the pressure decreases near the surface. This loss of volatiles also increases the solidus temperature, which causes the magma to crystalize fine-grained crystals (a microlitic texture). If exhumation is too rapid, microlitic crystals will not have time to form.

Stop 6: Pumice Plain

We reached an outcrop of cryptodome material that is within the blast zone of the 1980 eruption. This blast deposit is composed mainly of fine-grained, crystalline, magmatic material (Figure 5.49). We observed distinctly light/dark igneous rocks, where their colour is probably related to different water content (Figure 5.50). The cooling of the magma body causes the rocks to become brittle and break easily.



Fig. 5.48: Low-density igneous rock with porphyritic texture.



Fig. 5.49: Left: blast deposit, right: igneous rocks in the deposit.



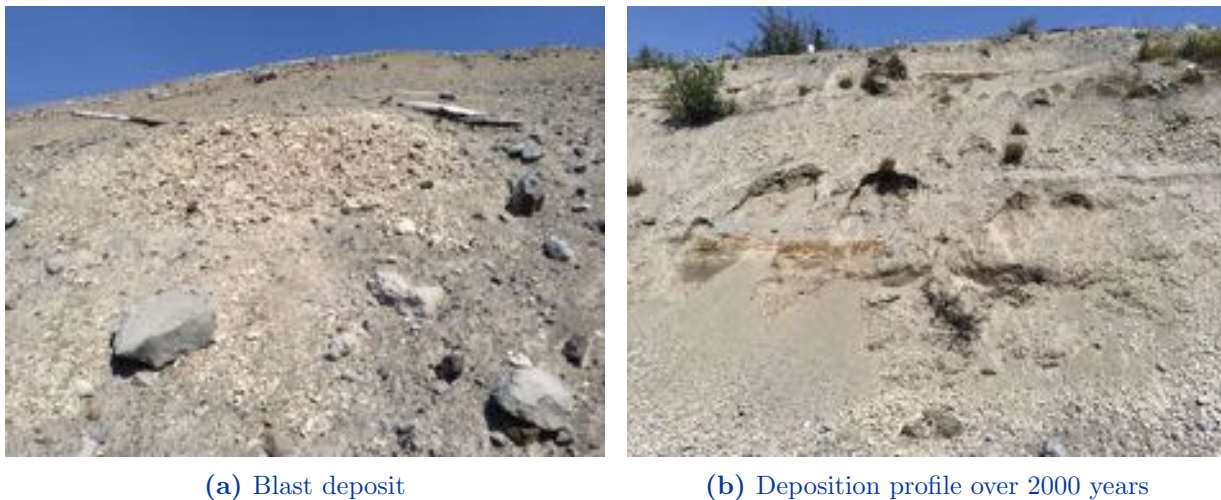
Fig. 5.50: Left: cooling feature, right: light and dark bands.

Further along the trail we found an outcrop of pyroclastic flow deposit containing very poorly sorted coarse to fine grained material (Figure 5.51). These features indicate that it is a flow deposit.



Fig. 5.51: Flow deposit

A lens of lighter material and some dead trees can be found within the Kalama period deposits (Figure 5.52a). This outcrop contains deposits from the Kalama Period (1400-1500), but the lens is from the Goat Rocks period (1800) (Figure 5.52b). This deposit was ripped up and redeposited during the 1980 eruption, explaining the jumbled stratigraphy.



(a) Blast deposit

(b) Deposition profile over 2000 years

Fig. 5.52: Deposits from past eruptions at Mt. St. Helens.

Stop 7: Miner's Car

On our way back to the campsite we stopped at the Miner's Car National Monument site near Mt. St. Helens. This car was destroyed during the 1980 eruption (Figure 5.53). It was tossed far from its original location by the power of the blast. The car belonged to Donald and Natalie Parker who, with their nephew, were staying at a cabin close to the Black Rock copper mine. This is approximately 9 miles from the volcano and was deemed a safe zone prior to the eruption. The family was among the 57 people killed during the eruption; 53 of these were in locations thought to be safe.



Fig. 5.53: The Parkers' car where it remains today.

We took an alternate route back to our campsite, the less-travelled Forest Road 26. This road is very narrow in parts and has significant potholes and dips. While we were able to drive it in minivans, it may be best to use higher clearance vehicles. There were very nice views of the trees that were knocked over in the radial blast from the eruption (Figure 5.54).



Fig. 5.54: Trees killed during the eruption. In the lower left hand corner of the picture, you can see how they have been knocked over in a radial pattern by the blast.

5.9. Day 9, August 11, 2014: Mt. St. Helens - Ape Caves

RAJ MOULIK

8:30 am	Departed campsite
9:35 am	Stop 1: Clearwater Overlook on the east side of Mt. St. Helens
10:30 am	Stop 2: Pine Creek Boulder
11:30 am	Stop 3: Ape Caves
1:40 pm	Lunch at Ape Caves
5:00 pm	Stop 4: Harry Gardner Park
6:45 pm	Arrived at Millersylvania State Park campground

The schedule for the day involved a long drive from Iron Creek Campground near Mt. St. Helens to Millersylvania Campground, en route to the Olympic peninsula.

Stop 1: Clearwater Overlook

We stopped on the east side of Mt. St. Helens at the Clearwater Overlook. This location provides a panoramic view of the broad, U-shaped glacial valley along the Clearwater Creek. The valley was carved by a glacier of Hayden Creek age (~ 140 ka, i.e. before the last glacial maximum) and possibly by an earlier glacier. The forests are mostly healthy in this part of the park, while some fallen trees from the blast zone are visible down the Clearwater Creek to the north. Several debris slides have occurred; the fallen trees mean the root-less soil lacks cohesive strength.

Across the road (east) from the parking area is an outcrop with a contact between lighter-colored, fine-grained, felsic dacite and dark, porphyritic basalt. The dacite is composed of lighter plagioclase feldspar and has miarolitic cavities: vesicles filled with later fluids that crystallize minerals incompatible with silicate granite. The dacite has few crystals as it is extrusive but does show some devitrification resulting in small crystals.



Fig. 5.55: Clearwater Overlook

Stop 2: Pine Creek Boulder

The second stop of the day was at the Pine Creek Boulder, a boulder weighing 37 tons carried by a lahar from the 1980 eruption of Mt. St. Helens. Lahars are high-density mudflows that have similar physical characteristics as wet cement and can suspend big boulders.

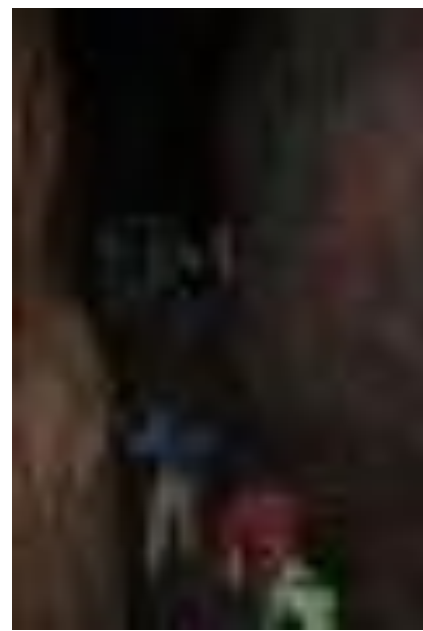


Stop 3: Ape Caves

The third stop was Ape Caves, the longest lava tube in the lower 48 states. There are two routes at this location: the Lower Ape Cave and the Upper Ape Cave. The lower cave is the shorter and easier route. We hiked the Upper Ape Cave, a lava tube that is 1.5 mile long. It had many boulder piles where one had to scramble over rocks and an 8-foot high lava fall with a rope anchored to climb it. There is no lighting in the tube except for an occasional skylight. Bright headlamps are a MUST for safety; headlamps are preferred so as to keep hands free for rock scrambling. Lava stalactites and stalagmites and flow marks could be seen on the walls and floor of the cave.



(a) View down a corridor in the upper Ape Cave.



(b) Scaling the 8 ft lavafall.

Fig. 5.57: Ape Caves.

Stop 4: Harry Gardner Park

The final stop was at Harry Gardner Park, which sits at the confluence of the north and south forks of the Toutle River. We observed two layers with similar material, separated by a distinct contact. The layers are poorly sorted with trees sticking out of the lower layer. These deposits contain a variety of clasts and are known to be lahar deposits from the 1980 eruption. The lahar velocities were different along the north and south fork; the one along the north fork had entrained ice and got dammed but eventually flowed over lahar deposits from the south fork. The lahar along the south fork picked up gravel quickly and was deposited two hours earlier.



Fig. 5.58: Harry Gardner Park

5.10. Day 10, August 12, 2014: Mima Mounds and Ruby Beach

CHLOE GAO, KEREN MEZUMEN, NANDINI RAMESH

8:50 am	Departed campsite
9:15 am	Stop 1: Mima Mounds Natural Area Preserve
10:00 am	Departed Mima Mounds for drive northwards
2:00 pm	Brief stop at Kalaloch Campground and then depart for Ruby Beach
2:15 pm	Stop 2: Ruby Beach
4:20 pm	Arrived at Kalaloch and have dinner

Stop 1: Mima Mounds Natural Area Preserve

The Mima Mounds Natural Area Preserve is a National Natural Landmark known for its mysterious mounded landscape, which is covered by prairie grassland. The mounds are small regularly-spaced circular or elliptical hills about 10 meters apart and 2.5 meters in height (Figure 5.59). The mounds are composed primarily of gravel. There are about 8 to 10 mounds per acre, and the preserve covers 637 acres.



Fig. 5.59: Mima Mounds

There are similar mounds in North America; pimple mounds by the Gulf of Mexico, prairie mounds in the northern Great Plains and hogwallow mounds in California (Figure 5.60).

The origin of Mima Mounds has left scientists puzzled since the mid 19th century. It is now known that these mounds were formed after the glaciers of the Last Glacial Maximum started to recede about 16,500 years ago (Figure 5.60, upper right). Around 16,500 years ago, the southern-most

edge of the glaciation in Washington covered the Mima Prairie. After the ice melted, ice-raftered debris/rock-mass was deposited across the area and became the prairie that we see today.

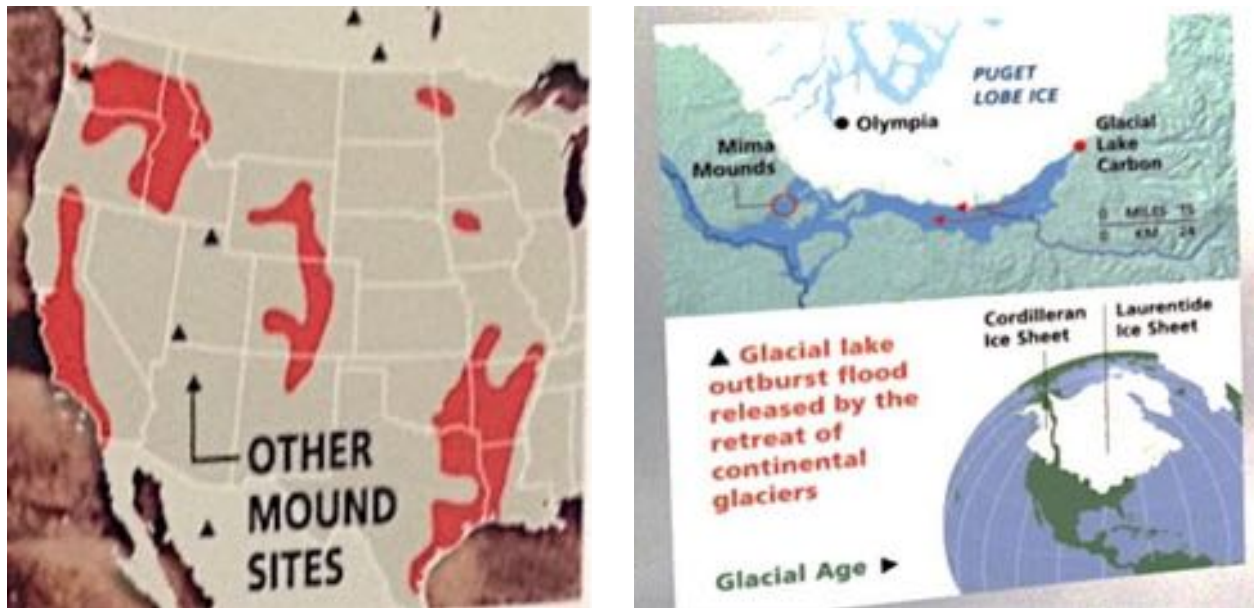


Fig. 5.60

Several theories for the origin of Mima mounds have been put forward yet none has been proven conclusively. Of the more than 30 explanations, the most popular ones include:

- **Glacial Ice:** Gravels and stones washed onto glaciers were gathered in suncups/pits, and as the ice melted, they were left behind in mounds.
- **Seismic activity:** Vibrational shock waves travel through soil, and mounds are formed at points of constructive interference, while dips form where waves cancel each other out. However, many earthquakes have taken place since, and none left similar mounds.
- **Fluvial deposition:** The mounds are deposits from glacially dammed lakes with sediment-rich floods, and water flowed around vegetation where sediments collected.
- **Erosion:** Glacial meltwater eroded the soil between plants (trees and shrubs), leaving mounded sediments around the vegetation.
- **Pocket gophers/ fossorial rodent hypothesis:** Small burrowing rodents, pocket gophers, built these mounds as shelters/nest chambers to stay above perched water tables. As the gophers excavated beneath the soil, they moved dense layers of glacial deposits upward, thus forming mounds. However, it has been argued that the mounds were there before the gophers moved into the area.
- **Permafrost cracking:** Ice formed wedges in cracked permafrost (frozen ground), and as the ice melted, only mounded soil remained.

Stop 2: Ruby Beach

Ruby beach is a pebble beach with sea stacks and tidal pools (Figure 5.61). On the beach, we observed a large number of stranded velella, a genus of deep blue hydrozoans, similar to the Portuguese man-of-war, that are made up of a number of polyps. These live on the surface of the sea and are propelled by the action of the wind using a small, sail-like protrusion that breaches the surface. Mass strandings of velellae occur every few years in this region and are, in general, driven by changes in the direction of the wind that lead to these being washed ashore. There is a large amount of driftwood that collects on this beach thanks to the logging activity in the region.

In the northern section of the beach there are cliffs as well as sea stacks. We found the sea stacks to be composed in some cases of fine-grained sandstone, and in other cases of a poorly-sorted conglomerate with angular clasts and large chunks of mudstone. These formations are olistostromes: rocks that were consolidated after an underwater mudslide and subsequently exposed.

Another feature observed at Ruby beach was the sorting of pebbles along the tide line. As the rounder pebbles are more inclined to roll down the slope and into the water, the pebbles remaining on the beach further from the tide line are flatter or more irregularly shaped than those closer to the water.



Fig. 5.61: Ruby Beach

5.11. Day 11, August 13, 2014: Olympic National Park and the Hoh Rainforest

CHLOE GAO, KEREN MEZUMEN, NANDINI RAMESH

9:05 am	Morning discussion and campsite departure
9:50 am	Breakfast at Forks Coffee Shop
10:45 am	Stop 1: Forks Timber Museum
12:00 pm	Lunch in Forks
2:10 pm	Stop 2: Hoh Rainforest
5:00 pm	Stop 3: Kalaloch Beach
5:30 pm	Returned to campsite

Stop 1: Forks Timber Museum

The Forks Timber Museum records information on the logging industry on the Olympic Peninsula from its settlement in the late 19th century through the late 20th century. The Olympic Peninsula receives the highest rainfall in the lower 48 states, averaging over 100 inches annually. This has produced fertile ground for logging. At first, logging was mostly done by local settlers, using low-tech methods. The industry grew markedly during World War I, when demand for lumber was high. Forks eventually became known as the logging capital of the world. The life of a lumberjack was, and is, hard and dangerous, with high risk of injury and death from the machinery used for large scale logging.



Fig. 5.62: Signpost by the Forks Timber Museum.

Stop 2: Hoh Rainforest

The hikes we did in the park were not strenuous and had magnificent natural sights (Figure 5.63). We started with the Hall of Moss Trail, a 0.8 mile loop through old growth temperate rain forest, with 100 ft elevation gain. This trail exhibits more than 100 types of mosses. Forest rangers provide guided tours open to the public. The climate is moist when not raining and it is advisable to bring a rain jacket. The region receives some of the highest precipitation in the USA thanks to the orographic effect of the Olympic mountains and Cascades blocking the moisture-laden westerly winds from the Pacific, and experiences up to 200 inches of rainfall per year.

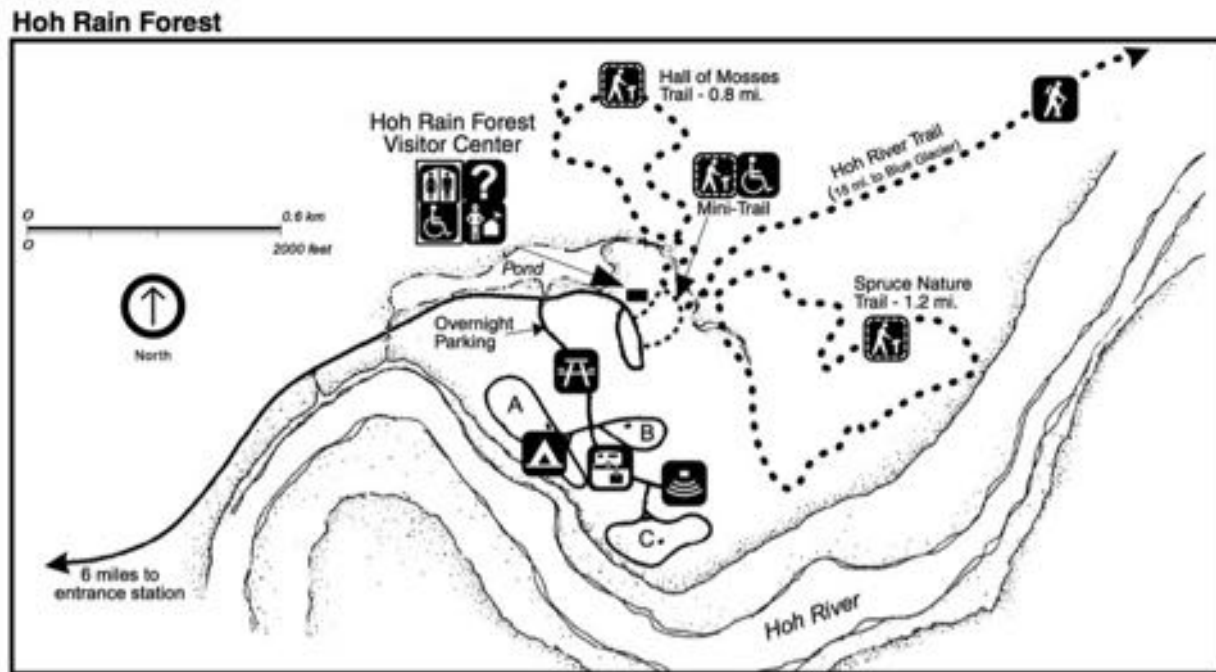


Fig. 5.63: Map of Hoh Rainforest trails

Due to the high rates of precipitation, the moisture in the ground is retained near the surface, rather than at depth. This leads the trees of the rainforest to develop very shallow root systems in order to take advantage of this moisture. As a result, the trees, not being deep-rooted, are easily toppled by the wind during the frequent storms occurring in the region. It is estimated that approximately 80% of tree deaths in this forest are caused by the wind.

The epiphytes found in this forest - primarily mosses and lichens - are a crucial part of the ecosystem (Figure 5.64). The relationship between the trees and epiphytes is symbiotic: the epiphytes use the trees for support and nutrients, while the trees have adapted to grow specialized lateral roots that re-absorb nutrients and moisture trapped in the moss and lichen layers.

The second hike, Spruce Nature Trail, is a 1.2 mile loop through the forest and the Hoh River. It is fairly flat with less than 100 foot elevation gain. The dominant tree species were the Sitka Spruce, Western Hemlock, and Douglas Fir; but other conifers and several deciduous species were present as well. According to the forest rangers, many are 100s years old and can reach 250 feet in height and 30 to 60 feet in circumference. When the group tried to measure the circumference, it took 8 students to hug one tree!



Fig. 5.64: Mosses in the Hoh Rainforest

This trail crosses both the glacier-fed Hoh river and the spring-fed Taft river, which are the primary water bodies that irrigate the rainforest. The Hoh river, being glacier-fed, has a much more variable path and flow volume than the Taft river.

Signboards along this trail provide descriptions of the common tree species, and also point out features in the forest. Among these are clearings used as grazing pastures by elk, toppled trees, and nurse log colonnades. ‘Nurse logs’ are the trunks of trees toppled by the wind. In an ecosystem where access to sunlight is highly competitive, these toppled trees provide a gap in the canopy that allow young saplings to grow rapidly as they are able to access sunlight. These saplings grow along the trunk of the fallen tree, using up the nutrients present in the organic matter. This results in sets of trees of approximately the same age growing in near-perfect rows known as



Fig. 5.65: Row of trees grown on a nurse log
In some cases, the remains of the fallen tree are still visible. It is estimated that 98% of the trees in the Hoh rainforest began as saplings on nurse logs.

Stop 3: Kalaloch Beach outcrop

The group speculated on the sequence of formation of this outcrop. We observed several layers of till that were formed by intermittent growth and shrinkage of glaciers in the Olympics, corresponding with the last interglacial period through the glacial sequence to the present. This was deduced after pieces of wood within the till were analyzed geochemically. On a macroscopic scale it is evident that we are in an active plate margin setting; there is a large thickness variation in the units we have observed here and further up the coast. The structure is broadly folded in the north-south direction, resulting from compression and rotation of the plates.

On the beach, we also observed large swarms of velella (see Section 5.10); there was a large swarm of these creatures along the entire west coast of the United States during the later summer of 2014.



Fig. 5.66: Washed up Velella at Kalaloch Beach.

6 Campsite Information

Deception Pass State Park

41229 WA-20, Oak Harbor, WA 98277

(360) 675-2417

Bathrooms, showers, water stations centrally located. Access to beach.

Horseshoe Cove Campground

Concrete, WA 98237

(888) 448-1474

Bathrooms, water stations centrally located. Within Mt. Baker-Snoqualmie National Forest, access to Baker Lake for swimming. About an hour drive out of the forest to the nearest gas station. Potentially bad mosquitos.

Daroga State Park

1 S Daroga Park Rd., Orondo, WA 98843

(509) 784-0229

Bathrooms, showers, water stations centrally located. The walk-in (~ 0.5 mi) campgrounds are on a man-made island that extends into the Columbia River, and can experience *extremely* windy conditions. Wheelbarrows are available to move equipment from the parking area to the campground. Access to Columbia River for swimming.

Silver Springs Campground

Highway 410, Enumclaw, WA 98022

(541) 338-7869

Bathrooms, water stations centrally located. Within Mt. Baker-Snoqualmie National Forest, just outside of Mt. Rainier National Park's northern entrance.

Iron Creek Campground

Randle, WA 98377

877-444-6777

Vault toilet, water stations centrally located. Within Gifford Pinchot National Forest, about a 40 minute drive to Mt. St. Helens. Creek access available for swimming.

Millersylvania State Park

12245 Tilley Road S., Olympia, WA 98512

(360) 753-1519

Bathrooms, showers, water stations centrally located. Access to Deep Lake for swimming. Boat rentals available.

Kalaloch Campground

Forks, WA 98331

(360) 565-3131

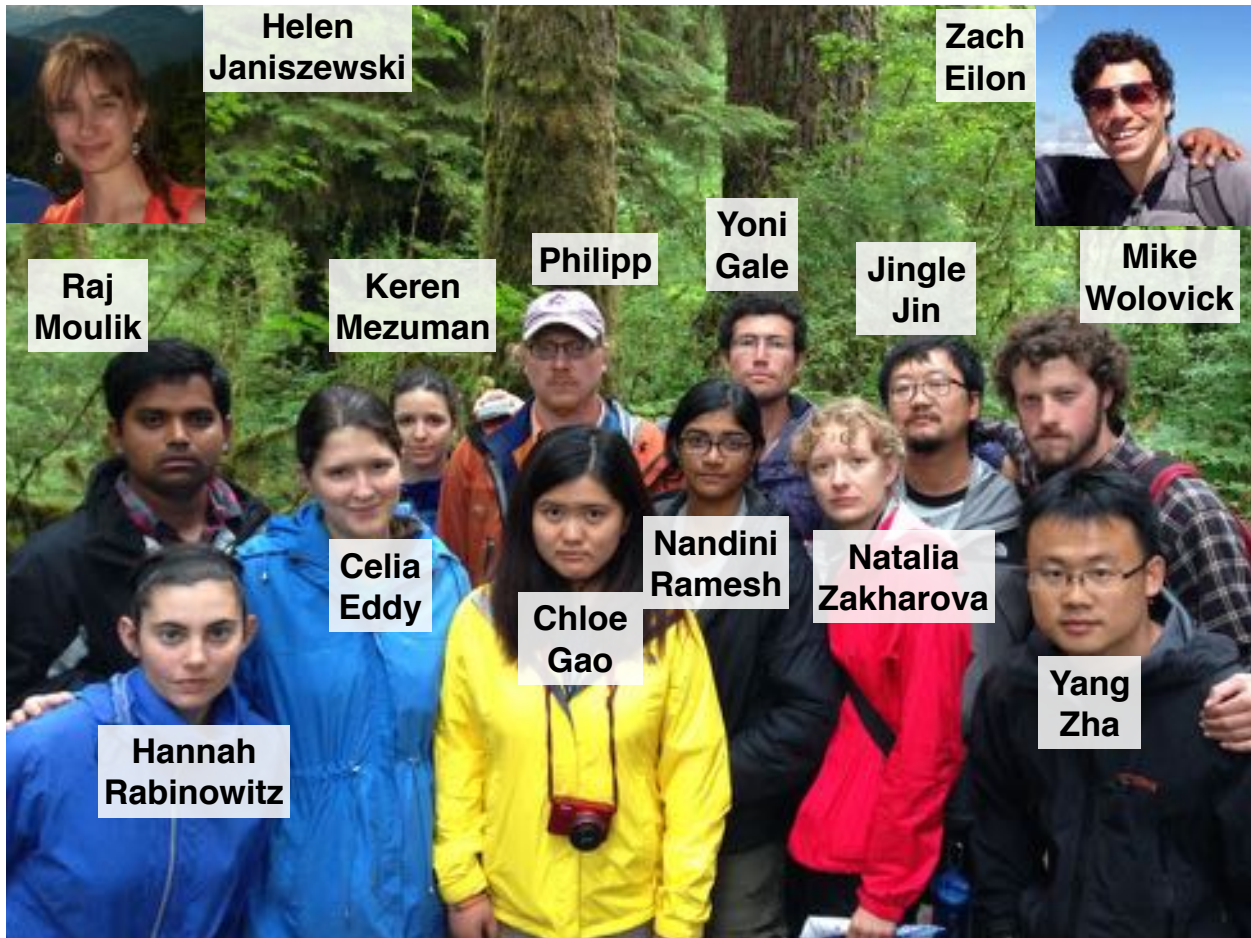
Bathrooms, water stations centrally located. Within the Olympic National Park, about 10 minutes south of Ruby Beach. Beach access available. Be prepared for rain. Very popular campground so reservations are needed early.

7 Trip Budget

The budget for the field trip was initially \$8,800. In order to reduce costs to ensure that we stayed within this budget, we were careful with our food expenditures (which was the only adjustable part of the budget). Specifically, we kept a running inventory of food (including left-over ingredients from previous meals) to reduce the waste. This allowed us to come in substantially under budget on the food in order to make up for higher-than-expected expenditures on miscellaneous items.

Item	Cost	Expected
Campsite	\$853.50	\$900.00
Transport	\$4470.97	\$4850.00
Food	\$1362.87	\$1980.00
Miscellaneous	\$1390.85	\$1070.00
Grand Total	\$8078.19	\$8800.00

8 Trip Participants



Philipp Ruprecht, Lamont Assistant Research Professor, Geochemistry

Celia Eddy, Seismology; **Zach Eilon**, Seismology; **Jonathan Gale**, Geology; **Chloe Gao**, Atmospheric Science; **Helen Janiszewski**, Seismology; **Ge Jin (Jingle)**, Seismology; **Keren Mezuman**, Atmospheric Science; **Raj Moulik**, Seismology; **Hannah Rabinowitz**, Rock Mechanics; **Nandini Ramesh**, Physical Oceanography; **Mike Wolovick**, Glaciology; **Natalia Zakharova**, Borehole Geophysics and Carbon Sequestration; **Yang Zha**, Seismology.

9 Acknowledgements

We gratefully acknowledge the Storke Fund for providing financial support that makes this and other trips possible. They have proved educational and social highlights of our time as graduate students; long may they continue!

We thank Philipp Ruprecht for leading the trip, helping to plot our route, and setting us up with local experts. More generally we appreciate what an informative and enthusiastic guide he was on all subjects volcanological, petrological, and phrenological.

We appreciate the time and effort of Tom Sisson and Heather Wright, who made room in their busy schedules to teach us about the area and, in the case of Tom, intrepidly lead us over hill and dale.

We are very grateful to the organizing committee, Celia Eddy, Zach Eilon, Jonathan Gale, Helen Janiszewski, Pritwiraj Moulik, and Hannah Rabinowitz. They put tremendous amounts of time and effort into planning, budgeting, and executing this trip. Securing funding was a real challenge, and they not only managed to do this, but made it stretch a long way to fund a protracted and memorable trip.

Finally, we thank the compilers of this report: Celia Eddy, Zach Eilon, Helen Janiszewski, Hannah Rabinowitz, and Natalia Zakharova, for their above-and-beyond efforts putting this document together. They are the best people in the world.

Bibliography

- Geoffrey A. Abers, Laura S. MacKenzie, Stéphane Rondenay, Zhu Zhang, Aaron G. Wech, and Kenneth C. Creager. Imaging the source region of Cascadia tremor and intermediate-depth earthquakes. *Geology*, 37(12):1119–1122, 2009.
- Hemendra Acharya. Comparison of seismicity parameters in different subduction zones and its implications for the Cascadia Subduction Zone. *Journal of Geophysical Research*, 97(B6):8831, 1992.
- Nicholas T. Arndt and Steven L. Goldstein. Use and abuse of crust-formation ages. *Geology*, 15(10):893–895, 1987. doi: 10.1130/0091-7613(1987)15;893:UAAOCA;2.0.CO;2. URL <http://geology.gsapubs.org/content/15/10/893.abstract>.
- Brian F. Atwater. Evidence for great Holocene earthquakes along the outer coast of Washington state. *Science*, 236(4804):942–944, 1987.
- Brian F. Atwater and Andrew L. Moore. A tsunami about 1000 years ago in Puget Sound, Washington. *Science*, 258(5088):1614–1617, 1992. doi: 10.1126/science.258.5088.1614. URL <http://www.sciencemag.org/content/258/5088/1614.abstract>.
- T. Atwater. Plate tectonic history of the North Pacific Ocean, animation. <http://emvc.geol.ucsb.edu/2infopgs/IP3RegTect/dNoPacific.html>.
- T. Atwater. Implications of plate tectonics for the Cenozoic tectonic evolution of western North America. *Geological Society of America Bulletin*, 81(12):3513–3536, 1970. doi: 10.1130/0016-7606(1970)81[3513:IOPTFT]2.0.CO;2. URL <http://gsabulletin.gsapubs.org/content/81/12/3513.abstract>.
- Pascal Audet, Michael G. Bostock, Nikolas I. Christensen, and Simon M. Peacock. Seismic evidence for overpressured subducted oceanic crust and megathrust fault sealing. *Nature*, 457(7225):76–78, 2009.
- Mike Barna, Brian Lamb, Susan O'Neill, Hal Westberg, Cris Figueroa-Kaminsky, Sally Otterson, Clint Bowman, and Jennifer DeMay. Modeling ozone formation and transport in the Cascadia region of the Pacific Northwest. *Journal of Applied Meteorology*, 39(3):349–366, 2000.
- R.L. Beschta and W.J. Ripple. Wolves, trophic cascades, and rivers in the Olympic National Park, USA. *Ecohydrology*, 1:118–130, 2008.
- M. G. Bostock, R. D. Hyndman, S. Rondenay, and S. M. Peacock. An inverted continental Moho and serpentinization of the forearc mantle. *Nature*, 417(6888), 2002.
- E. H. Brown, J. Y. Bradshaw, and G. E. Mustoe. Plagiogranite and keratophyre in ophiolite on Fidalgo Island, Washington. *Geological Society of America Bulletin*, 90(5):493–507, 1979. URL <http://gsabulletin.gsapubs.org/content/90/5/493.abstract>.
- Paul Budkewitsch and Pierre-Yves Robin. Modelling the evolution of columnar joints. *Journal of Volcanology and Geothermal Research*, 59(3):219–239, January 1994.

- B. C. Burchfiel, D. S. Cowan, and G. A. Davis. Tectonic overview of the cordilleran orogen in the western u. s. In B. C. Burchfiel, P. W. Lipman, and M. L. Zoback, editors, *The Cordilleran Orogen: conterminous U. S.: The Geology of North America*, volume G-3, pages 407–480. Geological Society of America, Boulder, 1992.
- Luigi Burlini, Giulio Di Toro, and Philip Meredith. Seismic tremor in subduction zones: Rock physics evidence. *Geophysical Research Letters*, 36(8), 2009. doi: 10.1029/2009GL037735.
- V.E. Camp. Mid-miocene propagation of the yellowstone mantle plume head beneath the columbia river basalt source region. *Geology*, 23(5):435–438, 1995.
- V.E. Camp and M.E. Ross. Mantle dynamics and genesis of mafic magmatism in the intermontane pacific northwest. *Journal of Geophysical Research: Solid Earth (1978–2012)*, 109(B8), 2004.
- G.K.C. Clarke. Subglacial processes. *Annual Review of Earth and Planetary Sciences*, 33: 247–276, 2005. ISSN 0084-6597. doi: 10.1146/annurev.earth.33.092203.122621.
- Peter J Coney, David L Jones, and James W H Monger. Cordilleran suspect terranes. *Nature*, 288 (5789):329–333, 1980.
- K.M. Cuffey and W.S.B. Paterson. *The Physics of Glaciers*. Butterworth-Heinemann/Elsevier, Burlington, MA, 4 edition, 2010.
- C. DeMets and T. H. Dixon. New kinematic models for pacific-north america motion from 3 ma to present: 1. evidence for steady motions and biases in the nuvel1a model. *Geophys. Res. Lett.*, 26(13):1921–1924, 1999.
- D. J. DePaolo, A. M. Linn, and G. Schubert. The continental crustal age distribution: Methods of determining mantle separation ages from sm-nd isotopic data and application to the southwestern united states. *Journal of Geophysical Research: Solid Earth*, 96(B2):2071–2088, 1991. ISSN 2156-2202. doi: 10.1029/90JB02219. URL <http://dx.doi.org/10.1029/90JB02219>.
- William R. Dickinson. Tectonic setting of faulted tertiary strata associated with the catalina core complex in southern arizona. *Geological Society of America Special Papers*, 264:1–106, 1991. doi: 10.1130/SPE264-p1. URL <http://specialpapers.gsapsubs.org/content/264/1.abstract>.
- William R. Dickinson. Tectonic implications of cenozoic volcanism in coastal california. *Geological Society of America Bulletin*, 109(8):936–954, 1997. doi: 10.1130/0016-7606(1997)109;0936:OTIOCV;2.3.CO;2. URL <http://gsabulletin.gsapsubs.org/content/109/8/936.abstract>.
- William R. Dickinson. Geotectonic evolution of the great basin. *Geosphere*, 2(7):353–368, 2006. doi: 10.1130/GES00054.1. URL <http://geosphere.gsapsubs.org/content/2/7/353.abstract>.
- DNR. Geology of washington. <http://www.dnr.wa.gov/ResearchScience/Topics/GeologyofWashington/Pages/geolofwa.aspx>, 2014.
- H Dragert, K Wang, and G Rogers. Geodetic and seismic signatures of episodic tremor and slip in the northern cascadia subduction zone. *Earth, Planets and Space*, 56(12):1143–1150, 2004.

- R.L. Edmonds and R.D. Blew. Trends in precipitation and stream chemistry in a pristine old-growth forest watershed, olympic national park, washington. *Journal of the American Water Resources Association*, 33(4):781–793, 1997.
- R.L. Edmonds and G.L.D. Murray. Overstory litter inputs and nutrient returns in an old-growth temperate forest ecosystem, olympic national park, washington. *Canadian Journal of Earth Sciences*, 32:742–750, 2002.
- D. C. Engebretson, A. Cox, and G. A. Thompson. Correlation of plate motions with continental tectonics: Laramide to basin-range. *Tectonics*, 3(2):115–119, 1984. ISSN 1944-9194. doi: 10.1029/TC003i002p00115. URL <http://dx.doi.org/10.1029/TC003i002p00115>.
- W. G. Ernst. Metamorphic terranes, isotopic provinces, and implications for crustal growth of the western united states. *Journal of Geophysical Research: Solid Earth*, 93(B7):7634–7642, 1988. ISSN 2156-2202. doi: 10.1029/JB093iB07p07634. URL <http://dx.doi.org/10.1029/JB093iB07p07634>.
- Rob L Evans, Philip E Wannamaker, R Shane McGary, and Jimmy Elsenbeck. Electrical structure of the central Cascadia subduction zone: The EMSLAB Lincoln Line revisited. *Earth and Planetary Science Letters*, 2013.
- G. Lang Farmer and Donald J. DePaolo. Origin of mesozoic and tertiary granite in the western united states and implications for pre-mesozoic crustal structure: 1. Nd and sr isotopic studies in the geocline of the northern great basin. *Journal of Geophysical Research: Solid Earth*, 88 (B4):3379–3401, 1983. ISSN 2156-2202. doi: 10.1029/JB088iB04p03379. URL <http://dx.doi.org/10.1029/JB088iB04p03379>.
- Thomas J. Fitch. Plate convergence, transcurrent faults, and internal deformation adjacent to southeast asia and the western pacific. *Journal of Geophysical Research*, 77(23):4432–4460, 1972. ISSN 2156-2202. doi: 10.1029/JB077i023p04432. URL <http://dx.doi.org/10.1029/JB077i023p04432>.
- R.J. Fleck and R.E. Criss. Strontium and oxygen isotopic variations in mesozoic and tertiary plutons of central idaho. *Contributions to Mineralogy and Petrology*, 90(2-3):291–308, 1985. ISSN 0010-7999. doi: 10.1007/BF00378269. URL <http://dx.doi.org/10.1007/BF00378269>.
- R.W. Frenzel, G.W. Witmer, and E.E. Starkey. Heavy metal concentrations in a lichen of mt. rainier and olympic national parks, washington, usa. *Bulletin of environmental contamination and toxicology*, 44(1):158–164, 1990.
- L.H. Geiser and et al. Lichen-based critical loads for atmospheric nitrogen depositionin western oregon and washington forests, usa. *Environmental pollution*, 158(7):2412–2421, 2010.
- M Gerdom, A.M Treher, E.R Flueh, and D Klaeschen. The continental margin off oregon from seismic investigations. *Tectonophysics*, 329:79–97, 2000.
- Chris Goldfinger, C. Hans Nelson, and Joel E. and Johnson. Holocene earthquake records from the cascadia subduction zone and northern san andreas fault based on precise dating of offshore turbidites. *Annual Review of Earth and Planetary Sciences*, 31(1):555–577, 2003. doi: 10.1146/annurev.earth.31.100901.141246.

- Chris Goldfinger, C Hans Nelson, A Morey, Joel E Johnson, J Gutiérrez-Pastor, A T Eriksson, E Karabanov, J Patton, Eulàlia Gràcia, and R Enkin. Turbidite event history – Methods and implications for Holocene paleoseismicity of the Cascadia subduction zone. *U.S. Geological Survey Profesional Paper 1661-F*, 170:64, 2012.
- Gary G. Gray. Native terranes of the central klamath mountains, california. *Tectonics*, 5(7): 1043–1054, 1986. ISSN 1944-9194. doi: 10.1029/TC005i007p01043. URL <http://dx.doi.org/10.1029/TC005i007p01043>.
- Kenneth A. Grossenbacher and Stephen M. McDuffie. Conductive cooling of lava: columnar joint diameter and stria width as function of cooling rate and thermal gradient. *Journal of Volcanology and Geothermal Research*, 69(1-2):95–103, December 1995.
- A.M. Ho and K.V. Cashman. Temperature constraints on the ginkgo flow of the columbia river basalt group. *Geology*, 25(5):403–406, 1997.
- P. F. Hoffman. Belt basin: A landlocked remnant ocean basin? (analogous to the south caspian and black seas). In *Geological Society of America Abstracts with Programs*, volume 7, page A50, 1988.
- P.R. Hooper. Chemical discrimination of columbia river basalt flows. *Geochemistry, Geophysics, Geosystems*, 1(6):doi:10.1029/2000gc000040, 2000.
- P.R. Hooper, V.E. Camp, S.P. Reidel, and M.E. Ross. The origin of the columbia river flood basalt province: Plume versus nonplume models. In G.R. Foulger and D.M. Jurdy, editors, *Plates, plumes, and planetary processes*, volume 430, pages 635–668. Geological Society of America Special Papers, 2007.
- D. G. Howell. *Tectonics of Suspect Terranes, Mountain Building and Continental Growth*. Chapman and Hall, London, 1989.
- Eugene Humphreys. Relation of flat subduction to magmatism and deformation in the western united states. *Geological Society of America Memoirs*, 204:85–98, 2009. doi: 10.1130/2009.1204(04). URL <http://memoirs.gsapsubs.org/content/204/85.abstract>.
- Eugene D. Humphreys. Post-laramide removal of the farallon slab, western united states. *Geology*, 23(11):987–990, 1995. URL <http://geology.gsapsubs.org/content/23/11/987.abstract>.
- R.D. Hyndman, M. Yamano, and D.A. Oleskevich. The seismogenic zone of subduction thrust faults. *The Island Arc*, 6:244–260, 1997.
- Matt J. Ikari and Demian M. Saffer. Comparison of frictional strength and velocity dependence between fault zones in the nankai accretionary complex. *Geochemistry, Geophysics, Geosystems*, 12(4), 2011. doi: 10.1029/2010GC003442.
- E. Irving. Paleopoles and paleolatitudes of north america and speculations about displaced terrains. *Canadian Journal of Earth Sciences*, 16(3):669–694, 1979.
- Honn Kao, Shao-Ju Shan, Herb Dragert, and Garry Rogers. Northern cascadia episodic tremor and slip: A decade of tremor observations from 1997 to 2007. *Journal of Geophysical Research*, 114(June), 2009. doi: 10.1029/2008JB006046.

- Harvey M Kelsey, Alan R Nelson, Eileen Hemphill-Haley, and Robert C Witter. Tsunami history of an oregon coastal lake reveals a 4600 yr record of great earthquakes on the cascadia subduction zone. *Geological Society of America Bulletin*, 117(7):1009, 2005.
- Giorgi Khazaradze, Anthony Qamar, and Herb Dragert. Tectonic deformation in western washington from continuous gps measurements. *Geophysical Research Letters*, 26(20): 3153–3156, 1999. ISSN 1944-8007. doi: 10.1029/1999GL010458. URL <http://dx.doi.org/10.1029/1999GL010458>.
- D.H. Landers, S.I. Simonich, L.H. Jaffe, I.H. Geiser, D.H. Campbell, A.R. Schwindt, C.B. Schreck, M.L. Kent, W.D. Hafner, H.E. Taylor, K.J. Hageman, S. Usenko, L.K. Ackerman, J.E. Schrlau, N.L. Rose, T.F. Blett, and M.M. Erway. *The Fate, Transport, and Ecological Impacts of Airborne Contaminants in Western National Parks (USA)*. U.S. Environmental Protection Agency, Office of Research and Development, NHEERL, Western Ecology Division, Corvallis, Oregon, 2008.
- J. H. Lincoln. The puget sound model summary.
<http://exhibits.pacsci.org/pugetsound/PSSummary.html>, 2014.
- Lorraine E. Lisiecki and Maureen E. Raymo. A pliocene-pleistocene stack of 57 globally distributed benthic ^{18}O records. *Paleoceanography*, 20(1):n/a–n/a, 2005. ISSN 1944-9186. doi: 10.1029/2004PA001071. URL <http://dx.doi.org/10.1029/2004PA001071>.
- P.E. Long and B.J. Wood. Structures, textures, and cooling histories of columbia river basalt flows. *Geological Society of America Bulletin*, 97:1144–1155, 1986.
- R.S. Ludwin, R. Dennis, D. Carver, A.D. McMillan, R. Losey, J. Clague, C. Jonientz-Trisler, J. Bowechop, J. Wray, and K. James. Dating the 1700 cascadia earthquake: Great coastal earthquakes in native stories. *Seismological Research Letters*, 76(2):140–148, 2005.
- James R. Magill, Ray E. Wells, Robert W. Simpson, and Allan V. Cox. Post 12 m.y. rotation of southwest washington. *Journal of Geophysical Research: Solid Earth*, 87(B5):3761–3776, 1982. ISSN 2156-2202. doi: 10.1029/JB087iB05p03761. URL <http://dx.doi.org/10.1029/JB087iB05p03761>.
- S.D. Malone, E.T. Endo, C.S. Weaver, and Ramey J.W. Seismic monitoring for eruption prediction. In Peter W. Lipman and Donal R. Mullineau, editors, *1980 Eruptions of Mt. St. Helens*, volume 1250, pages 803–813. US Geological Survey Professional Papers, 1981.
- Chris Marone and C H Scholz. The depth of seismic faulting and the upper transition from stable to unstable slip regimes. *Geophysical Research Letters*, 15(8):621–624, 1988.
- B.S. Martin, H.L. Petcovic, and S.P. Reidel. *Goldschmidt Conference: Field trip guide to the Columbia River Basalt Group, PNNL-15221*. Pacific Northwest National Laboratory, Richland, Washington, 2005.
- M.A. Mast, D.J. Manthorne, and D.A. Roth. Historical deposition of mercury and selected trace elements to high-elevation national parks in the western u.s. inferred from lake-sediment cores. *Atmospheric Environment*, 44(21-22):2577–2586, 2010.
- Robert McCaffrey, Anthony I. Qamar, Robert W. King, Ray Wells, Giorgi Khazaradze, Charles A. Williams, Colleen W. Stevens, Jesse J. Vollick, and Peter C. Zwick. Fault locking, block

- rotation and crustal deformation in the pacific northwest. *Geophysical Journal International*, 169(3):1315–1340, 2007. ISSN 1365-246X. doi: 10.1111/j.1365-246X.2007.03371.x. URL <http://dx.doi.org/10.1111/j.1365-246X.2007.03371.x>.
- S.R. McNutt. Seismic monitoring and eruption forecasting of volcanoes: a review of the state-of-the-art and case histories. In R. Scarpa and R.I. Tilling, editors, *Monitoring and mitigation of volcano hazards*, pages 99–146. Springer Berlin Heidelberg, 1996.
- S.R. McNutt. Volcanic seismology. *Annual Review of Earth and Planetary Sciences*, 33:461–491, 2005.
- NAM. Paleogeography and geologic evolution of north america.
<http://pubs.er.usgs.gov/publication/fs20133014>, 2014.
- M R Nedimovic, DelWayne R Bohnenstiehl, Suzanne M Carbotte, J Pablo Canales, and Robert P Dziak. Faulting and hydration of the Juan de Fuca plate system. *Earth and Planetary Science Letters*, 284(1):94–102, 2009.
- Mladen R Nedimović, Roy D Hyndman, Kumar Ramachandran, and George D Spence. Reflection signature of seismic and aseismic slip on the northern Cascadia subduction interface. *Nature*, 424(6947):416–420, July 2003.
- Alan R Nelson, Brian F Atwater, Peter T Bobrowsky, Lee-Ann Bradley, John J Clague, Gary A Carver, Mark E Darienzo, Wendy C Grant, Harold W Krueger, Rodger Sparks, Thomas W Stafford, Jr, and Minze Stuiver. Radiocarbon evidence for extensive plate-boundary rupture about 300 years ago at the Cascadia subduction zone. *Nature*, 378(6555):371–374, November 1995.
- Alan R Nelson, Harvey M Kelsey, and Robert C Witter. Great earthquakes of variable magnitude at the Cascadia subduction zone. *Quaternary Research*, 65(3):354–365, May 2006.
- A.R. Nelson, S.Y. Johnson, R.E. Wells, S.K. Pezzopane, H.M. Kelsey, B.L. Sherrod, L. Bradley, R.D. Koehler, R.C. Bucknam, R. Haugerud, and W.T. Laprade. Field and laboratory data from an earthquake history study of the toe jam hill fault, bainbridge island, washington. *U.S. Geological Survey Open-File Report*, 02-0060, 2002.
- NOAA. Olympic coast 2008 sanctuary report.
<http://sanctuaries.noaa.gov/science/condition/ocnms/state.html>, 2008.
- NOAA. Olympic coast national monument sanctuary-habitat.
<http://olympiccoast.noaa.gov/living/habitats/habitats.html>, 2013.
- NOAA. Environmental history and features of puget sound.
<http://www.nwfsc.noaa.gov/publications/scipubs/techmemos/tm44/environment.htm>, 2014a.
- NOAA. Olympic national park-three parks in one, 2014b. URL
<http://www.nps.gov/olym/index.htm>.
- Kazushige Obara. Nonvolcanic deep tremor associated with subduction in southwest Japan. *Science*, 296(5573):1679–81, May 2002. ISSN 1095-9203. doi: 10.1126/science.1070378. URL <http://www.ncbi.nlm.nih.gov/pubmed/12040191>.

- Kazushige Obara and Shutaro Sekine. Characteristic activity and migration of episodic tremor and slow-slip events in central japan. *Earth, Planets and Space*, 61(7):853–862, 2009.
- Mathias Obrebski, Richard M. Allen, Mei Xue, and Shu-Huei Hung. Slab-plume interaction beneath the pacific northwest. *Geophysical Research Letter*, 37(14), 2010.
- Tom Parsons, Anne M. Trehu, James H. Luetgert, Kate Miller, Fiona Kilbride, Ray E. Wells, Michael A. Fisher, Ernst Flueh, Uri S. ten Brink, and Nikolas I. Christensen. A new view into the cascadia subduction zone and volcanic arc: Implications for earthquake hazards along the washington margin. *Geology*, 26(3):199–202, 1998.
- Stephen C. Porter and Terry W. Swanson. Radiocarbon age constraints on rates of advance and retreat of the puget lobe of the cordilleran ice sheet during the last glaciation. *Quaternary Research*, 50(3):205–213, November 1998. ISSN 0033-5894. doi: 10.1006/qres.1998.2004. URL <http://www.sciencedirect.com/science/article/pii/S003358949892004X>.
- L A Preston. Intraslab Earthquakes: Dehydration of the Cascadia Slab. *Science*, 302(5648):1197–1200, November 2003.
- S.P. Reidel. Emplacement of columbia river flood basalt. *Journal of Geophysical Research*, 103(B11):27,393–27,410, November 1998.
- S.P. Reidel, T.L. Tolan, P.R. Hooper, M.H. Beeson, K.R. Beeson, R.D. Bentley Fecht, and J.L. Anderson. The grande ronde basalt, columbia river basalt group; stratigraphic descriptions and correlations in washington, oregon, and idaho. *Volcanism and tectonism in the Columbia River flood-basalt province: Geological Society of America Special Paper*, 239:21–53, 1989.
- S.P. Reidel, V.G. Johnson, and F.A. Spane. *Natural Gas Storage in Basalt Aquifers of the Columbia Basin, Pacific Northwest USA: A Guide to Site Characterization*, Rep. PNNL-13962. Pacific Northwest Natl. Lab., Richland, Washington, 2002.
- Stephen P. Reidel, Victor E. Camp, Terry L. Tolan, and Barton S. Martin. The columbia river flood basalt province: Stratigraphy, areal extent, volume, and physical volcanology. *Geological Society of America Special Papers*, 497:1–43, 2013. doi: 10.1130/2013.2497(01). URL <http://specialpapers.gsapsubs.org/content/497/1.abstract>.
- Garry Rogers and Herb Dragert. Episodic tremor and slip on the Cascadia subduction zone: the chatter of silent slip. *Science (New York, N.Y.)*, 300(5627):1942–3, June 2003. ISSN 1095-9203. doi: 10.1126/science.1084783. URL <http://www.ncbi.nlm.nih.gov/pubmed/12738870>.
- Demian M. Saffer and Harold J. Tobin. Hydrogeology and mechanics of subduction zone forearcs: Fluid flow and pore pressure. *Annual Review of Earth and Planetary Sciences*, 39(1):157–186, 2011. doi: 10.1146/annurev-earth-040610-133408.
- Kenji Satake, Kelin Wang, and Brian F Atwater. Fault slip and seismic moment of the 1700 Cascadia earthquake inferred from Japanese tsunami descriptions. *Journal of Geophysical Research*, 108(B11):2535, 2003.
- J. C. Savage, J. L. Svare, W. H. Prescott, and M. H. Murray. Deformation across the forearc of the cascadia subduction zone at cape blanco, oregon. *Journal of Geophysical Research: Solid Earth*, 105(B2):3095–3102, 2000. ISSN 2156-2202. doi: 10.1029/1999JB900392. URL <http://dx.doi.org/10.1029/1999JB900392>.

- Christopher H Scholz. Earthquakes and friction laws. *Nature*, 391:37–42, 1998.
- R.W. Sheibley, E. Mihaela, P.W. Swarzenski, P.W. Moran, and J.R. Foreman. Nitrogen deposition effects on diatom communities in lakes from three national parks in washington state. *Water Air and Soil Pollution*, 225(2):1857, 2014.
- Brian L. Sherrod, Thomas M. Brocher, Craig S. Weaver, Robert C. Bucknam, Richard J. Blakely, Harvey M. Kelsey, Alan R. Nelson, and Ralph Haugerud. Holocene fault scarps near tacoma, washington, usa. *Geology*, 32(1):9–12, 2004. doi: 10.1130/G19914.1. URL <http://geology.gsapubs.org/content/32/1/9.abstract>.
- R.B. Smith, M. Jordan, B. Steinberger, C.M. Puskas, J. Farrell, S. Waite, Husen, W.L. Chang, and R. O'Connell. Geodynamics of the yellowstone hotspot and mantle plume: Seismic and gps imaging, kinematics, and mantle flow. *Journal of Volcanology and Geothermal Research*, 188(1):26–56, 2009.
- Joann Stock and Peter Molnar. Uncertainties and implications of the late cretaceous and tertiary position of north america relative to the farallon, kula, and pacific plates. *Tectonics*, 7(6):1339–1384, 1988. ISSN 1944-9194. doi: 10.1029/TC007i006p01339. URL <http://dx.doi.org/10.1029/TC007i006p01339>.
- A. M. Trehu, I. Asudeh, T. M. Brocher, J. H. Luetgert, W. D. Mooney, J. L. Nabelek, and Y. Nakamura. Crustal architecture of the cascadia forearc. *Science*, 266(5183):237–243, 1994. doi: 10.1126/science.266.5183.237. URL <http://www.sciencemag.org/content/266/5183/237.abstract>.
- D. Tucker. Fidalgo ophiolite. *Northwest Geology Field Trips*, 2014. URL <http://nwgeology.wordpress.com/the-fieldtrips/fidalgo-ophiolite-part-2/>.
- TM Van Wagoner, RS Crosson, KC Creager, G Medema, L Preston, NP Symons, and TM Brocher. Crustal structure and relocated earthquakes in the puget lowland, washington, from high-resolution seismic tomography. *Journal of Geophysical Research: Solid Earth (1978–2012)*, 107(B12):ESE–22, 2002.
- Roland von Huene and David W. Scholl. Observations at convergent margins concerning sediment subduction, subduction erosion, and the growth of continental crust. *Reviews of Geophysics*, 29(3):279–316, 1991. ISSN 1944-9208. doi: 10.1029/91RG00969. URL <http://dx.doi.org/10.1029/91RG00969>.
- Kelin Wang, Yan Hu, and Jiangheng He. Deformation cycles of subduction earthquakes in a viscoelastic Earth. *Nature*, 484(7394):327–332, April 2012.
- J. Wassermann. Volcano seismology. *IASPEI New Manual of Seismological Observatory Practice*, 1(13):662–703, 2002.
- R. Wells. Evolution of the cascadia convergent margin. <http://www.geoprisms.org/images/stories/documents/Cascadia/presentations/thursday/Wells.pdf>, 2014.
- R. E. Wells and P. L. Heller. The relative contribution of accretion, shear, and extension to cenozoic tectonic rotation in the pacific northwest. *Geological Society of America Bulletin*, 100(3):325–338, 1988. doi: 10.1130/0016-7606(1988)100;0325:TRCOAS;2.3.CO;2. URL <http://gsabulletin.gsapubs.org/content/100/3/325.abstract>.

- R. E. Wells and The Cascadia Working Group. Cascadia regional lithospheric studies of the pacific northwest. *U. S. Geological Survey Open-File Report 93-706*, 1989.
- Ray Wells, David Bukry, Richard Friedman, Doug Pyle, Robert Duncan, Peter Haeussler, and Joe Wooden. Geologic history of siletzia, a large igneous province in the oregon and washington coast range: Correlation to the geomagnetic polarity time scale and implications for a long-lived yellowstone hotspot. *Geosphere*, 2014. doi: 10.1130/GES01018.1. URL <http://geosphere.gsapubs.org/content/early/2014/07/14/GES01018.1.abstract>.
- Ray E. Wells, Craig S. Weaver, and Richard J. Blakely. Fore-arc migration in cascadia and its neotectonic significance. *Geology*, 26(8):759–762, 1998. doi: 10.1130/0091-7613(1998)026;0759:FAMICA;2.3.CO;2. URL <http://geology.gsapubs.org/content/26/8/759.abstract>.
- R.E. Wells and R.W. Simpson. Microplate motion of the cascadia forearc and implications for subduction deformation. *Earth, Planets, Space*, 53:275–283, 2001.
- D. S. Wilson. The juan de fuca plate and slab: Isochron structure and cenozoic plate motions. *U.S. Geol. Survey, Reston, Va.*, Rep. 02-238:9–12, 2002.
- Douglas S. Wilson. Confidence intervals for motion and deformation of the juan de fuca plate. *Journal of Geophysical Research: Solid Earth*, 98(B9):16053–16071, 1993. ISSN 2156-2202. doi: 10.1029/93JB01227. URL <http://dx.doi.org/10.1029/93JB01227>.
- J. Witczuk, S. Pagacz, and L.S. Mills. Disproportionate predation on endemic marmots by invasive coyotes. *Journal of Mammalogy*, 94(3):702–713, 2013.